

Is nanostructuring sufficient to get catalytically active Au?

vorgelegt von

M. Sc.

Alexander Yu. Klyushin

aus Archangelsk, Russland

Von der Fakultät II - Mathematik und Naturwissenschaften
der Technischen Universität Berlin
zur Erlangung des akademischen Grades

Doktor der Naturwissenschaften

Dr. rer. nat.

genehmigte Dissertation

Promotionsausschuss:

Vorsitzender: Prof. Dr. Thorsten Ressler

Berichter/Gutachter: Prof. Dr. Robert Schlögl

Berichter/Gutachter: Prof. Dr. Mario Dähne

Berichter/Gutachter: Prof. Dr. Ronald Imbihl

Tag der wissenschaftlichen Aussprache: 24.09.2015

Berlin 2015

На дне терпения оседает золото.

Имам Шамиль

Gold settles at the bottom of patience.

Imam Shamil.

Acknowledgement.

I would like to thank many people for their support and help during my PhD thesis. First of all, I would like to thank my advisor, Prof. Dr. Robert Schlögl, Director of the Department of Inorganic Chemistry at the Fritz-Haber-Institute of Max-Planck-Society, for his guidance, invaluable support and encouragement throughout my PhD project. I would like to particularly acknowledge the members of the doctoral board, Prof. Dr. Mario Dähne and Prof. Dr. Ronald Imbihl, who gladly accepted to invest their valuable time in reviewing this work. Additional gratitude goes to Prof. Dr. Peter Strasser for taking the chair of the examination board.

I am also deeply grateful to Dr. Axel Knop-Gericke, leader of Electronic structure group, for his supervision, input and invaluable advice during my study. I shall also thank all members of Electronic structure group for all time that we spent together in the labs, conferences, meetings and events.

I am highly grateful and indebted to Dr. Tulio Rocha for introduce me into the utilization of the NAP-XPS setup and for providing me comprehensive overview of the research topic. Together with Dr. Mark Greiner their fruitful discussion and ideas during and after beamtimes were invaluable in past years.

I thank BESSY II/HZB for the allocation of synchrotron radiation beamtime. And of course, without efforts of Dr. Michael Hävecker, Dr. Raoul Blume and Birgitt Zada the ISSIS beamline operation would be impossible. With this respect, I am truly grateful to the technical support offered by Eugen Stotz in set-up construction.

Further acknowledgment goes to microscopy group, especially to Dr. Marc Willinger, Dr. Thomas Lunkenbein, Dr. Xing Huang, Dr. Manfred Schuster, Gisela Weinberg and Zhu-Jun Wang, for the amazing TEM and SEM images of Au-based catalysts. I shall also thank Dr. Matthias Friedrich for all catalytic tests of various samples at 1 bar pressure. I would also like to extend my gratitude to Dr. Rosa Arrigo, Dr. Zailai Xie, Dr. Yi Youngmi, Dr. Olaf Timpe and Xuan Li for the efforts made in sample synthesis.

Moreover, I would like to thank all my labmates, colleagues, and project partners for every piece of contribution that lead to the success of this work: Prof. Dr. Valerii Bukhtiyarov (Boreskov Institute of Catalysis, Russia), Dr. Andrey

Bukhtiyarov (Boreskov Institute of Catalysis, Russia), Dr. Igor Prosvirin (Boreskov Institute of Catalysis, Russia), Dr. Detre Teschner, Dr. Ramzi Farra, Dr. Juan Velasco-Vélez, Verena Pfeifer, Maike Hashagen, Norbert Pfänder.

Last but not least important, I would like to thank my parents for their encouragement and support despite the distance. Finally, I would like to express my deepest gratitude to my wife for endless patience and belief in me during PhD study.

Table of Content

List of Abbreviations	iii
List of Figures	v
List of Schemes	xi
List of Tables	xii
1. Introduction	1
1.1. Catalysis	1
1.2. Type of catalysis	2
1.3. Mechanisms in gas/solid heterogeneous catalysis	3
1.4. X-ray photoelectron spectroscopy for investigation catalytic process ..	4
1.5. Au catalysts	5
1.6. Outline of the Thesis	7
2. Experimental part	9
2.1. Beamline	9
2.2. Endstation	11
2.3. X-ray photoelectron spectroscopy	12
2.4. X-ray adsorption spectroscopy	16
2.5. Scanning electron microscopy	20
2.6. Transmission electron microscopy	21
2.7. Quadrupole mass spectroscopy	24
2.8. Reactor for CO oxidation at atmospheric pressure	25
2.9. XPS measurement performance	26

3. Results	29
3.1. Extended Au surface	29
3.1.1. Clean and oxidized Au foil.....	29
3.1.2. CO oxidation on Au foil	40
3.1.3. Clean and oxidized Au powder	41
3.1.4. CO oxidation on Au powder	43
3.1.5. Conclusions	47
3.2. Au nanoparticles on oxygen-free support	49
3.2.1. Au/HOPG	49
3.2.2. Au/N-CNTs and Au/O-CNTs	53
3.2.3. HOPG	57
3.2.4. Au/Au foil	58
3.2.5. Conclusions	64
3.3. Au nanoparticles on oxide support	65
3.3.1. Au/Fe ₂ O ₃ -PC (photo-induced decomposition of an Au-azido- complex to generate zero-valence Au-species)	65
3.3.2. Au/Fe ₂ O ₃ -C (co-precipitation) and Au/TiO ₂ -DP (deposition- precipitation)	70
3.3.3. Conclusions	85
4. Summary.....	87
Bibliography.....	90
Statement on the contributions to the publications in this thesis	98

List of Abbreviations

Au/Fe₂O₃-C	Au/Fe ₂ O ₃ synthesized by co-precipitation method
Au/TiO₂-DP	Au/TiO ₂ synthesized by deposition-precipitation method
Au/Fe₂O₃-PC	Au/Fe ₂ O ₃ synthesized by photo-induced decomposition of a Au-azido-complex to generate zero-valence Au-species method
BE	Binding Energy
BESSY II/HZB	Berliner Elektronenspeicherring für Synchrotronstrahlung/ Helmholtz-Zentrum-Berlin
CNT	Carbon Nanotube
DFT	Density Functional Theory
EDX	Energy-Dispersive X-ray Spectroscopy
EELS	Electron Energy Loss Spectroscopy
E-SEM	Environmental Scanning Electron Microscopy
ESCA	Electron Spectroscopy for Chemical Analysis
EXAFS	Extended X-ray Absorption Fine Structure
ISS	Innovative Station for In-Situ Spectroscopy
FWHM	Full Width at Half Maximum
HOPG	Highly Oriented Pyrolytic Graphite
HV	High Vacuum
IMFP	Inelastic Mean Free Path
KE	Kinetic Energy
N-CNT	Nitrogen-functionalized Carbon Nanotube
NAP	Near Ambient Pressure
NEXAFS	Near-Edge X-ray Absorption Fine Structure
NP	Nanoparticle
O-CNT	Oxygen-functionalized Carbon Nanotube
PROX	Preferential Oxidation
QMS	Quadruple Mass Separation
RT	Room Temperature
SEM	Scanning Electron Microscopy
SMSI	Strong Metal Support Interaction

STEM	Scanning Transmission Electron Microscopy
TEM	Transmission Electron Microscopy
ToS	Time on Stream
UHV	Ultrahigh Vacuum
UV	Ultra Violet
UV/Vis	Ultraviolet–visible
VB	Valence Band
wt%	Weight Percent
XANES	X-ray Absorption Near-Edge Structure
XAS	X-ray Absorption Spectroscopy
XP	X-ray Photoelectron
XPS	X-ray Photoelectron Spectroscopy

List of Figures.

Figure 2.1	The optical layout of ISSS beamline	9
Figure 2.2	Sketch demonstrating the main components of NAP-XPS set-up ...	11
Figure 2.3	Electron trajectories inside a differentially pumped aperture system a) without electrostatic lenses, b) with electrostatic focusing lenses included. Electrons are assumed to enter from the left	12
Figure 2.4	Several ways to subtract background	15
Figure 2.5	XANES and EXAFS at Fe K-edge	17
Figure 2.6	Layout of SEM	20
Figure 2.7	The scheme of specimen chamber in E-SEM	21
Figure 2.8	Cross-section and layout of TEM	22
Figure 2.9	Possible signals available in TEM	23
Figure 2.10	End-on view of quadrupole mass spectrometer.....	24
Figure 2.11	Stability diagram for quadrupole mass spectrometer.....	25
Figure 2.12	Sapphire sample holder with a stainless steel back-plate and a lid with 8 mm hole	27
Figure 3.1	Survey photoelectron spectrum of clean Au foil	29
Figure 3.2	Fitting of NAP (a) Au $4f_{7/2}$ and (b) O 1s photoelectron spectra (using 150 eV kinetic energy photoelectrons) from gold foil at 100°C (i) before (ii) during and (iii) after O ₃ treatment at 0.3 mbar	30
Figure 3.3	Valence band spectra in UHV (bottom), in ozone (middle) and difference spectrum between ozone and UHV environments (top) measured at $h\nu = 130$ eV	31
Figure 3.4	Au 4f photoelectron spectra ($h\nu = 270$ eV) from gold foil during heating (A) and cooling (B) at various temperatures measured at 0.3 mbar and $CO/O_2+O_3=1/80$	32

Figure 3.5	NAP-XP Au 4f _{7/2} spectra (using 150 eV kinetic energy photoelectrons) of a gold foil at 100°C before (black dash line), during (red dot line), after (blue solid) O ₃ treatment at 0.3 mbar and difference spectrum between Au 4f _{7/2} after and before O ₃ treatment	33
Figure 3.6	Au 4f _{7/2} photoelectron spectra (hν = 270 eV) of a gold foil at 100°C in UHV after ozone treatment	34
Figure 3.7	<i>Ex-situ</i> SEM image of a Au foil after O ₃ (0.3 mbar) treatment at 100°C showing ridges only in areas that were exposed to O ₃ (region A). On the left side, where the surface was covered by the sample holder lid, no ridges are observed (region B)	34
Figure 3.8	NAP-XPS depth profile (a) Au 4f _{7/2} and (b) O 1s as obtained from a gold foil during O ₃ (0.3 mbar) treatment at 100°C for increasing kinetic energies of photoelectrons, i.e. decreasing surface sensitivity. Spectra were measured at 175 eV (cyan line), 350 eV (magenta line), 600 eV (dark yellow line) and 1000 eV (purple line) kinetic energy of photoelectrons	35
Figure 3.9	The area ratios between cationic Au 4f _{7/2} and Au ⁰ 4f _{7/2} (red dots), O 1s and Au ⁰ 4f _{7/2} (blue squares) XPS peak as function of inelastic mean free path (IMPF) of Au. Fitting results, assuming an oxide over-layer completely (solid line) and 60% (dash-dot line) covering the Au surface	36
Figure 3.10	O <i>K</i> -edge absorption spectra measured in Auger yield mode in O ₃ +O ₂ at 0.3 mbar and 100 °C	38
Figure 3.11	The change of the reaction mixture (CO/O ₂ +O ₃ =1/20) with time a) without Au foil and b) using Au foil as catalyst at 0.3 mbar and 100 °C.	40
Figure 3.12	Evolution of Au 4f (A) and O 1s (B) photoelectron spectra (using 700 eV kinetic energy photoelectrons) from gold foil at 0.3 mbar and 100°C in reaction mixture (CO/O ₂ +O ₃ =1/20) with time	41

Figure 3.13 Au 4f (A) and O 1s (B) photoelectron spectra (using 150 eV kinetic energy photoelectrons) of a gold powder at 100°C in UHV (bottom) and ozone (0.3 mbar) (top)	42
Figure 3.14 SEM image before (left) and after (right) O ₃ (0.3 mbar) treatment at 100°C showing restructuring of gold powder	42
Figure 3.15 The changes of the reaction mixture (CO/O ₂ +O ₃ =1/80) with time using Au powder as catalyst at 0.3 mbar and 100°C	43
Figure 3.16 <i>In-situ</i> Au 4f (left) and O 1s (right) photoelectron spectra (using 150 eV kinetic energy photoelectrons) of gold powder at 100°C during CO oxidation at 0.3 mbar	44
Figure 3.17 CO oxidation on Au powder at 0.3 mbar and different temperature	44
Figure 3.18 Au 4f photoelectron spectra (hν = 270 eV) from gold powder during heating (A) and cooling (B) at various temperatures measured at 0.3 mbar and CO/O ₂ +O ₃ =1/80	45
Figure 3.19 CO oxidation (CO/O ₂ +O ₃ =1/80) on Au powder with and without O ₃ at 0.3 mbar and 100 °C	46
Figure 3.20 Gas mixture changes while removing Au powder out of the chamber	46
Figure 3.21 NAP (a) Au 4f, (b) O 1s and (c) C 1s XP spectra of Au/HOPG (i) in UHV at RT, (ii) under O ₃ at 0.3 mbar, 100 °C and (iii) under CO and O ₂ (CO:O ₂ =1:75) atmosphere at 0.3 mbar, RT	49
Figure 3.22 SEM image of Au/HOPG a) before and b) after O ₃ treatment at 250 °C and CO oxidation at 0.3 mbar. Images were colorized in order to highlight the differences between the two samples	51
Figure 3.23 QMS data (CO:O ₂ =1:75) of Au/HOPG a) before and b) after O ₃ treatment at 0.3 mbar and RT	53
Figure 3.24 TEM image of large Au particle supported on N-CNT	55
Figure 3.25 STEM image of fresh Au/N-CNTs	55
Figure 3.26 STEM images of fresh Au/O-CNTs	56
Figure 3.27 QMS data (CO:O ₂ =1:75) of Au/O-CNTs A) before and B) after O ₃ treatment at 0.3 mbar and RT	56

Figure 3.28 QMS data (CO:O ₂ =2:1) of a) Au/N-CNTs and b) Au/O-CNTs at 1 bar without any pretreatment	57
Figure 3.29 QMS data (CO:O ₂ =1:75) of HOPG A) before and B) after O ₃ treatment at 0.3 mbar and RT	58
Figure 3.30 NAP (a) Au 4f, (b) O 1s and (c) C 1s XP spectra of Au/Au foil (i) in UHV at RT, (ii) under O ₃ at 0.3 mbar, 150 °C, (iii) under O ₂ after O ₃ treatment at 0.3 mbar, RT and (iv) under CO and O ₂ atmosphere (CO:O ₂ =1:75) at 0.3 mbar, RT	59
Figure 3.31 SEM images of Au/Au foil a) before and b) after O ₃ treatment at 0.3 mbar. Images were colorized in order to highlight the differences between the two samples	62
Figure 3.32 QMS data (CO:O ₂ =1:2) of Au/Au foil a) before and b) after O ₃ treatment at 0.3 mbar and RT	63
Figure 3.33 NAP (a) Au 4f _{7/2} , (b) O 1s and (c) C 1s XP spectra of Au/Au foil under CO reaction (CO:O ₂ =1:2) after O ₃ treatment at 0.3 mbar, RT (i) after 10 min, (ii) 60 min and (iii) 120 min	63
Figure 3.34 TEM images of Au/Fe ₂ O ₃ -PC (A) before and (B) after annealing in O ₂ at 300 °C and CO oxidation (CO:O ₂ =1:2) at 0.3 mbar and 300 °C. Images were colorized in order to highlight the differences between the two samples	66
Figure 3.35 (A) Au 4f, (B) O 1s and (C) C 1s XP spectra of Au/Fe ₂ O ₃ -PC at 0.3 mbar (i) in O ₂ during annealing, (ii) in CO+O ₂ (CO:O ₂ =1:2) at 300 °C and (iii) in CO+O ₂ (CO:O ₂ =1:2) at 100 °C. Photoelectrons with 160 eV kinetic energy were used to collect the O 1s and C 1s spectra, and photoelectrons with 900 eV kinetic energy were used to collect the Au 4f spectra	67
Figure 3.36 CO ₂ production of Au/Fe ₂ O ₃ -PC in CO-reactor at 1 bar and CO:O ₂ =1:2	69
Figure 3.37 CO ₂ production of Au/Fe ₂ O ₃ -C in NAP-XPS chamber at 0.3 mbar	70
Figure 3.38 CO ₂ production of Au/TiO ₂ -DP in NAP-XPS chamber at 0.3 mbar	71
Figure 3.39 CO ₂ production of pure Fe ₂ O ₃ in CO-reactor at 1 bar (CO:O ₂ =1:2) and 373 K	72

Figure 3.40 CO ₂ production of pure TiO ₂ in CO-reactor at 1 bar (CO:O ₂ =1:2) and 373 K	72
Figure 3.41 CO ₂ production of Au/Fe ₂ O ₃ -C in CO-reactor at 1 bar (CO:O ₂ =1:2) and 373 K	73
Figure 3.42 CO ₂ production of Au/TiO ₂ -DP in CO-reactor at 1 bar (CO:O ₂ =1:2) and 373 K	73
Figure 3.43 (A) Au 4f, (B) O 1s and (C) C 1s XP spectra of Au/Fe ₂ O ₃ -C before (top panel) and after (bottom panel) CO oxidation (CO:O ₂ =1:2) at 0.3 mbar and 100 °C. Photoelectrons with 160 eV kinetic energy were used to collect O 1s and C 1s spectra and photoelectrons with 900 eV kinetic energy were used to collect Au 4f spectra	74
Figure 3.44 (A) Au 4f, (B) O 1s and (C) C 1s XP spectra of Au/TiO ₂ -DP before (top panel) and after (low panel) CO oxidation (CO:O ₂ =1:2) at 0.3 mbar and 100 °C. Photoelectrons with 160 eV kinetic energy were used to collect O 1s, C 1s spectra and photoelectrons with 720 eV kinetic energy were used to collect Au 4f spectra	76
Figure 3.45 TEM images of Au/TiO ₂ -DP (A) before and (B) after CO oxidation (CO:O ₂ =1:2) at 0.3 mbar and 100°C. The insets in (A) and (B) represent power spectra of the Au nanoparticles. Images were colorized in order to highlight the differences between the two samples	78
Figure 3.46 TEM image of Au/Fe ₂ O ₃ -C after CO oxidation at 0.3 mbar (CO:O ₂ =1:2) and 100°C. Image was colorized in order to highlight the differences between Au and Fe ₂ O ₃	79
Figure 3.47 EELS spectra of Au/TiO ₂ -DP after CO oxidation at 0.3 mbar (CO:O ₂ =1:2) and 100°C. The inset represents a TEM image of a single Au NP in front of the aperture	79
Figure 3.48 Arrhenius plot of Au/TiO ₂ -DP (blue line) and Au/Fe ₂ O ₃ -C (red line)	80

Figure 4.1 Au 4f XP spectrum and TEM image of sample synthesized by deposition-precipitation (left) and photochemical decomposition of intermediate gold-azido complex (right) method 89

List of Schemes.

Scheme 1.1. Langmuir-Hinshelwood reaction mechanism	3
Scheme 1.2. Eley-Rideal reaction mechanism	3
Scheme 1.3. Mars-van Krevelen reaction mechanism	4
Scheme 2.1. Schematic representation of a) XPS, b) XAS and c) Auger processes	19
Scheme 2.2. Scheme of reactor for CO oxidation at atmospheric pressure	26
Figure 3.1. Suggested CO oxidation pathway on Au/TiO ₂	85

List of Tables.

Table 3.1.	Fitting parameters of Au 4f spectrum of Au foil	31
Table 3.2.	Surface composition of Au/HOPG at different conditions	51
Table 3.3.	Fitting parameters of Au 4f _{7/2} spectra of Au/Au foil	59
Table 3.4.	Fitting parameters of O 1s spectra of Au/Au foil	60
Table 3.5.	Surface composition of Au/Au foil at different conditions	61
Table 3.6.	Fitting parameters of Au 4f _{7/2} and O 1s spectra of Au/Fe ₂ O ₃ -PC ...	67
Table 3.7.	Fitting parameters of Au 4f _{7/2} and O 1s spectra of Au/Fe ₂ O ₃ -C	75
Table 3.8.	Surface composition of Au/Fe ₂ O ₃ -C before and after CO oxidation (CO:O ₂ =1:2) at 100 °C	75
Table 3.9.	Fitting parameters of Au 4f _{7/2} and O 1s spectra of Au/TiO ₂ -DP.	77
Table 3.10.	Surface composition of Au/TiO ₂ -DP before and after CO oxidation (CO:O ₂ =1:2) at 100 °C	77
Table 3.11.	Main finding of Au NPs supported on transition metal oxides	81
Table 3.12.	Activation energies for CO oxidation and specific surface area of Au/Fe ₂ O ₃ and Au/TiO ₂ prepared by different methods	84
Table 4.1.	CO oxidation on Au-based catalysts	88

1. Introduction.

1.1. Catalysis.

The word *catalysis* is derived from latinized form of Greek noun *κατάλυσις*, related to the verb *καταλύειν*, meaning ‘to dissolve’, which originates from Greek prefix *κατά* and verb *λύω*. *Κατά* means ‘down’ and the meaning of *λύω* is ‘to loosen’. The term *catalysis* was coined in 1836 by Swedish scientist Jöns Jakob Berzelius, who noted that certain chemicals speed up a reaction. He wrote: “*I shall therefore call it the catalytic power of substances, and the decomposition by means of this power catalysis, just as we use the word analysis to denote the separation of the component parts of bodies by means of ordinary chemical process. Catalytic power actually means that substances are able to awake affinities which are asleep at this temperature by their mere presence and not by their own affinity*” [1]. The development of experimental and theoretical techniques and the accumulated results allowed Nobel Prize winner Friedrich Wilhelm Ostwald to define a catalyst as “*a substance that increases the rate at which a chemical system approaches equilibrium, without being consumed in the process.*” Nevertheless, the position of equilibrium attained in the presence of a catalyst is the same as that ultimately arrived at in its absence [2]. It is only the difference between initial and final states that determines a free energy change - and hence the position of equilibrium - not whether a catalyst was used to bring about the change.

According to the equation proposed by Svante Arrhenius, the reaction rate constant **k** is defined as follows:

$$k = A \exp(-E_a/RT) \quad (1.1)$$

Where, **A** is the pre-exponential factor, which is proportional to the collision number between unlike molecules according collision theory, **E_a** is the activation energy, **R** is the gas constant and **T** is the temperature. Therefore, the effect of a catalyst on a chemical reaction is to increase its rate, in other words to increase its rate constant. Thus we can conclude that a catalyst acts by decreasing the activation energy of the reaction. A catalytic reaction happens via the adsorption of a molecule on the catalyst

surface, forming a transition state with a resulting loss of translational freedom. This means that catalytic reactions proceed by a new energetically favorable pathway.

1.2. Types of catalysis.

There are three main forms of catalysis: homogeneous, heterogeneous, and enzymatic or biocatalysis. We briefly discuss these types of catalysis in this section.

Biological catalysts called enzymes, are complex organic molecules usually consisting of proteins, which form a lyophilic colloid. Enzymes are neither homogeneous nor heterogeneous catalysts, but sometimes in between. They are extremely efficient catalysts, for example nitrogenase enzymes convert nitrogen from the air to ammonia at ambient temperature [3], while the Haber-Bosch process requires temperature above 400 °C [4, 5]. Biocatalysts occur widely in our life. Over 150 biocatalytic processes are running today: the enzymes are employed in food and drink industries. Over the past century the application of biocatalysts has especially increased in the pharmaceutical industry.

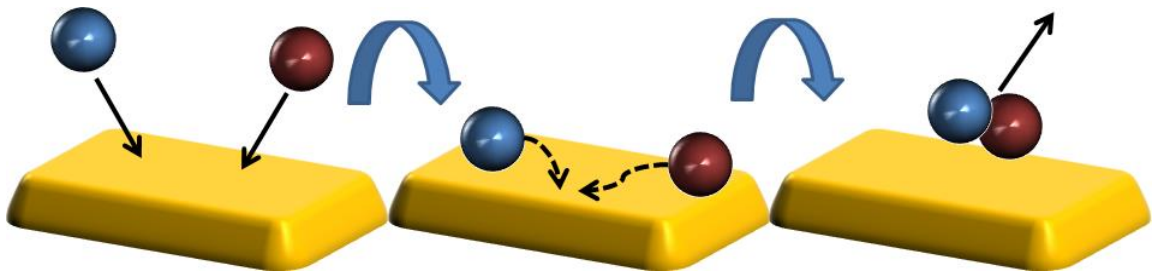
In homogeneous catalysis, the catalyst and the reactants are in the same phase, and no phase boundary exists. The main advantages of homogeneous catalysis are high activity and selectivity, the main disadvantage is the complexity of catalyst separation and recovery. However, about 10% by volume of all industrial catalytic processes occurs on homogeneous catalysts. One important industrial example of homogeneous catalysis is the hydroformation reaction, in which CO and H₂ molecules are added to alkene [6].

In heterogeneous catalysis, the catalyst is in a different phase from the reactants. The catalytic reaction takes place at the catalyst border (surface), where the reaction mixture is temporarily adsorbed. Nowadays, heterogeneous catalysis plays an important role in our life, in particular, in the petrochemical and bulk chemistry industries and in the energy storage cycles, via converting electrical energy into chemical energy. Examples of heterogeneous catalysis include such reactions as methanol synthesis on Cu/ZnO/Al₂O₃ [7] and Fischer-Tropsch synthesis on Co and Fe [8].

1.3. Mechanisms in gas/solid heterogeneous catalysis.

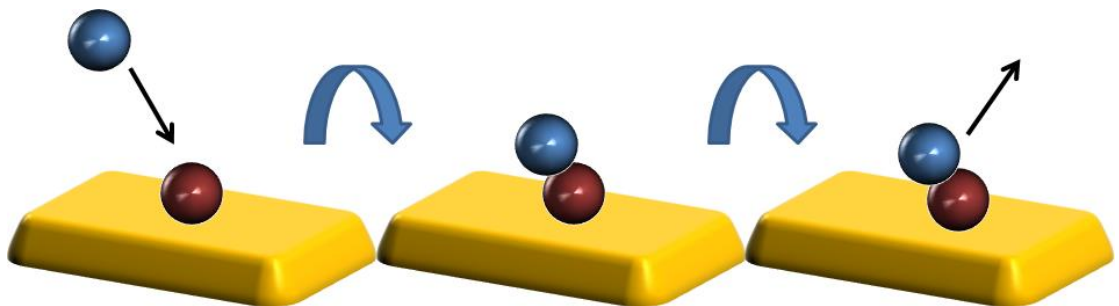
In this work we focus on heterogeneous catalysis in the gas/solid system, therefore the following chapter will briefly discuss different reaction mechanisms. In all mechanisms of heterogeneous catalysis there is one common feature, at least one of the reactants is adsorbed on the catalyst.

The Langmuir-Hinshelwood model describes the most common situation in heterogeneous catalysis [9]. This mechanism assumes that both reactants are first adsorbed on the catalyst surface, then migrate to each other and react (Scheme. 1.1). The products are afterwards desorbed from the catalyst back to the gas phase.



Scheme 1.1 Langmuir-Hinshelwood reaction mechanism.

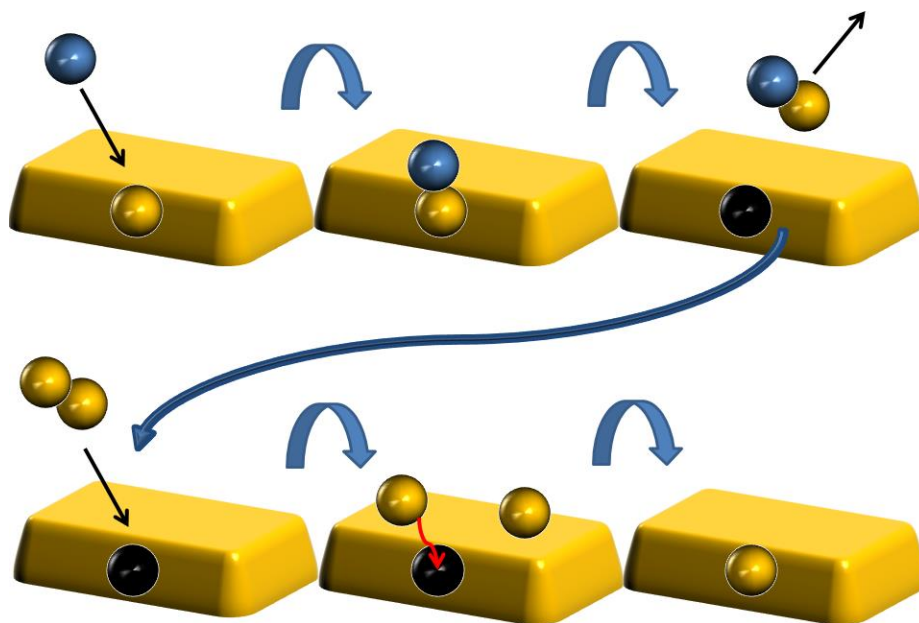
In the Eley-Rideal mechanism only one reactant is directly chemisorbed on the catalyst. The reaction takes place between reactant from the gas phase and an adsorbed one (Scheme 1.2). The Eley-Rideal mechanism well describes the kinetics of the hydrogen-deuterium reaction [10].



Scheme 1.2. Eley-Rideal reaction mechanism.

The third mechanism is assigned as Mars-van Krevelen mechanism and applies to oxidation reactions on oxides, which are easily reducible. The oxidation occurs between adsorbed reactant and lattice oxygen, which is later replaced by dissociated

molecular oxygen or by the bulk (Scheme 1.3). An example of the Mars-van Krevelen mechanism is CO oxidation under high oxygen pressure on Pt [11].



Scheme 1.3. Mars-van Krevelen reaction mechanism.

1.4. X-ray photoelectron spectroscopy for investigation of catalytic process.

Model systems have been investigated under well-defined ultrahigh vacuum (UHV) conditions with different methods using surface science approach, which allows applying simplified version of catalysts and reaction [12-15]. Such investigation have provided information about elementary steps of reaction on the surface, changes of electronic and geometric structure of the surface when atoms and molecules are presented, surface dynamics, the role of defects, etc. Theoretical calculations [16] have been used to guide the experiments [17].

The major disadvantage of the surface science approach is that catalysts are investigated far from realistic operating conditions. Surface science studies focus on the catalytic behavior of well-structured (single crystal, alloy, oxide) samples, while catalysts are complex multicomponent materials, this leads to the so-called “material gap”. There exists as well a “pressure gap”, because operating pressure in catalytic reactors are orders of magnitude higher than in the UHV chambers. The pressure

influences the morphology of catalysts, dynamics and reaction mechanism because of the chemical potential of the reactant.

The preparation of nanostructured supported model catalysts bridges the “material gap” [18-20]. Meanwhile the first attempts to bridge “pressure gap” were *ex-situ* experiments, where sample were directly transferred between reactor and UHV chamber. This strategy helps find correlation between catalytic activity in the reactor and the structure before and after reaction [21]. The main disadvantage of *ex-situ* measurements is that they cannot give insights into metastable species formed just under reaction conditions, which might be very relevant for the catalytic process [22].

The understanding of the interaction of a catalyst's surface with gas atmospheres plays a key role in a detailed description of catalytic processes. X-ray photoelectron spectroscopy (XPS) is well-known method for the characterization of surfaces under high vacuum, but the application of XPS at elevated pressures started more than 40 years ago. However, a spectroscopic characterization of the reacting surface under ambient condition is challenging, because emitted electrons are scattered by gas under operating pressures. The Fritz-Haber-Institut der Max-Planck-Gesellschaft in collaboration with the group of M. Salmeron (Berkley) developed a set-up suitable to record photoelectron spectra in the presence of a reacting gas. Nowadays the operating pressure in the setup is up to 10 mbar. The detailed description of the set-up is in the section 2.2.

1.5. Au catalysts.

The noble character of bulk Au has been well known for centuries. Corrosion and oxidation resistance are the hallmarks of Au, with these properties being exploited in many technological and everyday applications, such as dentistry, jewelry and electronics. Gold owes its unusual properties for its unique electronic structure. Gold is the 79th element in periodic table with electronic configuration $1s^2 2s^2 2p^6 3s^2 3p^6 4s^2 3d^{10} 4p^6 5s^2 4d^{10} 5p^6 4f^{14} 5d^{10} 6s^1$. It lies in the 11th group of the periodic table along with silver and copper, which are well known catalysts in ethylene epoxidation and methanol synthesis.

Having excellent catalysts in its neighborhood, it is obvious that scientists tried to use Au as catalyst too. Most of the tests showed inactivity of Au, but it is not surprising as they were done with macroscopic Au (wires, powders and foils). Nevertheless, some hints that gold is not always inert were found, for example, Michael Faraday found that Au presents catalyzed hydrogen oxidation at room temperature [23]. Therefore, gold has long been ignored for catalytic purposes due to the inert nature of bulk Au until 1980's.

In 1989, impressive demonstrations that gold's noble characteristics spectacularly vanish as the dimensions of the material are reduced to the nanometer scale were provided by Haruta and co-workers [24], who found Au nanoparticles supported on transition metal oxides to have a high catalytic activity in CO and H₂ oxidation, even at low temperatures. This pioneering work has prompted Au catalysis to become a very active research field in recent years, but the nature of active sites on gold is still under debate in the literature [25]. The huge difference between the catalytic behaviors of extended Au surfaces and supported nanoscopic Au has emerged in numerous studies, which came to partly contradictory conclusions. One of the most common conclusions is that the way in which gold acts catalytically is substantially different from that adopted for metals of the platinum group [26].

Supported Au-based catalysts have shown activity for epoxidation of olefins [27,28], water-gas-shift reactions [29,30], C-C coupling reactions [31], liquid-phase oxidation of alcohols [32], selective reduction of NO by hydrocarbons in presence of high oxygen concentrations [33,34], preferential oxidation (PROX) of CO in a hydrogen atmosphere [35,36], selective oxidation of hydrocarbons [37], epoxidation of propene [38], selective hydrogenation of acetylene to ethylene [39] and of 1,3-butadiene to butene [40] and CO oxidation [41]. Also plenty of metal oxide supports, like CeO₂ [42], TiO₂ [43-45], ZrO₂ [46], Al₂O₃ [47], Fe₂O₃ [48], FeO [49], were tested and some common factors affecting catalytic behavior, such as particle size [50], method of preparation [51], pretreatment [52], oxidation state of Au [53], were found.

Nano-structured Au, supported on transition metal oxides, is a highly efficient oxidation catalyst; however, the mechanism of these reactions is still the focus of intense debate in the literature. For instance, edge sites and changes in the electronic

structure of Au, due to its interaction with the support, have been suggested to be important factors in establishing activity [25]. Furthermore, the activity of Au in CO oxidation increases in the presence of water [41,54]. Several works have clearly shown that CO can be readily oxidized to CO₂, at any kind of Au surface, if a source of atomic oxygen is present [25]. Ozone (O₃), N₂O, and O₂ plasma have been used as sources of atomic oxygen to show that even extended surfaces of Au single-crystals can be catalytically active towards CO oxidation [55]. For high-performance, supported, nano-structured Au catalysts, it has been debated whether or not oxygen atoms are obtained by direct O₂ dissociation at the Au clusters or provided by the oxide support [56]. Based on DFT calculations [57], it was proposed that low-coordinated atoms on Au clusters play a central role in molecular oxygen activation. Contrary to the case of extended Au surfaces, adsorbed O on Au clusters is stable relative to O₂ in the gas phase. In turn, recent theoretical and experimental investigations show that Au perimeter atoms can be active sites in CO oxidation reaction. The interpretation of the results combines the role of low coordinated Au atoms and interaction with the support. However, the role of the support for the catalytic reaction is still under discussion and the identification of the nature of active sites requires a systematic study of Au-based catalysts.

1.6. Outline of the Thesis.

Effective catalyst design based on a rational approach requires knowledge of the relationship between the electronic and morphological features of a catalyst and their roles in the catalytic reaction pathway. Such an understanding can only be obtained by analyzing catalysts under working conditions. A systematic study of the effects of different strategies of Au activation by comparing the activity, morphology and electronic structure before, after and during CO oxidation allows understanding what makes Au less noble. Therefore, it is necessary to apply various techniques such as X-ray photoelectron spectroscopy, X-ray absorption spectroscopy, scanning and transmission microscopies, mass-spectroscopy and electron energy-loss spectroscopy in order to gain a deeper insight into the complex physical and chemical properties of Au.

The thesis is composed of four cumulative chapters. After the introduction presented in Chapter 1, the basics of techniques used in the present work are described in Chapter 2. Chapter 3 consists of three subchapters, which describe the major finding of the thesis. The subchapters are adopted from publications that cover the results obtained during this doctoral thesis. In subchapter 3.1 the oxidation mechanism of Au is discussed using multiple *in-situ* and *ex-situ* techniques. Also the catalytic performance of extended Au surfaces was investigated in details. The catalytic properties of Au nanoparticle on oxygen-free support (highly oriented pyrolytic graphite, functionalized carbon nanotubes and Au foil) as well as their electronic and surface structures are investigated in subchapter 3.2. Subchapter 3.3 describes Au nanoparticles on transition metal oxides synthesized by precipitation and photochemical decomposition of intermediate gold-azido complex methods. Special attention is paid to the investigation of interaction between Au and transition metal oxides by surface sensitive techniques. Finally, the main findings are summarized in Chapter 4.

2.Experimental part.

2.1. Beamline.

The experiments were performed at ISSS (Innovative Station for In-Situ Spectroscopy) beamline at the electron storage ring BESSY II/HZB (Berliner Elektronenspeicherring für Synchrotronstrahlung/Helmholtz-Zentrum-Berlin), Berlin, Germany.

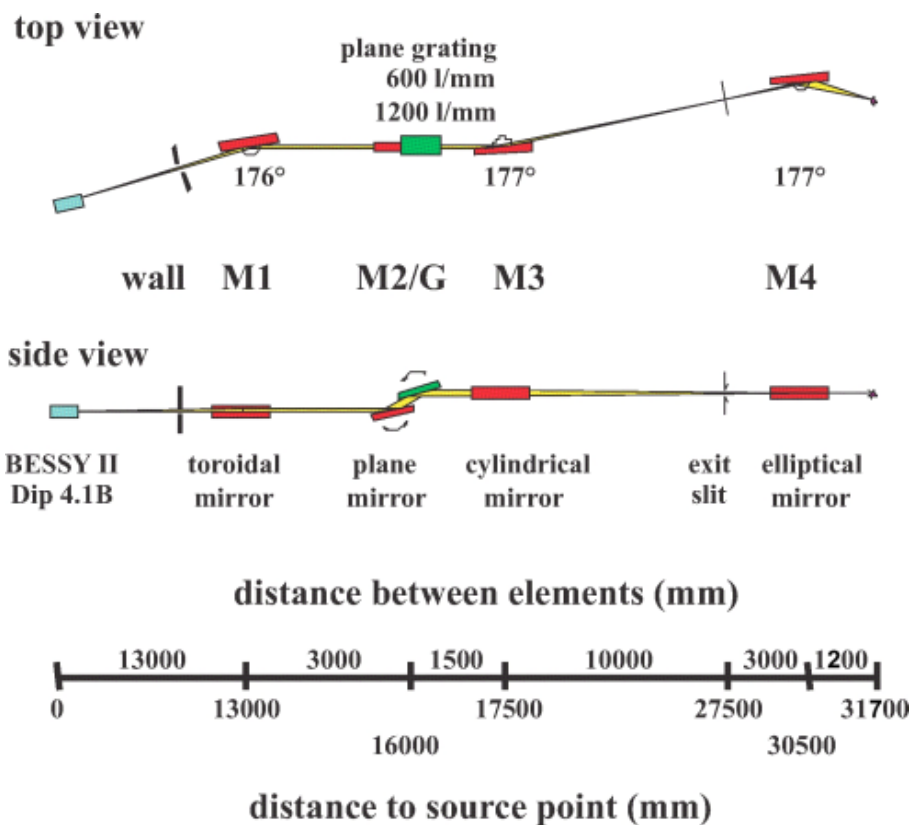


Figure 2.1. The optical layout of ISSS beamline

The optical layout of the beamline is shown in Figure 2.1. The beamline is located at the third generation synchrotron radiation source. Synchrotron radiation is generated by electrons with energy of 1.7 GeV in the bending magnet of the storage ring. The orbit of electrons (circumference of the storage ring is a 240 m) is stable and it makes possible to abandon an entrance slit of monochromatization system. The beam is collimated in the vertical plane by the toroidal mirror (M1), which center is 13 m away from the light source. The mirror is placed in an ultrahigh vacuum

chamber and is equipped with three adjustment devices allowing the necessary precision of angles and linear movement. A water cooling system is used to eliminate heating of the mirror by incident radiation. Downstream of M1, the beam enters the chamber of monochromator, containing planar mirror M2 and planar grating G. The design provides the ability to change gratings (1200 and 600 l/mm) without breaking the vacuum in the system. Their rotation is necessary for the wavelength changing, for the effective use of the entire surface of the optical element and for the reduction of intensity loss. The monochromator chamber is equipped with two optical angle encoders for accurate determination of the rotation angle of the mirror and grating, the signal from which is sent to the control computer. Such an arrangement of optical elements can significantly increase the energy resolution and effectively suppress the higher-order spectrum, as well as provide high beam intensity without additional movements of the optical elements in the entire operating range. In this design, the fix focus constant $c = (\cos \beta / \cos \alpha)$ (α : angle of incidence, β : angle of diffraction relative to the grating normal, respectively) is kept constant during the scanning of the photon energy.

Monochromatized radiation enters the next chamber with a cylindrical mirror M3, which focuses light on the exit slit. The photoionization chamber is the next one (not shown in Figure 2.1). It is designed to record photoionization spectra of various gases to determine the spectral resolution and calibration of the monochromator wavelength. The chamber operates as a gas cell when the inlet and outlet valves are closed. In the inlet valve there is a polyamide window with 120 nm thick, which maintains pressure to 5 mbar. Gas comes into the cell through a leak valve simultaneously with continuous differential pumping through a turbo pump.

The beam enters the last chamber with elliptical mirror M4. The photon beam is re-focused after the exit slit to ensure a high brilliant X-ray spot at the sample position. The spot size is typically $150\mu\text{m} \times 100\mu\text{m}$ (h×v). The intensity of the photon flux at the location of the sample is determined from the photoemission current of gold foil, taking into account the quantum yield. The beamline is optimized to deliver photons in the energy range between 80eV - 2000eV with a high photon flux of up to 6×10^{10} photons/ sec/ 0.1A ring current.

2.2. Endstation.

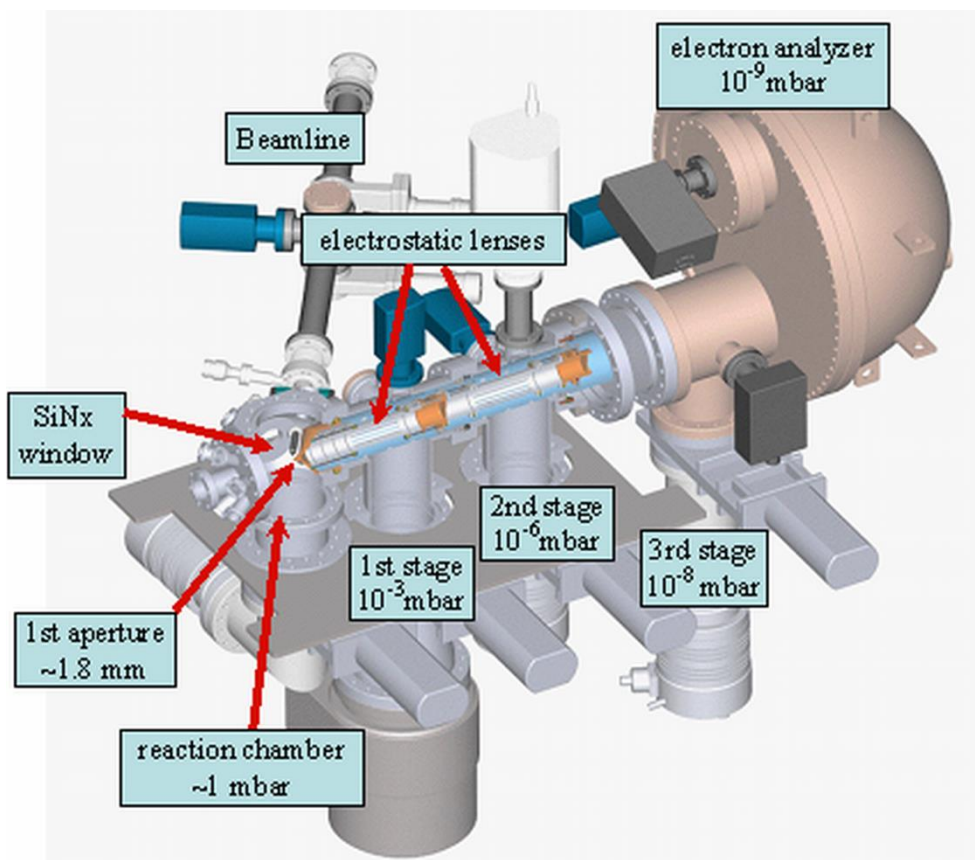


Figure 2.2. Sketch demonstrating the main components of NAP-XPS set-up.

A sketch of the near ambient pressure XPS (NAP-XPS) set-up is shown in Figure 2.2. The stainless steel NAP-XPS chamber consists of four main parts: a) load-lock chamber (not shown in Figure 2.2), b) reaction chamber, c) differential pumping stage, d) electron analyzer.

The load-lock chamber is designed to insert samples and to clean sample surfaces by sputtering. The reaction chamber has a small volume, which is separated from the beamline by a SiN_x membrane to avoid venting the beamline during *in-situ* measurements at mbar pressures. The gases are dosed to the reaction chamber through a stainless steel tube; the flows are monitored by five mass-flow controllers. The pressure control stage allows constant pressure to be maintained inside the chamber, independently of gas flow. The reaction chamber is equipped with a differentially pumped electron-impact mass spectrometer ('PRISMA', Pfeiffer

Vacuum GmbH., Asslar) and a four channel micro gas chromatograph (CP-4900, Varian Inc., Palo Alto) to monitor the gas feed and the formed products.

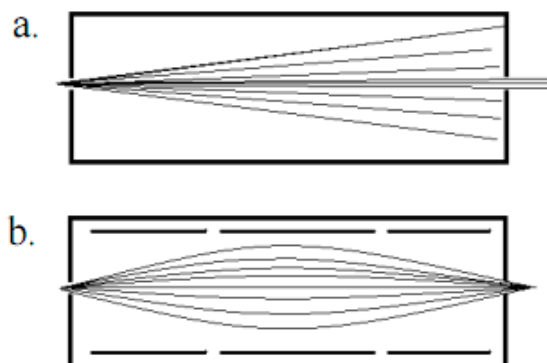


Figure 2.3. Electron trajectories inside a differentially pumped aperture system a) without electrostatic lenses, b) with electrostatic focusing lenses included. Electrons are assumed to enter from the left.

The differentially pumped part is separated from the main chamber by a nozzle with a 1 mm diameter aperture, and consists of four pumping stages. Across the four pumping stages the pressure decreases gradually from 1 mbar (in the reaction chamber) to 10^{-9} mbar (in the electron analyzer). The signal loss is minimized by positioning the sample within ca. 1 mm of the differentially pumped aperture system, thereby minimizing the path length of the photoelectron in the gas. Simultaneously, the differentially pumped aperture system serves as an electrostatic lens system that decreases significantly electron loss and thus increases the efficiency of electron collection (compare to Figure 2.3a and 2.3b).

2.3. X-ray photoelectron spectroscopy.

X-ray photoelectron spectroscopy (XPS, also known as electron spectroscopy for chemical analysis or ESCA) is a well-known surface science technique and has its origin in the work of Robinson and Rawlison [58] and de Broglie [59] a century ago. It provides information about elemental composition (species of atoms on surfaces, concentration of surface atoms, vertical distribution), molecular state of adsorbates and oxidation states of surface species. The detection limit of the method ranges from 0.1 to 0.5 atom percent, i.e. $1\text{-}5\cdot 10^{12}$ atoms/cm², it depends on photon energy,

photon flux, element cross section, analyzer pass energy, aperture settings, dwell time and set-up geometry.

Emission of electrons from the sample is preceded by the absorption of a photon of energy $h\nu$ according to:

$$\Psi_{tot}^i(N), E_{tot}^i(N) \xrightarrow{h\nu} \Psi_{tot}^f(N, K), E_{tot}^f(N, K) . \quad (2.1)$$

Here $\Psi_{tot}^i(N)$ is the initial-state N -electron wave function corresponding to a total energy $E_{tot}^i(N)$ and $\Psi_{tot}^f(N, K)$ is the K th final-state N -electron wave function (including the photoelectron) corresponding to a total energy $E_{tot}^f(N, K)$. The relevant energy conservation equation is

$$E_{tot}^i(N) + h\nu = E_{tot}^f(N, K) . \quad (2.2)$$

In practice the following assumption is used: the photoelectron is sufficiently weakly coupled to the $(N-1)$ -electron ion [60] so as to permit separating the final state of the excitation process to yield:

$$\Psi_{tot}^i(N), E_{tot}^i(N) \xrightarrow{h\nu} \Psi_{tot}^f(N-1, K), E_{tot}^f(N-1, K) + \varphi^f(1)s^f(1), E_{kin} \quad (2.3)$$

in which $\Psi_{tot}^f(N-1, K)$ and $E_{tot}^f(N-1, K)$ refer to the K th $(N-1)$ -electron ionic state that can be formed, E_{kin} is the kinetic energy of K th photoelectron, $\varphi^f(1)$ is the spatial part of one-electron orbital describing and $s^f(1)$ is the spin part of photoelectron orbit. The form of $\varphi^f(1)$ depends on kinetic energy. The energy conservation equation takes the following form:

$$E_{tot}^i(N) + h\nu = E_{tot}^f(N-1, K) + E_{kin} . \quad (2.4)$$

This form is the most useful in XP spectra analysis. By definition, the binding energy (BE) corresponding to leaving the ion in a state, which is described by $\Psi_{tot}^f(N-1, K)$:

$$E_b^V(N) = E_{tot}^f(N-1, K) + E_{tot}^i(N) . \quad (2.5)$$

If we neglect changes in kinetic energy due to work function differences between specimen and electron analyzer, the equation (2.4) will transform to:

$$E_b^V(N) = h\nu + E_{kin} . \quad (2.6)$$

The chemical environment of the element affects the value of binding energy measured for a given element. Siegbahn and co-workers [61] showed the importance of these chemical shifts for the identification of chemically different species.

The chemical shifts contain important information about origin of bonding between an atom and its environment. The physical principles underlying the shifts are simple: the energy of an electron is determined by the Coulomb interaction between the photoelectron and the nuclei (attractive potential) and nearby electrons (repulsive potential). A change in chemical environment leads to a spatial rearrangement of the surrounding electrons and results in a different potential created by all charged particles in the system. The identification of a chemical environment by chemical shifts can be done by comparing the measured binding energy with the binding energy of reference compounds containing the same element. This fingerprint technique is commonly used in catalysis.

Special attention should be paid to energy calibration synchrotron radiation as photon source. There are two most common ways to calibrate BE: 1) align peak positions using reference (in conductive material BE of Fermi edge is taken as 0 eV); 2) use higher orders of radiation, which are reflected from the mirror according Bragg's law. Usually 1st and 2nd orders are used, the difference in kinetic energy of emitted electrons provides "real" (calibrated) photon energy, according following equations:

$$h\nu = E_b + E_{kin1} \quad (2.7)$$

$$2h\nu = E_b + E_{kin2} \quad (2.8)$$

$$h\nu = E_{kin2} - E_{kin1} \quad (2.9)$$

For quantitative XPS analysis, least-squares fitting of the spectra should be done. The selection of correct line shape is very important as well as proper background subtraction. For metallic components a Doniach-Sunjic line shape is the best choice, Voight or a product of a Gaussian with a Lorentzian line shapes for others peaks can be used to obtain the best fit.

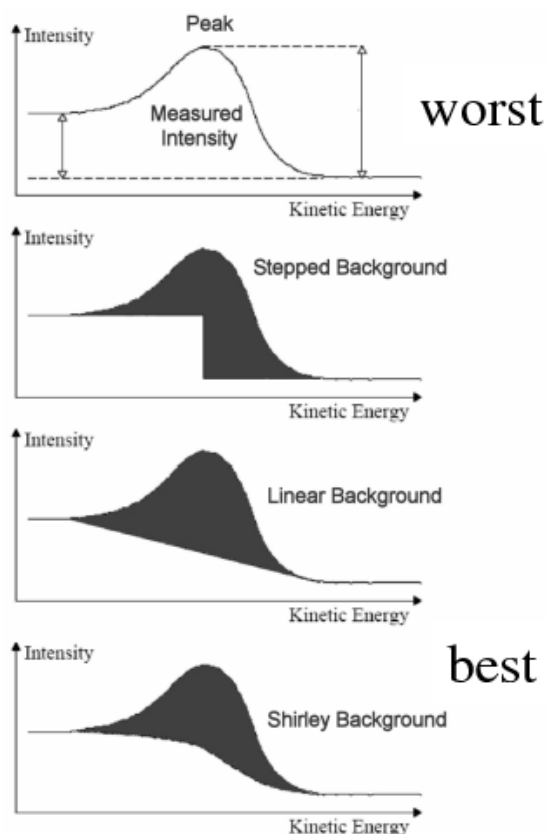


Figure 2.4. Several ways to subtract background.

There are several ways to subtract background as shown in Figure 2.4. The worst case is no background subtraction, stepped and linear backgrounds represent better approximations. The most common method of Shirley [62], where the intensity of background at any given point is proportional to the total integral peak area above the background in the higher kinetic energy peak range is shown at the bottom of Figure 2.4. Another type of background subtraction was introduced by Tougaard [63]. This methodology is based on the integration of the intensity of the background at a given binding energy of the spectral intensities of higher kinetic energies. The linear background suffers from large peak area changes depending on the position of the chosen end points. The Tougaard background is the most accurate one, but the disadvantage of the method is the complications in practical use (required long energy range, minimum peak overlapping). The Shirley background is somewhere in between for accuracy, however its easy application has resulted in its widespread adoption.

The changes in the XP spectrum may not only be caused by different chemical environments, but also X-ray radiation itself can damage the surface. X-ray-induced beam damage during XPS studies requires special attention. The effects of photon beam irradiation on solid surfaces have a complex nature, but the main demonstrations are changes in composition (segregation, adsorption-desorption), beam heating (reactions, interdiffusion), changes in physical structure (defects, bond breaking) and charging of insulators. To minimize beam damage a movement of beam spot is necessary time to time.

2.4. X-ray absorption spectroscopy.

X-ray absorption spectroscopy (XAS) is a highly informative method of experimental study of molecular and solid-state samples due to the method's elemental selectivity and ability to probe free electronic states, with high energy resolution and high sensitivity to chemical structure.

The process of absorption of X-ray quanta by atoms of polyatomic systems (molecules, complexes, clusters and solids) occurs with the highest probability when the photon energy is close to the binding energy of one of the inner shell electrons of an atom within the system. Two different processes are possible: 1) if $h\nu \geq E_i$, the electron will be emitted from the atom with a kinetic energy $E_{kin} \geq 0$. In other words, atoms are photoionized followed by a formation of a cation and photoelectron. 2) If $h\nu < E_i$, the electron will remain bounded to a molecule [64].

The first case corresponds to the continuous absorption starting stepwise, when $h\nu = E_i$ (absorption edge). After the absorption edge, a monotonic decrease of the absorption coefficient is observed, which is usually superimposed on the additional structure called the fine structure of X-ray absorption edge (Figure 2.5). The presence of this structure is easily explained by the description of X-ray photon absorption as a two-stage process, consisting of: 1) the act of absorption of a quantum of light by an atom and the appearance of a photoelectron in the inner electron shell; 2) subsequent release of the photoelectron from polyatomic systems. Broad low-intensity oscillations in absorption, which are observed when photoelectron kinetic energy is >50 eV, are called Extended X-ray Absorption Fine Structure (EXAFS). It appears as a result of interference of the primary photoelectron

wave and single scattered photoelectron waves in the potential field of the atom and its neighbors from the nearest coordination spheres.

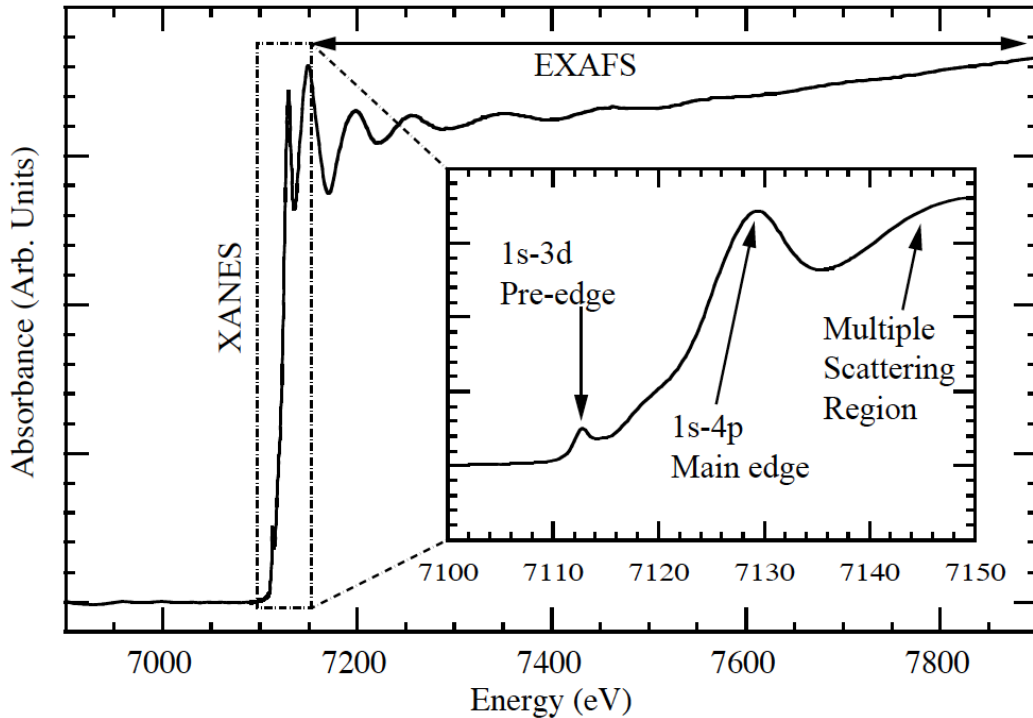


Figure 2.5. XANES and EXAFS at Fe K-edge [65].

In the second case, a series of separate, and often quite narrow, strong absorption lines appear before and after the absorption edge. This Near-Edge X-ray Absorption Fine Structure (NEXAFS) or X-ray Absorption Near-Edge Structure (XANES) is determined by the multiple scattering of low energy photoelectrons ($E_{kin} < 30$ eV) having a wavelength comparable with interatomic distances in the system. Major contribution to the NEXAFS is made by interference of photoelectron waves, which are formed as a result of multiple (resonant) scattering of low-energy photoelectrons atoms by the environment. NEXAFS contains information about the spatial structure of the environment of the absorbing atom and the energy distribution of the free electron states in the system, defining the optical, electrical and other physical and chemical properties of matter.

The traditional approach to the interpretation of NEXAFS spectra of solids is based on the use of data about the electronic structure obtained by the band calculations. In such approach the X-ray absorption process is described as the

transfer of electrons from the inner (core) shells of an atom to an unoccupied state in the conduction band. A proceeding of the linear absorption coefficient $\tau(E)$ in this case is given by:

$$\tau(E) \approx \int_S \frac{|M_{ji}(\vec{k})|^2}{|\nabla_{\vec{k}}(E_{ji}(\vec{k}))|} . \quad (2.10)$$

Where, $E_{ji}(\vec{k}) = E_i(\vec{k}) - E_j(\vec{k})$ is energy of the electron transition from core level to the unoccupied state in the conduction band of the crystal, $M_{ji}(\vec{k}) = \int \psi_j^*(\vec{r}, \vec{k}) \vec{r} \psi_i(\vec{r}) d^3\vec{r}$ is dipole matrix element of the electron transition between the core level and states in the conduction band, \vec{k} is electron wave vector in the final state. Transitions between levels are allowed, if the matrix element of the dipole transition is nonzero. In this case, the spectral lines are intense. Transitions between levels are called forbidden transitions, if the matrix element is zero. In other words, transitions are allowed, if $\Delta L = \pm 1$ and $\Delta J = 0 \pm 1$ ($J = 0 \leftrightarrow 0$), where L is orbital angular momentum quantum number and J is total angular momentum quantum number. Despite the name, the forbidden transitions may occur due to the higher multipole or if third bodies, but these spectral intensities are less.

In equation (10) the integral is taken over the surface S in the space vector \vec{k} in which the energy $E_{ji}(\vec{k})$ is constant (equal to the energy of the absorbed quantum). Since the energy of an electron E_i in an inner shell does not depend on the wave vector \vec{k} , then $\nabla_{\vec{k}}(E_{ij}(\vec{k})) = \nabla_{\vec{k}}(E_j(\vec{k}))$. Replacing the value $M_{ji}(\vec{k})$ of some average value at constant constant-energy surface S gives the multiplicative formula for the absorption coefficient:

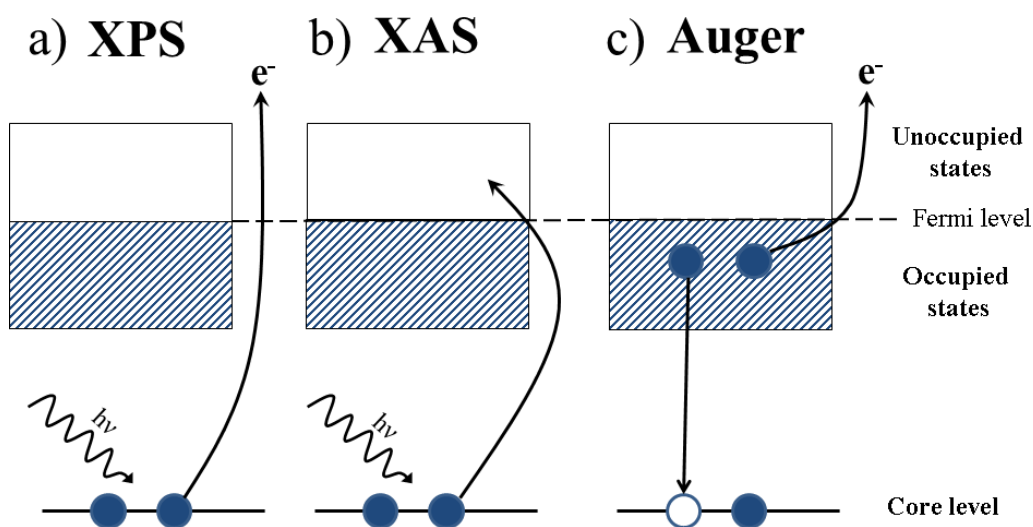
$$\tau(E) \approx \overline{|M_{ji}(\vec{k})|^2} N(E) . \quad (2.11)$$

Where, $N(E) = \int \frac{dS}{\nabla_{\vec{k}} E_j(\vec{k})}$ is the density of the unoccupied electron states in the conduction band of the crystal. The equation (11) allows for a separate discussion of the effect of the density of unoccupied states and the probability of transition to the NEXAFS. A major shortcoming of the band approach is not fully taking into account peculiarities of the electronic structure of solids (the Rydberg series, the discrete bands above the absorption edge, etc.) and the lack of demonstrative relationship between the electronic structure of solids and its components: atoms and molecules.

Modern molecular orbital approach takes into account chemical bonding between atoms and molecules. In this approach an electron in a molecule probability can be at each of the atoms of the molecule with certain and near atom it behaves like a normal atomic electron. Molecular orbital φ_m is represented as a linear combination of atomic orbitals χ_n :

$$\varphi_m = \sum_n C_{nm} \chi_n . \quad (2.12)$$

Where, the coefficients C_{nm} are found from the solution of Schrödinger equation by minimizing the total energy of the system. The squares of these coefficients $|C_{nm}|^2$ equal to the probability of finding an electron in the state χ_n near the atom.



Scheme 2.1. Schematic representation of a) XPS, b) XAS and c) Auger processes.

In Scheme 2.1a simplified XPS process is presented, after photon absorption electron from the core shell is emitted from the sample and then collected by analyzer. In XAS the excited electron stays in a bond states after the photon absorption and provides information about atom's environment (Scheme 2.1b). Unlike previous methods Auger process is a relaxation of a system after excitation. After the filling of the vacancy in the inner core level by an electron from higher level the energy released by the downward transition is given to one of the outer electrons, and this electron is then ejected from the atom with an energy equal to the energy loss of the electron which made the downward transition minus the binding energy of the electron that is ejected from the atom; the kinetic energy of the emitted electron does not depend on excitation photon energy and is unique for each element.

2.5. Scanning electron microscopy.

Scanning electron microscopy (SEM) is a powerful technique to obtain information about the morphology of catalysts. Figure 2.6 shows a schematic of a SEM optical configuration. The instrument must be equipped with a vacuum system. An electron beam is generated from an electron gun. The condenser lens collimates the electron paths and concentrates the electron flux. Then electron beam then passes through a region where its direction can be changed by deflection coils for rastering the beam across the surface of a sample. The objective lens focuses the beam into small spot (ca. 1-5 nm diameter) onto the sample.

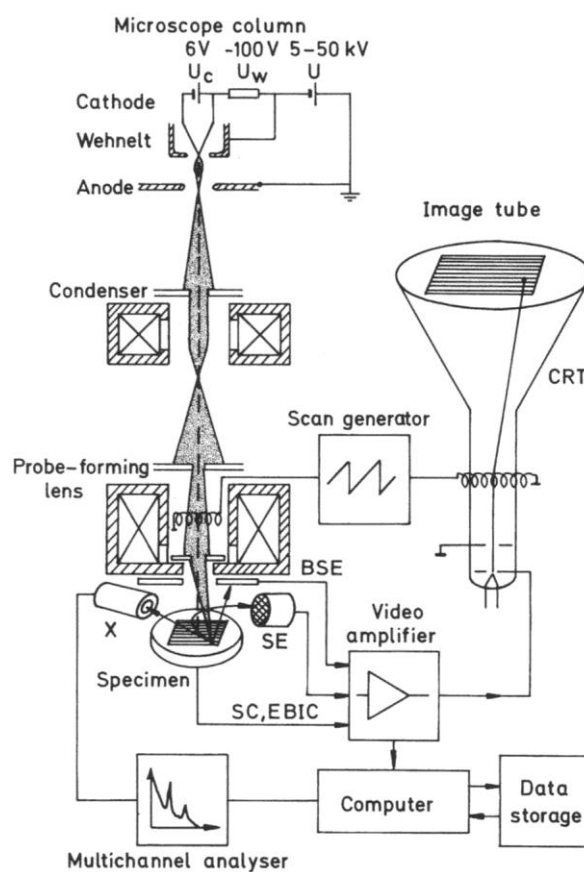


Figure 2.6. Layout of SEM [66].

The interaction between the electron beam and the sample leads to the generation of low-energy secondary electrons, which are collected by the secondary electron detector. The intensity of the electric signal of the detector depends on the nature and the topography (mainly) of the sample in the interaction region. Thus, an

electron beam scanning the surface of an object may obtain a relief map of the analyzed area.

Environmental Scanning Electron Microscope (E-SEM) allows one to obtain an image of the specimen in gaseous environments. A scheme of the specimen chamber in E-SEM is shown in Figure 2.7. This instrument makes it possible to find a correlation between *in-situ* XPS measurements and *in-situ* morphological changes and dynamics. The maximum pressure in the chamber is 30 Pa

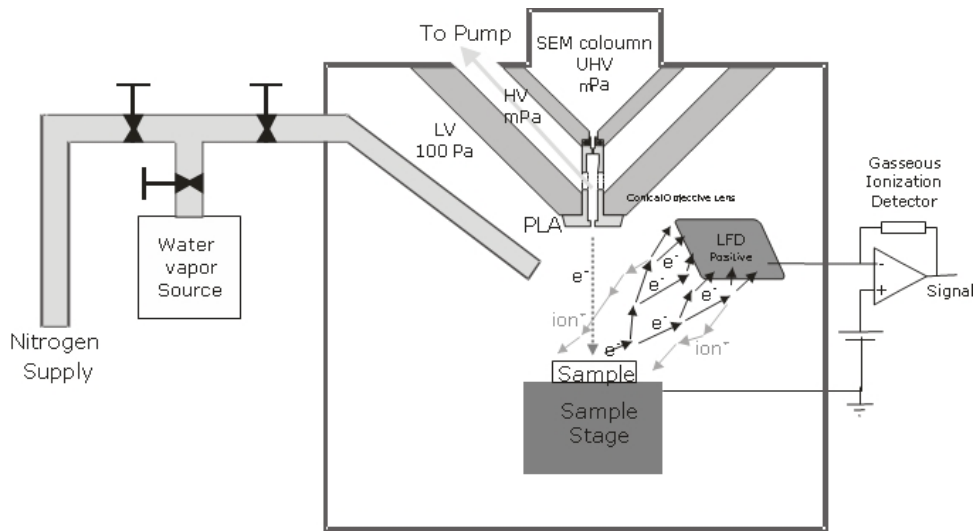


Figure 2.7. The scheme of specimen chamber in E-SEM.

2.6. Transmission electron microscopy.

Transmission electron microscopy (TEM) is microscopy technique in which an image of an ultra-thin sample (thickness about 0.1 microns) is formed by the interaction of an electron beam with the specimen. Subsequent magnification happens in the electromagnetic lenses and recording on the fluorescent screen. The first TEM was created by German electronics engineers Max Knoll and Ernst Ruska in 1931. Ernst Ruska was awarded the Noble Prize in Physics for its creation in 1986.

A cross-section and layout of the optical components in a TEM are shown in Figure 2.8. TEM consists of several components: vacuum system, specimen stage, electron source, high voltage source, electromagnetic lenses, apertures and screen. The typical pressure in TEM is 10^{-4} Pa. There are two main reasons: 1) the possibility of creating a considerable potential between the cathode and the ground

without arcing; 2) increasing the mean free path of the electron gas interaction. The design of the specimen stage includes gateways allowing loading of the sample holder in a vacuum environment of the microscope with minimal increase in pressure. The standard TEM grid size is a 3.05 mm diameter ring with ultramicrotomy sections. In our TEM measurements we used a lanthanum hexaboride filament as the electron source. The LaB₆ filament is heated in order to achieve thermionic emission. The condenser lens system focuses the beam to form a small spot and provides enough magnification (objective lens) to show atomic-scale image.

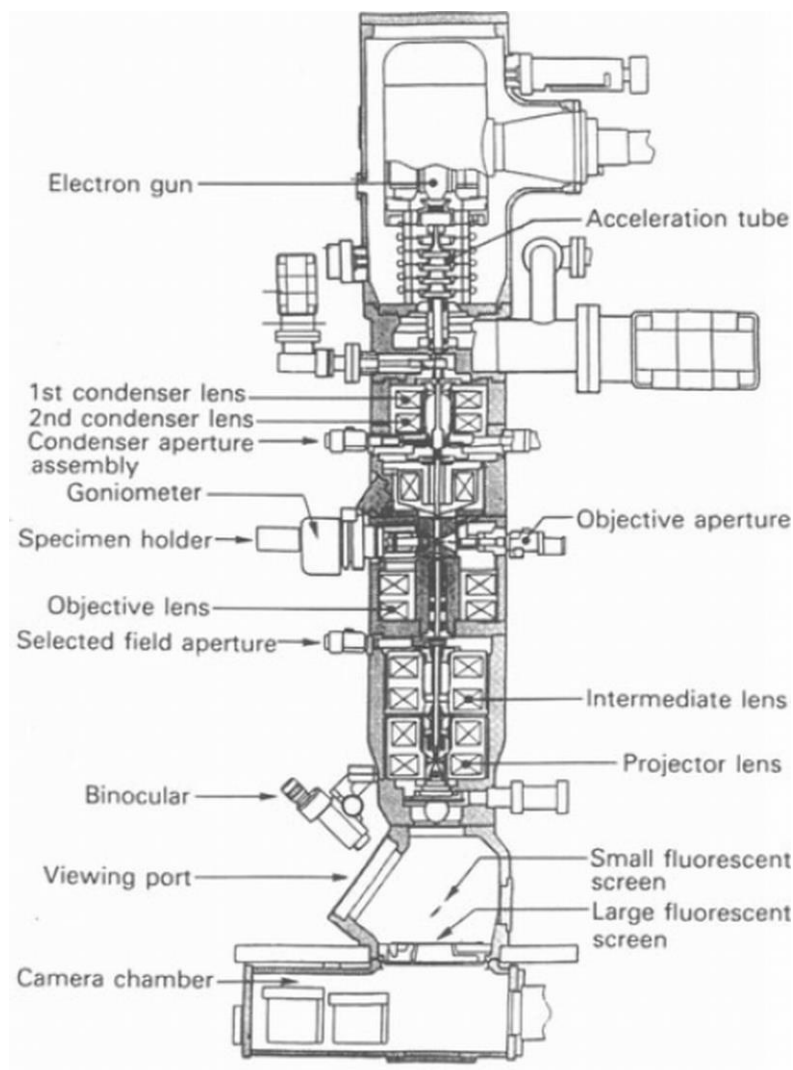


Figure 2.8. Cross-section of TEM [67].

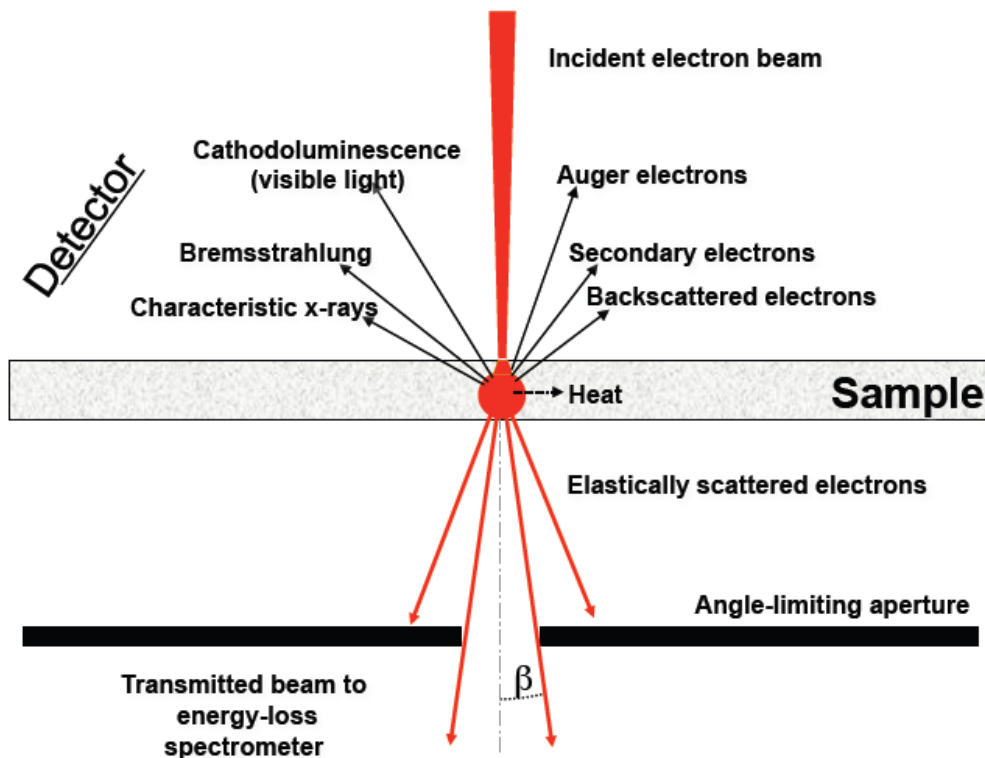


Figure 2.9. Possible signals available in TEM.

A lot of signal can be detected in TEM (Figure 2.9). Commonly TEM collects the following ones:

- 1) Bright field mode: transmitted electrons that leave the sample at relatively low angles with respect to the optical axis. In this mode, thicker regions or regions with higher atomic numbers appear dark in the measured image.
- 2) Electron energy loss spectroscopy (EELS): transmitted electrons that have lost energy when passing through the sample.
- 3) Energy-dispersive X-ray spectroscopy (EDX): X-rays generated from electron excitations in the sample.

It is obvious, that, TEM and SEM have similarities but there are as well some characteristic differences. SEM focuses on the sample's surface, while TEM shows what is beyond the surface. The resolution and magnification of TEM is much better than in SEM, on the other hand SEM provides images with better depth of field in comparison with TEM images. Also TEM requires the specific sample preparation using TEM grid. Both techniques are used for a wide range of scientific applications.

2.7. Quadrupole mass spectroscopy.

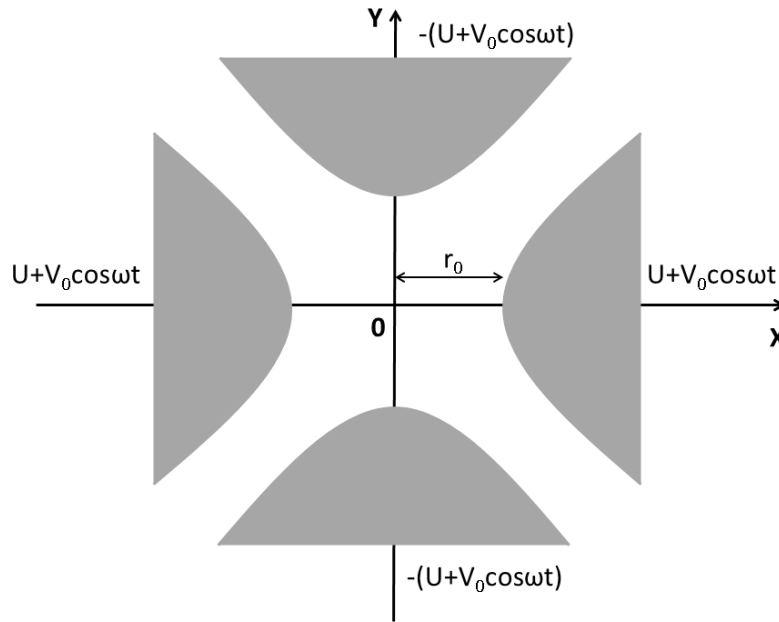


Figure 2.10. End-on view of quadrupole mass spectrometer.

The first mass spectrometer with quadrupole (radio frequency electric field) mass separation (QMS) was developed by Paul and co-workers [68]. An end-on view of a QMS is shown on Figure 2.10. Two pairs of rod-shaped electrodes of hyperbolic cross section establish a two-dimension quadrupole field. The voltage applied to the quadrupole array consists of a constant component U and a radio frequency component $V_0 \cos \omega t$. The motion of an ion injected into the field in the z direction is described by the following equations

$$m\ddot{x} + \frac{2e(U+V_0 \cos \omega t)x}{r_0^2} = 0 \quad (2.13)$$

$$m\ddot{y} + \frac{2e(U+V_0 \cos \omega t)y}{r_0^2} = 0 \quad (2.14)$$

$$m\ddot{z} = 0 \quad (2.15)$$

Equations (2.13) and (2.14) for x and y axes, respectively, can be reduced to Mathieu equation:

$$\frac{d^2x}{dt^2} + (A + 2Q \cos 2\tau)x = 0 \quad (2.16)$$

$$\frac{d^2y}{dt^2} + (A + 2Q \cos 2\tau)y = 0, \quad (2.17)$$

where $A = \frac{8eU}{mr_0^2\omega^2}$, $Q = \frac{8eV_0}{mr_0^2\omega^2}$ and $\tau = \frac{\omega t}{2}$. The solutions of these equations describe ion oscillation in the x and y directions, respectively. However, the velocity in the z direction does not change. The oscillation are stable for certain values of A and Q, it means that the amplitude are finite at any time. But for other values of A and Q the amplitude increases to infinity (the oscillation are unstable). The range of values of A and Q for which the oscillations are stable in x and y simultaneously is indicated in Figure 2.11.

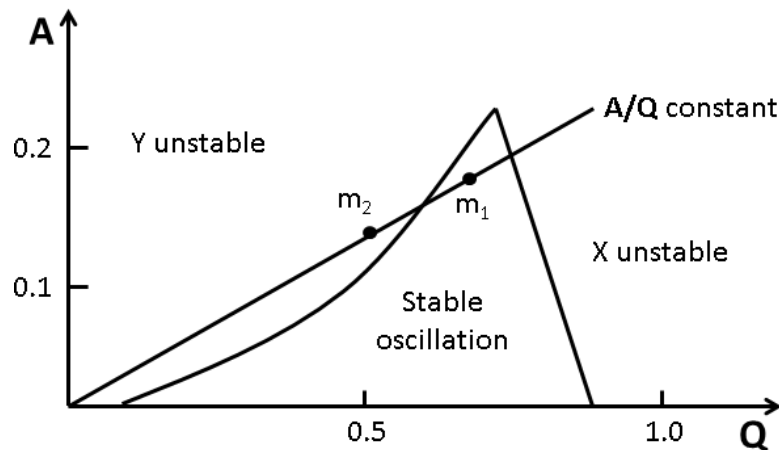


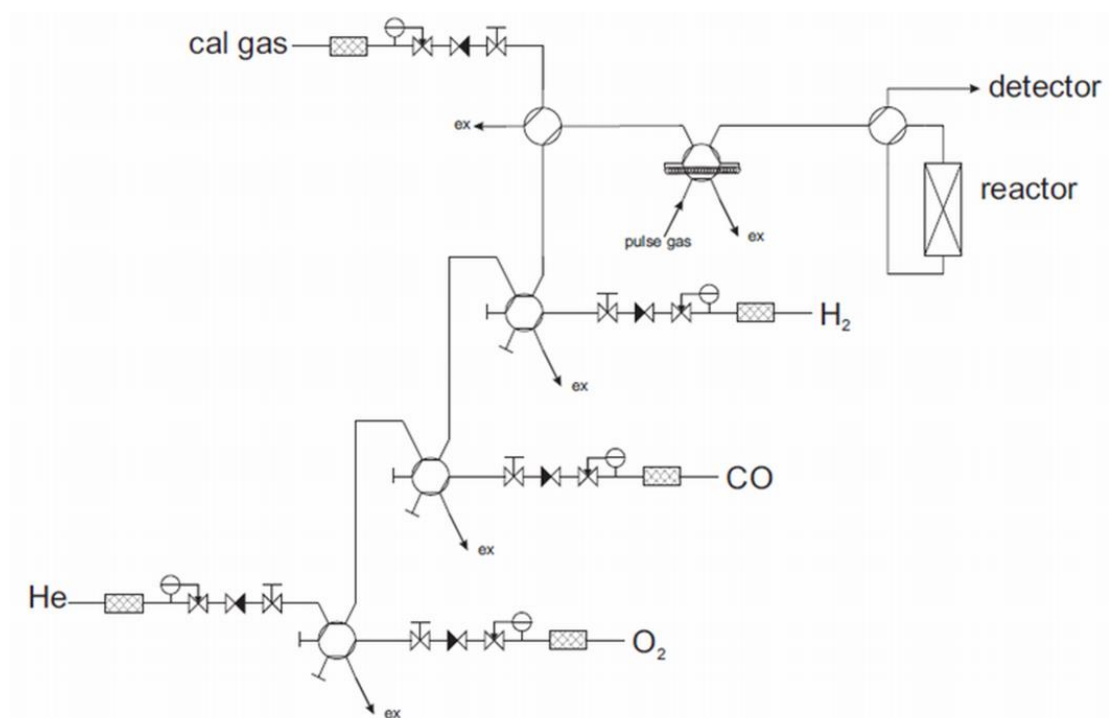
Figure 2.11. Stability diagram for quadrupole mass spectrometer [69].

If the ratio A/Q is constant, the points on the straight line passing through the origin of the stability diagram will represent different ionic masses. For the points inside the region of stable oscillation (mass m_1 in Figure 2.11), the ions with corresponding masses path through the quadrupole field. For other masses (such as m_2 in Figure 2.11), the ions collide with inner parts of the QMS, thus mass separation takes place. To increase the mass resolution, the parameters A and Q are chosen in such way that the representative line passes close to the top of the stability region ($A=0.237$, $Q=0.706$).

2.8 Reactor for CO oxidation at atmospheric pressure.

The catalytic oxidation of carbon monoxide was investigated at atmospheric pressure in a plug-flow fixed-bed reactor. The measurements were carried out in a set-up consisting of a gas dosing section, a reactor tube inside a copper block oven, and an on-line gas analyzer unit. The gas dosing section includes lines for He, H₂,

O₂, and CO and a calibration gas (1% CO, 1% O₂, 1% CO₂ in He). Each line consists of a filter, a mass flow controller (EI-Flow, Bronkhorst), a check valve, and a shut-off valve. The gases are mixed via custom-designed switching valves (Valco, Vici). The reactor itself is a U-tube reactor with an inner diameter of 5mm made of glass lined steel (Glass Lined Tubing, SGE). It is connected to a four-way valve (Valco, Vici) using as bypass. The reactor is heated by a custom-made copper block oven, providing an isothermal (± 1 K) zone of 4 cm at temperatures up to 400 °C. The sample temperature is monitored by an internal thermocouple of type K. Analytics are performed by an on-line detector consisting of IR detectors for CO, CO₂ and H₂O and a paramagnetic sensor for O₂ (X-Stream, Rosemount).



Scheme 2.2. Scheme of reactor for CO oxidation at atmospheric pressure.

2.9. XPS measurement performance.

The XPS measurements were performed at the ISIS beamline at BESSY II/HZB (Berlin, Germany). All measurements were carried out in a stainless steel NAP-XPS chamber described in detail in Chapter 2.2. The powder samples were pressed into a pellet of 8 mm diameter. The Au samples on transition metal oxides were pressed together with a copper mesh into a pellet. The copper mesh was used to

prevent sample charging during photoemission. The samples were mounted on a sapphire sample holder between a stainless steel back-plate and a lid with 6 mm hole, shown in the Figure 2.12. The samples were heated from behind by an infrared laser and the temperature was measured by a type-K thermocouple positioned at the sample's surface. The overall spectral resolution was 0.3 eV in O 1s and C 1s and 0.2 eV in Au 4f regions. The spectral intensity was normalized by the incident photon flux, which was measured using Au reference foil. The binding energies (BE) were calibrated using the Fermi edge, the Au 4f_{7/2} and C 1s second-order peaks. The accuracy of BE calibration was estimated around 0.05 eV.

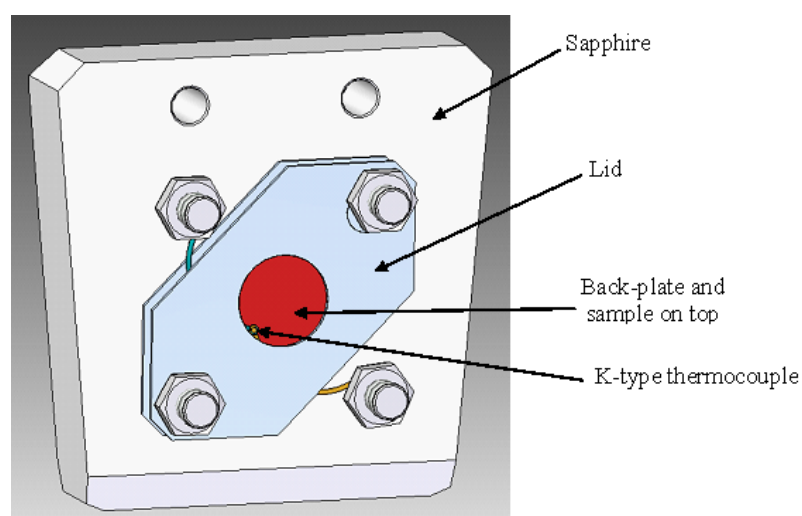


Figure 2.12. Sapphire sample holder with a stainless steel back-plate and a lid with 8 mm hole.

The gold foil was cleaned by standard surface science procedures, with Ar⁺ sputtering ($2 \cdot 10^{-4}$ mbar, 1.5 kV) for 30 min at room temperature and subsequent annealing to 400°C in vacuum. Cycles of cleaning were repeated until carbon was no longer detected by C 1s XPS.

O₃ was produced using a commercial ozone generator TC-1KC. Oxygen was passed at a rate of 1 L/min through Teflon tubing to the ozone generator. The effluent gas from the generator contained a mixture of approximately 1% ozone and 99% un-reacted oxygen. The O₃/O₂ mix was dosed through Teflon tubing into the experimental cell using a leak valve while the sample kept at 100°C. The total pressure in the experimental cell was 0.3 mbar.

All XP spectra were collected in normal photoemission mode. For quantitative XPS analysis, least-squares fitting of the spectra were performed using CasaXPS software (www.casaxps.com). A Doniach-Sunjic line shape for Au 4f_{7/2} and a product (multiplication) of a Gaussian with a Lorentzian line shape for O 1s with Shirley-type background were used to obtain the best fit.

We recorded Au 4f_{7/2} and O 1s spectra at four different kinetic energies: 175 eV, 350 eV, 600 eV and 1000 eV, using a special combination of exit slit width of the monochromator and pass energy of the electron analyzer, which keeps the total resolution almost the same over the relevant interval of kinetic energies. These kinetic energies correspond to inelastic mean free paths (IMFP) of 0.49 nm, 0.67 nm, 0.91 nm and 1.29 nm (assuming predominantly gold in the near-surface region) [70].

3.Results.

3.1. Extended Au surface.

3.1.1. Clean and oxidized Au foil.

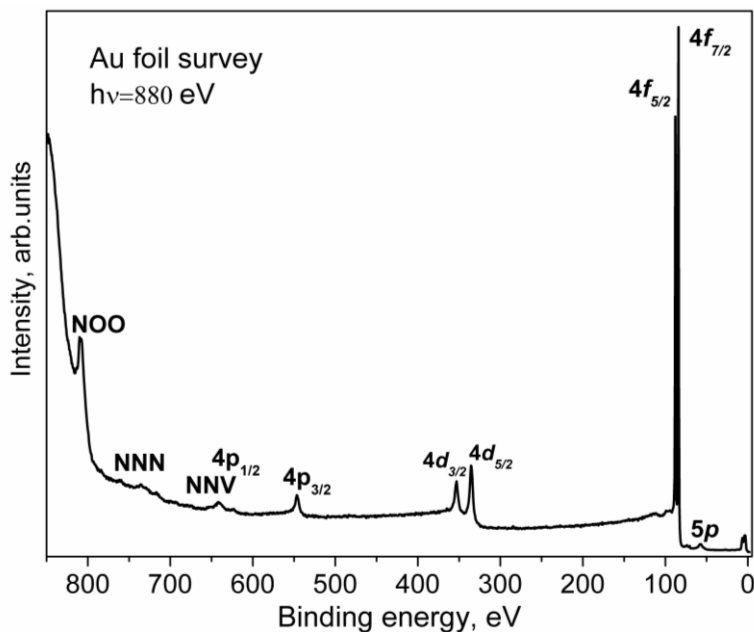


Figure 3.1. Survey photoelectron spectrum of clean Au foil.

The first step to study the interaction of O₃ with Au is to obtain a clean Au surface. The fresh Au foil was cleaned by repeating cycles of Ar⁺ sputtering and thermal annealing until no additional elements other than Au were visible in a broad-energy survey XP spectrum (Figure 3.1). The corresponding Au 4f_{7/2} spectrum of the clean Au foil (Figure 3.2A(i)) shows the expected metallic peak at a binding energy (BE) of 83.92 eV [71-73] together with an additional component shifted by 0.32 eV towards lower BE, assigned as the surface core-level shift according to the literature [74,75]. The surface-sensitive O 1s spectrum (using 150 eV kinetic energy photoelectrons) shows only a small peak but no sign of adsorbed oxygen or oxygenated contaminants. (Figure 3.2B(i)).

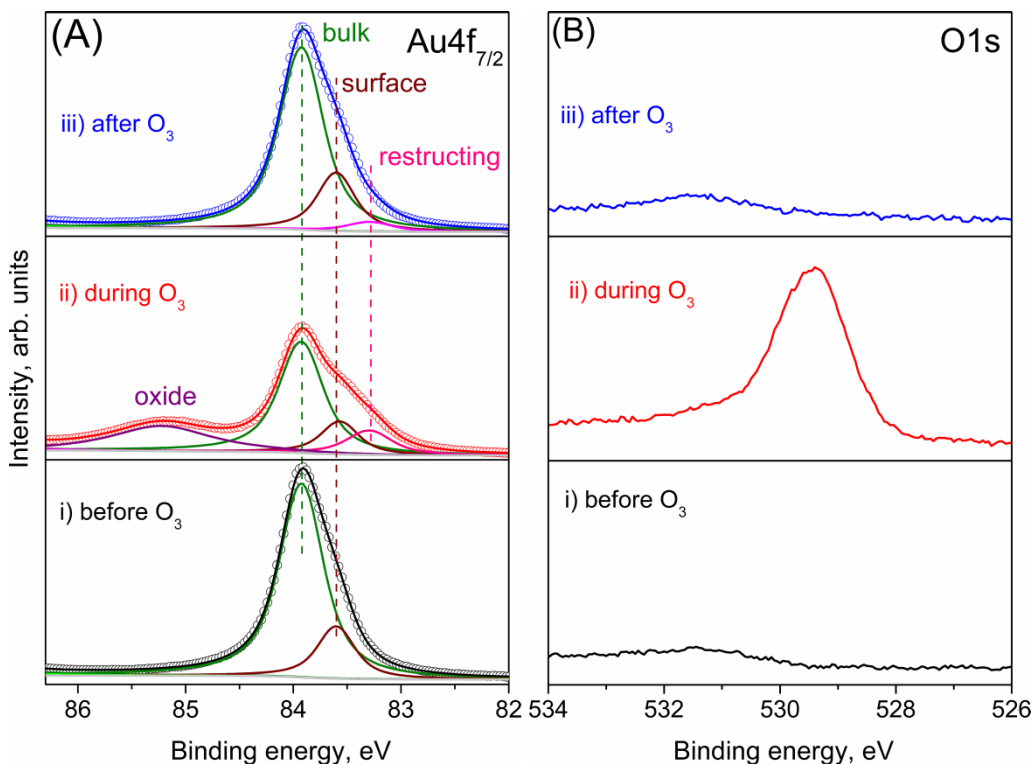
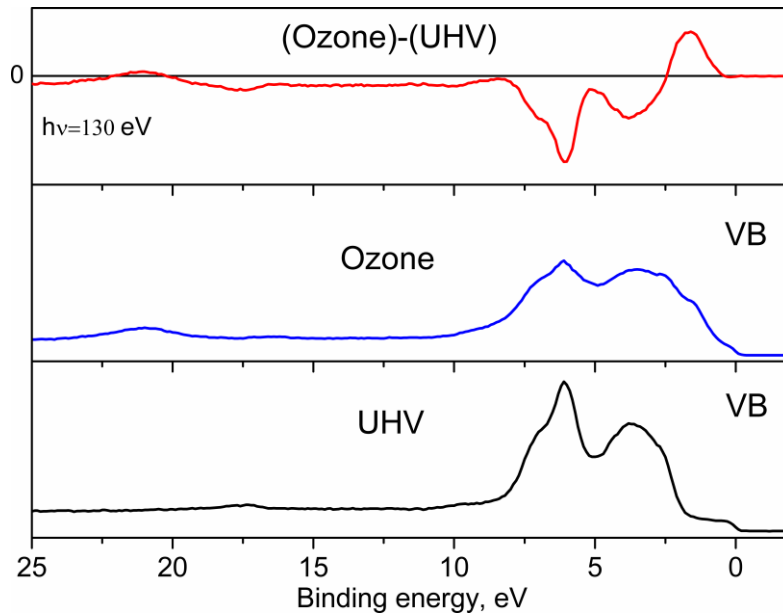


Figure 3.2. Fitting of NAP (a) Au $4f_{7/2}$ and (b) O $1s$ photoelectron spectra (using 150 eV kinetic energy photoelectrons) from gold foil at 100°C (i) before (ii) during and (iii) after O_3 treatment at 0.3 mbar.

When we introduce the O_2/O_3 mixture to the chamber, the O $1s$ spectrum immediately changes, developing an intense peak at 529.4 eV (Figure 3.2B(ii)). The atomic element ratio is $O:Au=0.84\pm 0.05$ within a depth of 0.49 nm. Since no contaminants, within the detection limits of XPS, appear on the Au surface during oxidation, this peak can be assigned as oxygen bonded to gold. The corresponding Au $4f$ spectrum during O_3 exposure (Figure 3.2A(ii)) shows new features in comparison with the clean Au surface. A well-defined peak appears at 85.22 eV, which is assigned to cationic Au species [73,76], together with an additional feature at low BE (83.29 eV). All fitting parameters are given in Table 3.1. This additional component is assigned to the presence of low-coordinated atoms that appear on the Au surface as result of surface restructuring during oxidation [77] (Figure 3.2). This assignment is further discussed below.

Table 3.1. Fitting parameters of Au 4f spectrum of Au foil.

	bulk		surface		restructuring		oxide	
	BE (eV)	FWHM (eV)	BE (eV)	FWHM (eV)	BE (eV)	FWHM (eV)	BE (eV)	FWHM (eV)
Before O ₃	83.92	0.486	83.60	0.415	-	-	-	-
During O ₃	83.92	0.486	83.59	0.415	83.29	0.499	85.22	1.105
After O ₃	83.92	0.486	83.60	0.415	83.29	0.500	-	-

**Figure 3.3.** Valence band spectra in UHV (bottom), in ozone at 0.3 mbar (middle) and difference spectrum between ozone and UHV environments (top) measured at $h\nu = 130$ eV. The spectra were normalized to the Fermi edge jump.

The valence band (VB) spectrum of clean gold foil (Figure 3.3) is in good agreement with results obtained previously [78,79], with slight differences in shape due to the polycrystalline surface and lower total resolution. The spectrum corresponds to the density of occupied *d*-states of Au. Corresponding bands are interpreted elsewhere [80]. Changes in VB spectra are observed after ozone treatment. A difference VB spectrum between oxidized and clean foil shows a decrease in density of occupied Au *d*-states and the appearance of a new structure (BE ~ 3 eV) which corresponds to O *p*-states. This observation confirms that Au oxide is formed, because chemical bonding is accompanied by charge transfer.

Both the cationic Au component and the O 1s peak disappear when the O₂/O₃ mixture is removed and the chamber reaches high vacuum (HV) conditions, as shown in the top spectra of Figures 3.3A and 3.3B. Even the higher chemical potential of 0.3 mbar of O₂ at 100°C instead of HV does not prevent the decomposition of the surface oxide. Under O₃, the Au oxide is stable from room temperature up to 250°C. At higher temperatures the cationic Au component vanishes even in the presence of O₃ as shown in Figure 3.4A. However, as the sample is cooled from 400°C to room temperature, the oxide forms on the surface again at temperatures below 300°C (see Figure 3.4B).

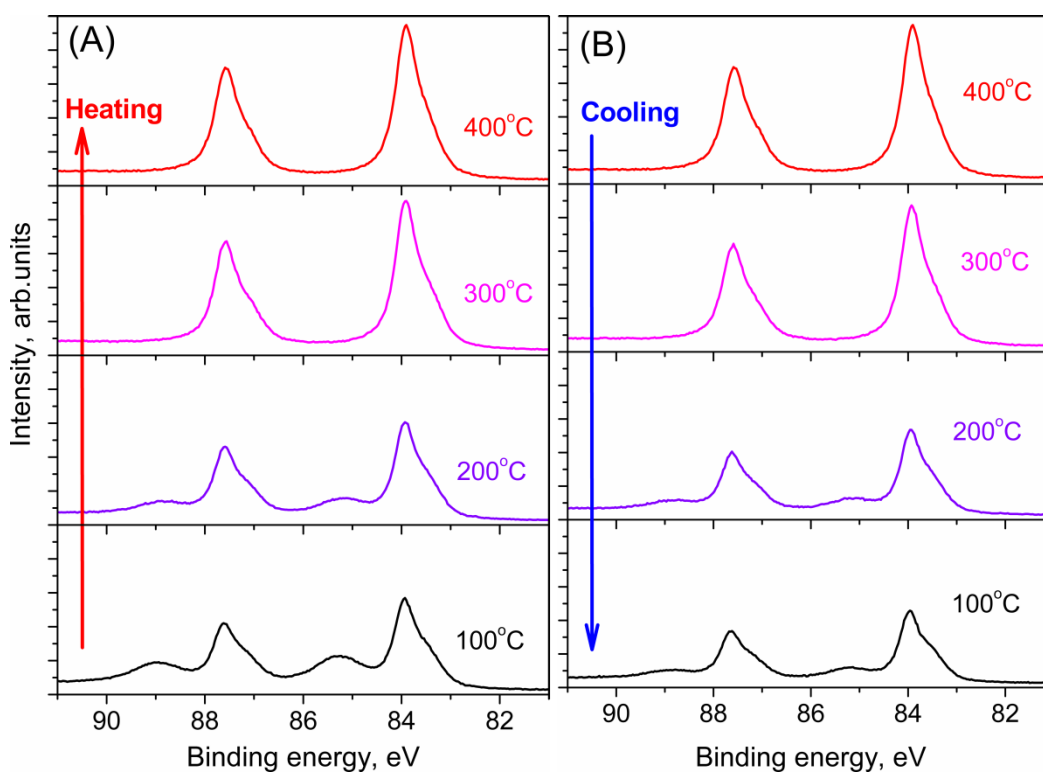


Figure 3.4. Au 4f photoelectron spectra ($h\nu = 270$ eV) from gold foil during heating (A) and cooling (B) at various temperatures measured at 0.3 mbar and CO/O₂+O₃=1/80.

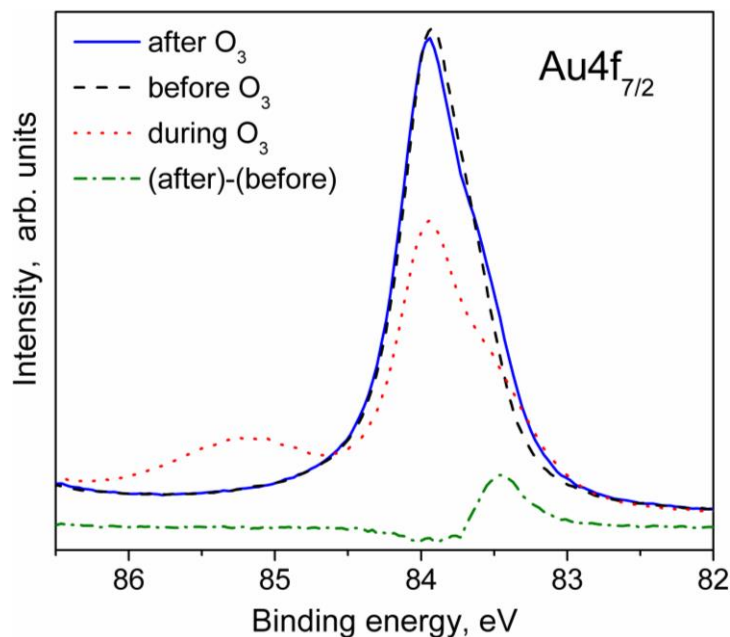


Figure 3.5. NAP-XP Au 4f_{7/2} spectra (using 150 eV kinetic energy photoelectrons) of a gold foil at 100°C before (black dash line), during (red dot line), after (blue solid) O₃ treatment at 0.3 mbar and difference spectrum between Au 4f_{7/2} after and before O₃ treatment.

Interestingly, although the oxide phase totally vanishes after O₃ is removed; the Au 4f spectral shape is not exactly the same as before O₃ treatment. The Au 4f_{7/2} peak is slightly broader (FWHM changes from 0.59 eV before O₃ to 0.64 eV after) with a more pronounced tail to low BE (Figure 3.5). Difference spectrum before and after ozone oxidation (Figure 3.5) clearly shows the existence of an additional component at 83.29 eV assigned to restructuring. At 100°C, the initial spectrum is recovered only after 4.5 h (Figure 3.6), but at 350°C the additional low BE features disappears after 10 min. The persistence of the additional low-BE component even after the decomposition of the oxide phase and its removal by thermal annealing reinforces the assignment as an additional surface core-level shift related to restructuring.

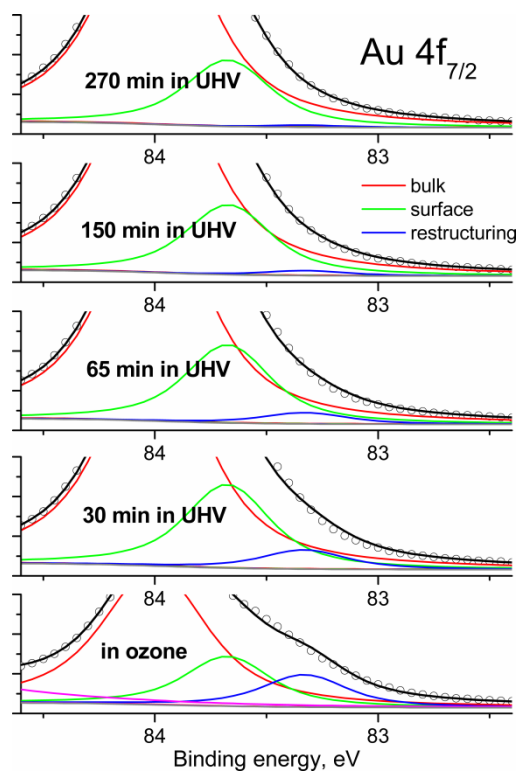


Figure 3.6. Au $4f_{7/2}$ photoelectron spectra ($h\nu = 270$ eV) of a gold foil at 100°C in UHV after ozone treatment.

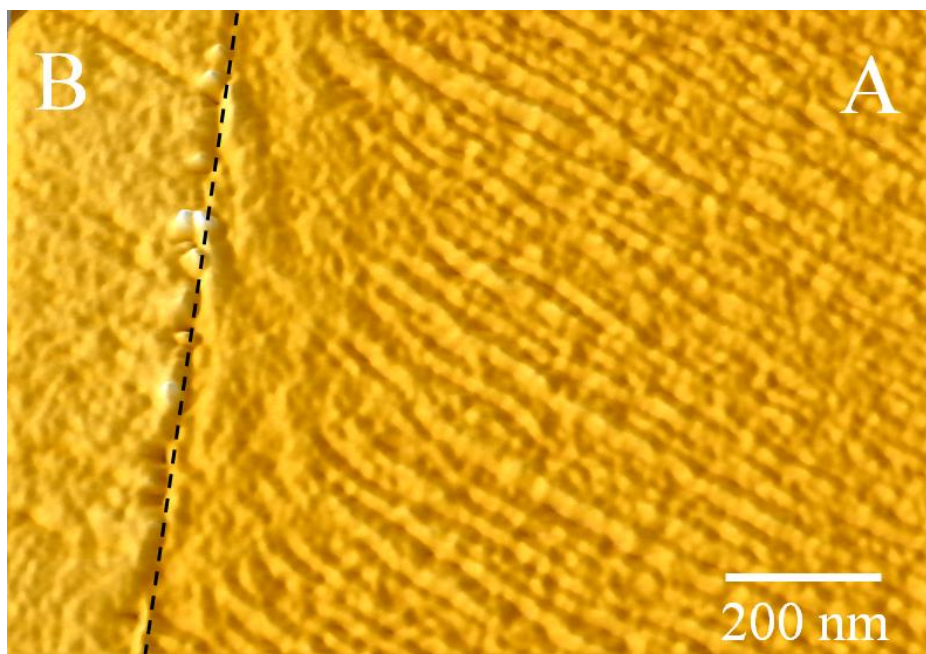


Figure 3.7. *Ex-situ* SEM image of a Au foil after O_3 (0.3 mbar) treatment at 100°C showing ridges only in areas that were exposed to O_3 (region A). On the left side, where the surface was covered by the sample holder lid, no ridges are observed (region B).

The structural modifications of the Au foil after O₃ exposure, as suggested by the XPS results, were further confirmed by *ex-situ* SEM characterization. Figure 3.7 shows an image of a particular region of the Au surface that was partially covered by the sample holder lid. The nearly vertical line marks the position where the edge of the steel lid was pressed against the Au foil. The region of the sample that was exposed to O₃ (region A in Figure 3.7) shows pronounced contrast variations that are consistent with the presence of ridges on the Au surface. Conversely, the region that was shadowed by the lid shows a rather uniform contrast suggesting a less-structured surface on this length scale (region B in Figure 3.7).

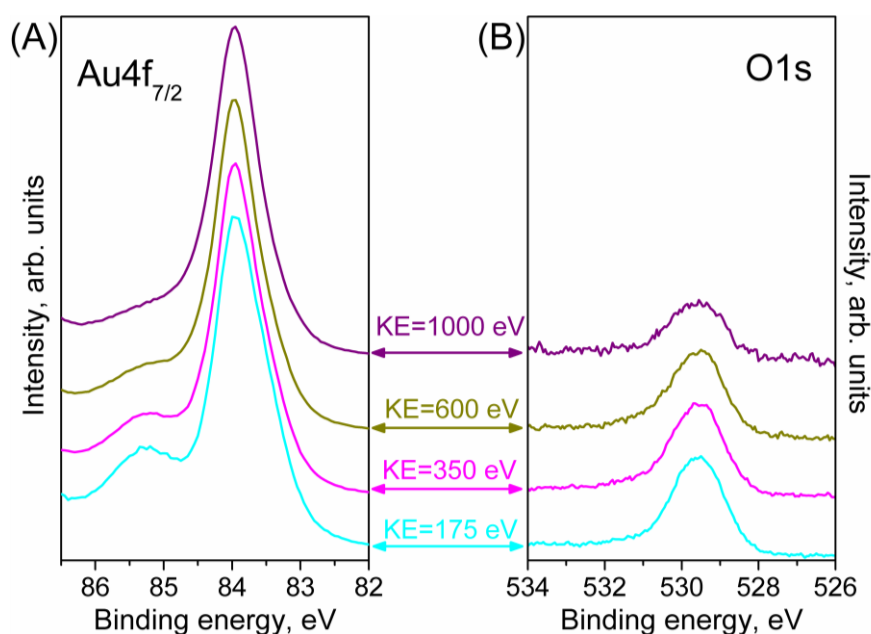


Figure 3.8. NAP-XPS depth profile (a) Au 4f_{7/2} and (b) O 1s as obtained from a gold foil during O₃ (0.3 mbar) treatment at 100°C for increasing kinetic energies of photoelectrons, i.e. decreasing surface sensitivity. Spectra were measured at 175 eV (cyan line), 350 eV (magenta line), 600 eV (dark yellow line) and 1000 eV (purple line) kinetic energy of photoelectrons.

We exploited the energy tunability of synchrotron radiation to measure a depth profile of the sample. By generating photoelectrons of different kinetics energies, the sample could be probed at various depths. Figure 3.8 shows Au 4f and O 1s spectra measured using kinetic energies of 175, 350, 600 and 1000 eV. The O 1s spectra intensity is normalized to the area of the corresponding metallic component Au⁰ in order to emphasize the variations in the total amount of oxygen. It can be clearly

seen that the cationic Au feature and the O 1s peak are consistently less-pronounced for higher-KE photoelectrons, which originate from deeper layers of the Au foil. Moreover, the main peak at 83.95 eV in the Au 4f is more symmetric at higher kinetic energies, which confirms the assignment of the low-BE components to surface related features. These measurements suggest that only the near-surface region of the Au foil is oxidized under O₃ at mbar pressures; however, quantification of the depth-dependent measurements is required for a better assessment of the thickness of the oxide phase.

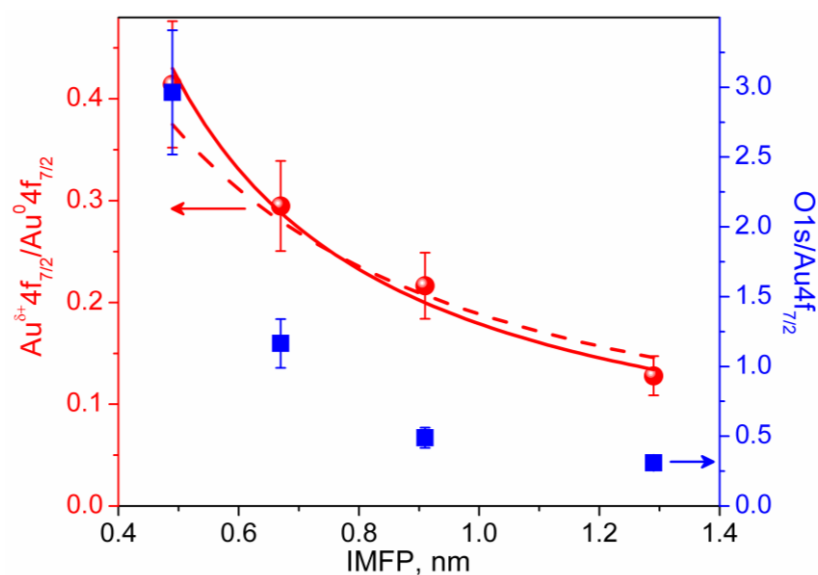


Figure 3.9. The area ratios between cationic Au 4f_{7/2} and Au⁰ 4f_{7/2} (red dots), O 1s and Au⁰ 4f_{7/2} (blue squares) XPS peak as function of inelastic mean free path (IMFP) of Au. Fitting results, assuming an oxide over-layer completely (solid line) and 60% (dash-dot line) covering the Au surface.

The mean escape depth for each measurement at different kinetic energies can be approximated using known values of the inelastic mean free path* (IMFP) for Au [70], because there are no data about IMFP for AuO_x in the literature. Depth profiles are constructed from the integrated XPS areas. Figure 3.9 shows the integrated peak areas of the O 1s and cationic Au divided by the Au⁰ area as function of the average escape depth. The normalization by Au⁰ is necessary to remove the influence of elastic scattering in the gas phase that is also energy dependent. The thickness of the

* The IMFP is defined as the distance a photoelectron beam can travel inside the solid before its intensity decays to 1/e of its initial value.

oxide phase can be estimated by quantification of the depth profile using a simplified structural model consisting of a uniform oxide layer of thickness t over a semi-infinite substrate [60,81]. Using known atomic densities and assuming the same IMFP for the metal and oxide, the unknown thickness t can be obtained by fitting the experimental data.

For calculation we use the equation for semi-infinite specimen, with uniform over-layer of thickness t_A [81]. Suffixes S (support, Au⁰) and A (active over-layer, cationic Au) are used to specify the nature of the atomic species. Over-layer/substrate ratio:

$$\frac{N_A}{N_S} = \frac{F_A \rho_A \sigma_A \lambda_{Aa}}{F_S \rho_S \sigma_S \lambda_{Sa}} \times [1 - \exp(-t_A / \lambda_{Aa} \cos \theta)] \exp(t_A / \lambda_{Sa} \cos \theta), \quad (3.1)$$

where F , dependent on the emitted electron energy, includes several instrumental parameters; ρ , the atomic density; σ , the differential cross-section; λ , IMFP; where θ is the emission direction angle with respect to the surface normal. Equation 3.1 applies to several situations, including growth on metal [60].

In our calculation we use the following parameters: $F_{Au^0} = F_{Au^{\delta+}}$; $\lambda_{Au^0} = \lambda_{Au^{\delta+}}$; $\sigma_{Au^0} = \sigma_{Au^{\delta+}}$; $\rho_{Au^0} = 5.9 * 10^{22}$ atom/mol; $\rho_{Au^{\delta+}} = 3.09 * 10^{22}$ atom/mol ; $\theta = 0^\circ$. By assuming the oxide over-layer completely covers the Au surface, a good fit was obtained (solid line in Figure 3.9) and gave a value of $t = 0.29 \pm 0.02$ nm. However, similar models with incomplete coverage of the surface by the oxide phase (patches) also result in reasonable fittings within the experimental errors, resulting in larger values for the thickness. In the extreme case of 60% coverage (dash-dot line in the Figure 3.9), the derived over-layer thickness increases to 0.58 nm (lower coverages do not result in reasonable fittings). Comparing these values to the shortest Au-O distance of 0.201 nm in the Au₂O₃ structure (most stable bulk Au-oxide) or the smaller axis of its unit cell of 0.404 nm [82], it is reasonable to conclude the formation of a surface oxide phase during the oxidation of a Au surface with O₃ at mbar pressures.

The area ratio in both depth profile curves in Figure 3.9 decays exponentially with escape depth; however, the oxygen curve (blue squares) decays much faster than the cationic Au when probing deeper into the sample. This observation suggests the presence of an additional adsorbed oxygen over-layer that totally or partially covers the surface oxide layer/patches.

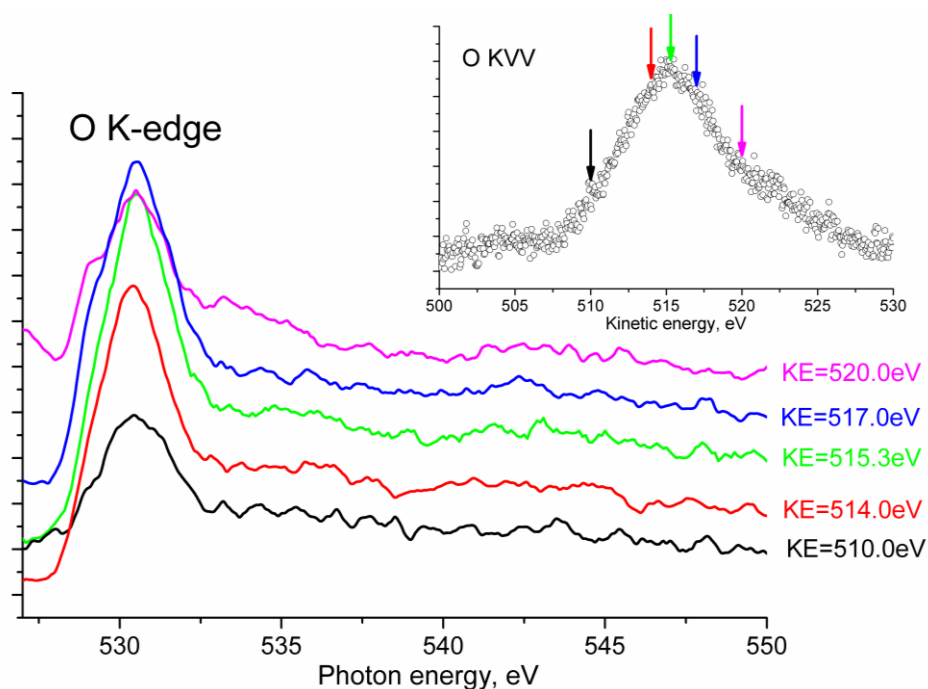


Figure 3.10. O *K*-edge absorption spectra measured in Auger yield mode in O₃+O₂ at 0.3 mbar and 100 °C.

To reveal different oxygen species on the surface O *K*-edge absorption spectra were measured (Figure 3.10). Auger yield mode was chosen as the most surface sensitive mode. Unfortunately all spectra look similar and the signal from the oxygen gas phase dominates [83].

The limiting step in the oxidation of Au seems to be the production of atomic oxygen [25]. Since the dissociation probability of O₂ is very small on Au surfaces [84], atomic oxygen must be supplied by other methods. Recent studies have clearly shown that Au can be readily oxidized when exposed to strong oxidative environments, such as O₂-plasma and UV/ozone [72,85]. The formation of Au oxide has been reported, not only for nanoparticles [86,87], but also for extended Au surfaces, such as single-crystals [86] and polycrystalline thin films [73,76,89]. In our case, the ozone treatment at 100 °C resulted in the formation of a surface oxide phase with a thickness of 1-2 atomic layers, instead of the 3-4 nm thick plasma-oxidized thin films reported by others [73,76,90].

This Au surface oxide is unstable under UHV conditions and in an O₂ atmosphere at 100°C, leaving a clean Au surface when O₃ is removed (Figure 3.3(iii)), in agreement with a previous study [73]. However, under constant O₃

exposure, the surface oxide is stable up to 250 °C. In contrast, based on resistivity measurements, Tsai et al. [76] reported a decomposition half-life time of approximately 10 min for 4 nm Au-oxide films (Au_2O_3) at 100 °C in air. The stability of the surface oxide under an O_3 -containing atmosphere suggests that the surface oxide is in dynamic equilibrium with the gas environment. The constant supply of atomic oxygen, provided in this case by O_3 dissociation, counteracts the spontaneous decomposition and the surface oxide that prevails at higher temperatures. The surface-limited oxidation, observed in our conditions, might be related to this competition between oxidation and reduction/decomposition, and would kinetically limit the oxide growth. This model system under dynamic equilibrium is more representative of a practical catalytic system than static phases under UHV. In the real catalyst, atomic O might be supplied by the oxide support or by direct dissociation of O_2 at the kinks or steps of nanoparticles. It is worth mentioning that we did not observe any X-ray-induced oxidation of Au, as has been previously reported by P. Jiang et al. [91], most likely due to the lower photon flux density in our case that limits beam-induced chemistry. The broad O 1s and cationic Au peaks suggest that the surface oxide is most likely not a single, long-range, ordered phase, but might consist of multiple oxygen species. For example, in the Ag-O system, the co-existence of different oxygen species has been predicted by theory [92] and experimentally verified [93,94]. Similar conclusions — i.e. that several Au-O species can be generated by kinetic control of the oxidation conditions — were drawn by Ming and Friend after reviewing several studies about the oxidation of Au [25].

One of the most controversial aspects of the mechanism of CO oxidation on nano-structured Au catalysts is the source of atomic oxygen. While some authors suggest that a spillover of lattice oxygen from reducible oxide supports is the source of atomic oxygen, others point to the direct dissociation of O_2 at low-coordination sites on the surface of Au nanoparticles [25,87]. The additional surface core-level shift component, related to the restructuring that is observed during ozone treatment in our XP spectra, (Figure 3.3A(ii)) indicate the formation of low-coordinated atoms on the Au surface during oxidation. Similar spectral features were previously observed for stepped single-crystal surfaces [77] with a clear correlation between the

coordination number of atoms at steps and terraces with the measured surface core-level shift for Au(321) and Au(310) crystals. The surface roughening observed by SEM after the O₃ treatment (Figure 3.7) indicates extensive surface restructuring during oxidation, and might have generated the low-coordinated atoms that we had inferred from the XPS analysis. Surface restructuring induced the formation of Au ad-atoms and clusters on a Au(111) surface was directly observed by STM after atomic oxygen exposure, generated by electron-induced NO₂ dissociation [95].

3.1.2. CO oxidation on Au foil.

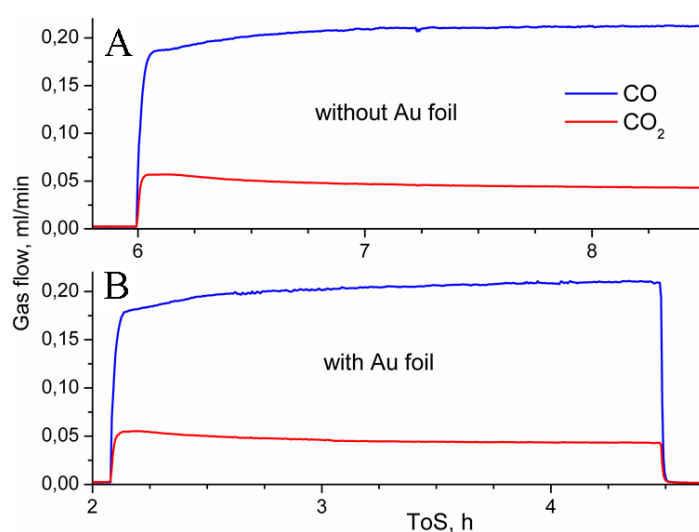


Figure 3.11. The change of the reaction mixture ($\text{CO}/\text{O}_2+\text{O}_3=1/20$) with time a) without Au foil and b) using Au foil as catalyst at 0.3 mbar and 100 °C.

Catalytic properties of Au foil were tested in CO oxidation reaction. The gas mixture ratio was $\text{CO}/\text{O}_2+\text{O}_3=1/20$, temperature was 100 °C and was kept constant during reaction. CO was introduced to the NAP-XPS chamber when O_2+O_3 flow was already provided.

Figure 3.11A shows changes of the reaction mixture with time measured on Au foil. When CO comes in the chamber the corresponding signal increases in QMS. Simultaneously with CO yield the signal of CO₂ increases and remains constant for two hours, it decreases to zero just when CO flow is stopped.

Obvious changes happen with Au 4f photoelectron spectra in reaction mixture (Figure 3.12A). The cationic Au component disappears when the $\text{CO}/\text{O}_2+\text{O}_3$ mixture

is introduced; even presence of O_3 in gas mixture is not enough to reoxidized Au foil. At the same time metallic component at 84 eV recovers and is the same as in UHV after oxidation (Figure 3.2). After 6 min in reaction mixture O 1s spectrum (Figure 3.12B) shows only residual amount of oxygen, thus CO reduces oxidized foil in presence of O_2+O_3 mixture, which may lead to initial increase of CO_2 production.

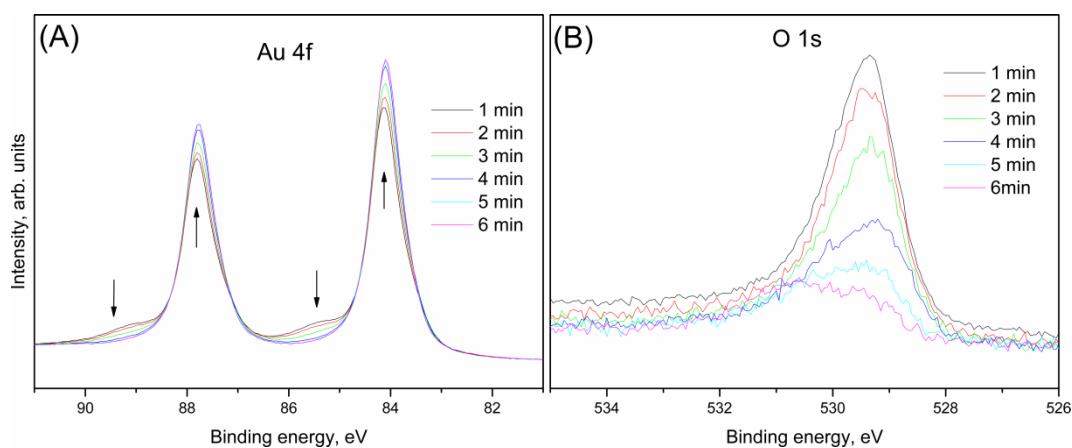


Figure 3.12. Evolution of Au 4f (A) and O 1s (B) photoelectron spectra (using 700 eV kinetic energy photoelectrons) from gold foil at 0.3 mbar and 100°C in reaction mixture ($CO/O_2+O_3=1/20$) with time.

When the same reaction was repeated without Au sample in the chamber (blank reaction) the profile of the gas mixture did not change (Figure 3.11B). The intensity of the signals of CO and CO_2 is independent of presence of Au foil in the chamber, several reasons can cause to this result: 1) reaction yield is below detection limit of the equipment; 2) background reaction dominates; 3) no CO oxidation on gold foil.

3.1.3. Clean and oxidized Au powder.

Since Au foil does not show any activity in CO oxidation at low temperature, we decide to use Au powder to increase surface area of catalyst, which allows making sure that the CO_2 yield is not below detection limit of the equipment. Au powder (<45 μ , 99.95% purity) was pressed to a pellet before mounting on a sapphire sample holder between a stainless steel back-plate and a lid and was loaded to the NAP-XPS chamber subsequently. The experimental parameters used were the same as for Au foil (see Chapter 3.1.1).

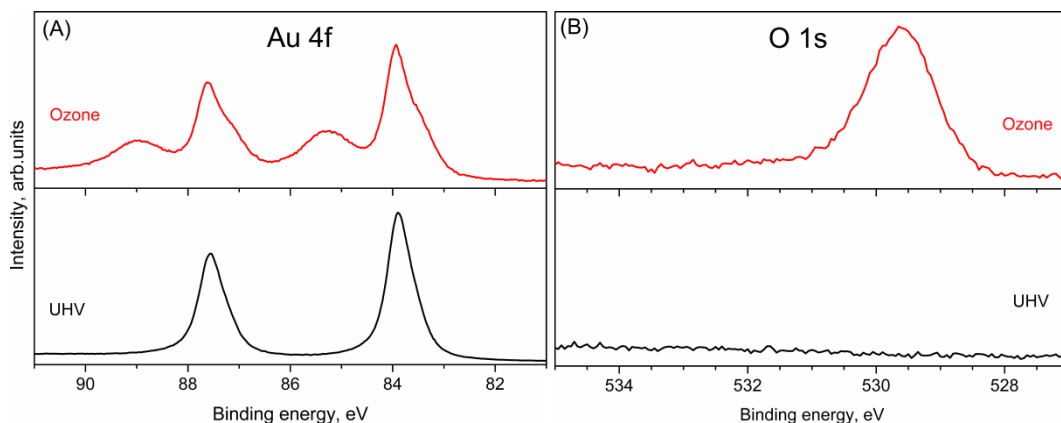


Figure 3.13. Au 4f (A) and O 1s (B) photoelectron spectra (using 150 eV kinetic energy photoelectrons) of a gold powder at 100°C in UHV (bottom) and ozone (0.3 mbar) (top).

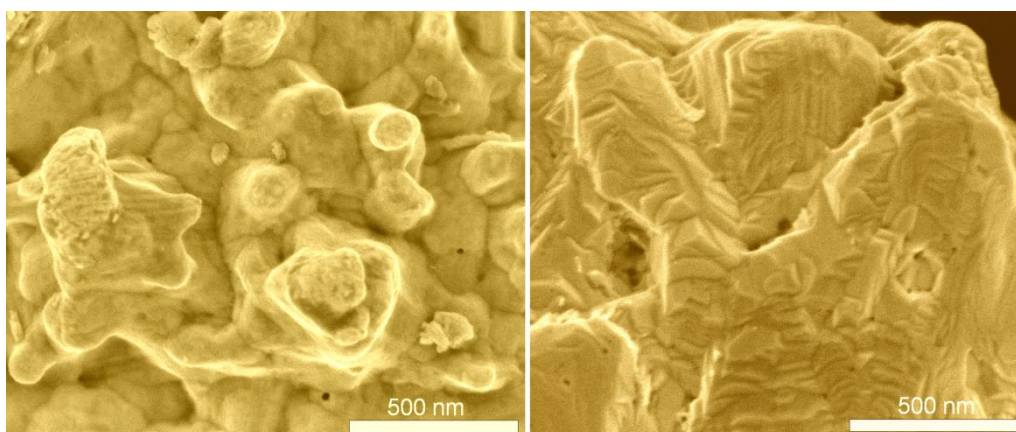


Figure 3.14. SEM image before (left) and after (right) O₃ (0.3 mbar) treatment at 100°C showing restructuring of the gold powder surface.

The gold powder was cleaned by Ar⁺ sputtering to remove possible contamination from the surface. Au 4f spectrum of clean powder (Figure 3.13(A)) replicates the shape of the spectrum of clean gold foil (Figure 3.2(A)). O 1s spectrum does not show any sign of oxygen species (Figure 3.13(B)) when measured in UHV.

Both spectra change immediately in ozone environment (Figure 3.13(top)). A well-defined broad peak of cationic Au species [73,76] appears at 85.2 eV in Au 4f, which is assigned to ionic Au species. The metallic peak (BE 83.95) [71-73] is more asymmetric to low binding energy region, which corresponds to surface core level shift [74,75]. Also high intensity peak arises at 529.4 eV in O 1s spectrum. Therefore

the behavior of oxidized Au powder is similar to Au foil and all results obtained for Au foil can be extrapolated to Au powder.

After O₃ exposure the restructurings of the Au powder can be observed in *ex-situ* SEM image (Figure 3.14). The shape of particles before O₃ treatment is roundish, while kinks and edges are visible after O₃ exposure. Thus we have a lot of low-coordinated atoms on the surface after oxidation.

3.1.4. CO oxidation on Au powder.

Catalytic properties of Au powder were tested in CO oxidation reaction using the similar condition as for Au foil in NAP-XPS chamber.

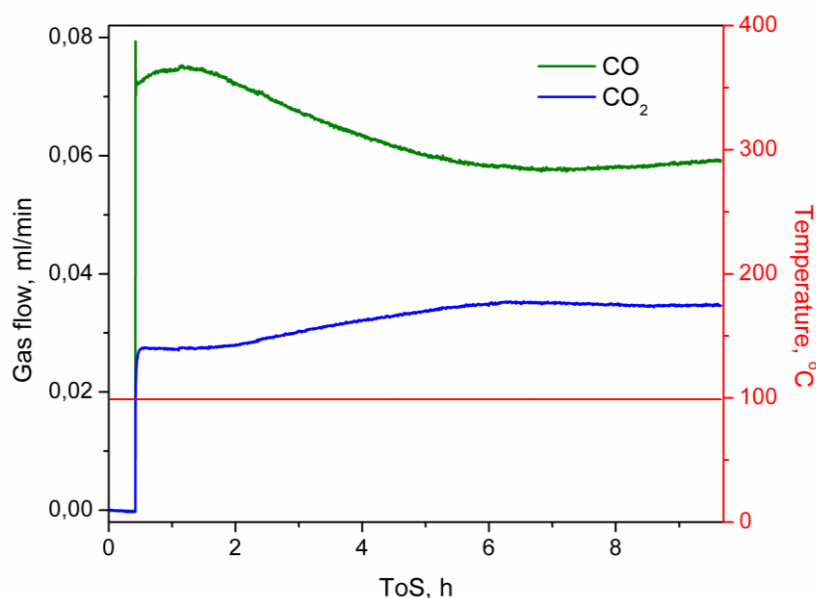


Figure 3.15. The changes of the reaction mixture (CO/O₂+O₃=1/80) with time using Au powder as catalyst at 0.3 mbar and 100°C.

Figure 3.15 shows changes of the reaction mixture with time using Au powder as catalyst. In the beginning the QMS signals of CO and CO₂ increase when CO was introduced in the chamber. After 1 hour approximately CO₂ signal grows slowly and reach plateau after 6 hours, CO signals shows opposite trend at the same time. This behavior clearly shows presence of reaction in the chamber.

During CO oxidation Au 4f_{7/2} and O 1s photoelectron spectra were measured to monitor changes of Au surface (Figure 3.16). We see that after 5 minute exposition in reaction mixture (Figure 3.16 bottom) the Au surface is still oxidized as evidence

by the presence of cationic Au species at 85.2 eV in Au 4f spectrum and broad peak in O 1s. Further exposition shows decreasing of cationic Au component and after 6.5 hours it is totally vanished, that coincide in time with changes of CO₂ flow in QMS. However oxygen species are still visible in O 1s spectrum (Figure 3.16 top) after oxide decomposition, the shape of the peak is more asymmetric and it is shifted to low binding energy region.

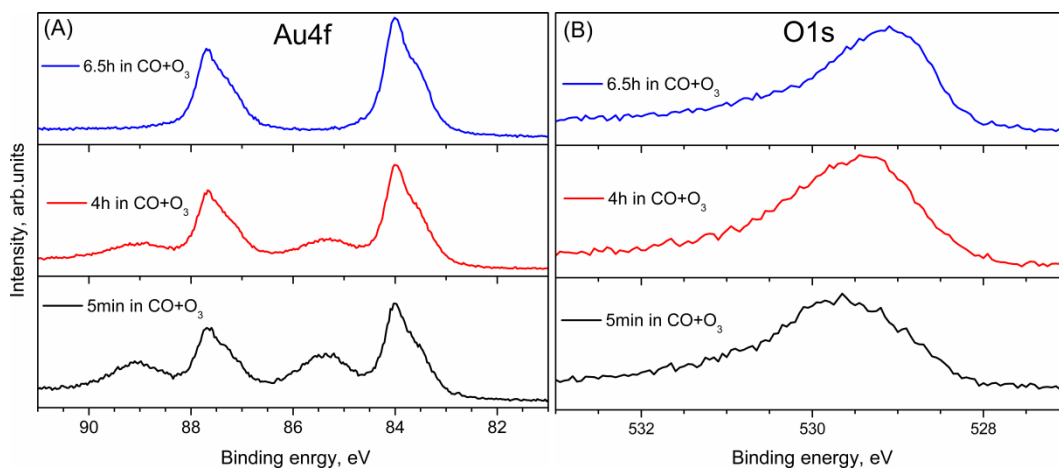


Figure 3.16. *In-situ* Au 4f (left) and O 1s (right) photoelectron spectra (using 150 eV kinetic energy photoelectrons) of gold powder at 100°C during CO oxidation at 0.3 mbar.

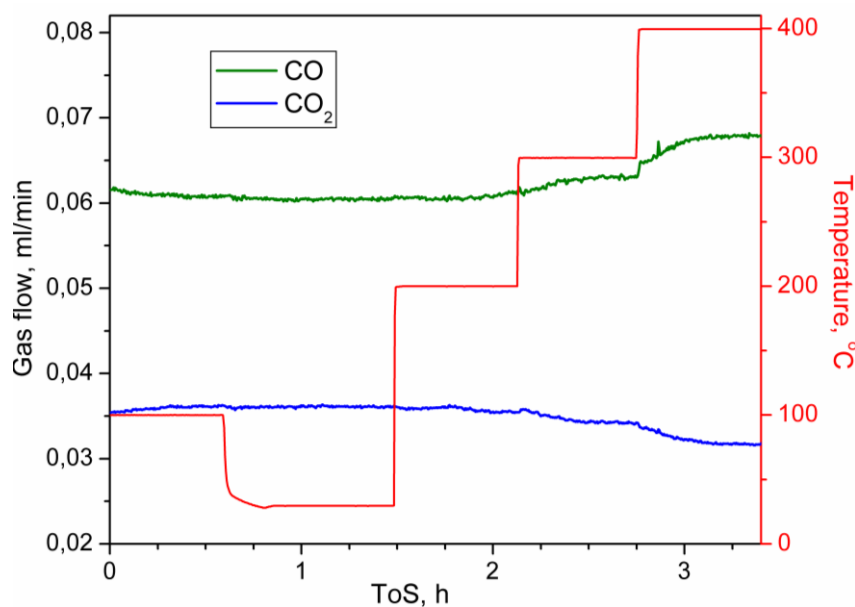


Figure 3.17. CO oxidation on Au powder at 0.3 mbar and different temperature.

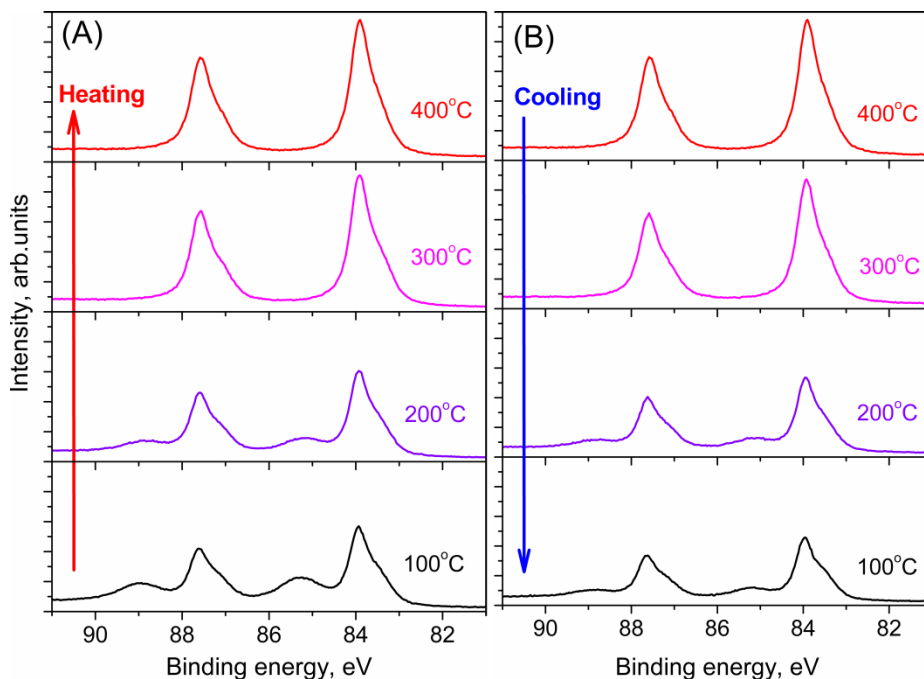


Figure 3.18. Au 4f photoelectron spectra ($h\nu = 270$ eV) from gold powder during heating (A) and cooling (B) at various temperatures measured at 0.3 mbar and $\text{CO}/\text{O}_2+\text{O}_3=1/80$.

To study CO oxidation on Au powder in detail the reaction temperature was varied (Figure 3.17). From room temperature to 200 °C, variations of CO_2 flow are tiny. At 300°C the conversion of CO to CO_2 decreases, further temperature increasing leads to reduction of CO_2 rate. The changes happen only when the temperature is tuned and then the flows are kept stable. Therefore performance of CO oxidation depends on temperature, it decreases with temperature. XP spectra of Au powder (Figure 3.18) show similar behavior to Au foil (Figure 3.4) during heating and cooling.

Since CO oxidation at different temperature does not shed light on active sites of Au, it was decided to vary the gas mixture. In Figure 3.19 CO oxidation ($\text{CO}/\text{O}_2+\text{O}_3=1/80$) on Au powder with and without O_3 in gas mixture is shown.

High conversion of CO is observed in O_3 containing atmosphere. After 1.5 hours the ozone generator was switched off, that did not change pressure in the chamber. Evacuating O_3 from the gas mixture leads to slow decreasing of CO_2 yield and CO_2 signal does not reach minimum after 1 hour. The explanation can be the following: the residual O_3 in the Teflon tube still comes in the chamber even after the

generator is switched off. When ozone generator was switched on again—occurring at a ToS of 2.7 hours in Figure 3.19 - CO₂ signal reaches initial value immediately. This experiment shows that O₃ reacts with CO very well. The temperature dependence in the Figure 3.17 becomes clear, because O₃ is not stable compound at high temperature [96]. The less O₃ concentration in the mixture, the less CO conversion.

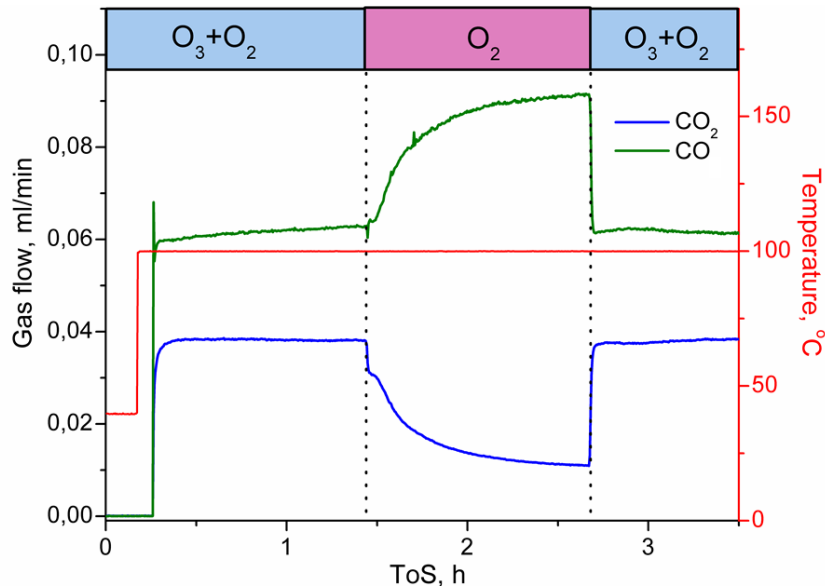


Figure 3.19. CO oxidation ($\text{CO}/\text{O}_2+\text{O}_3=1/80$) on Au powder with and without O₃ at 0.3 mbar and 100 °C.

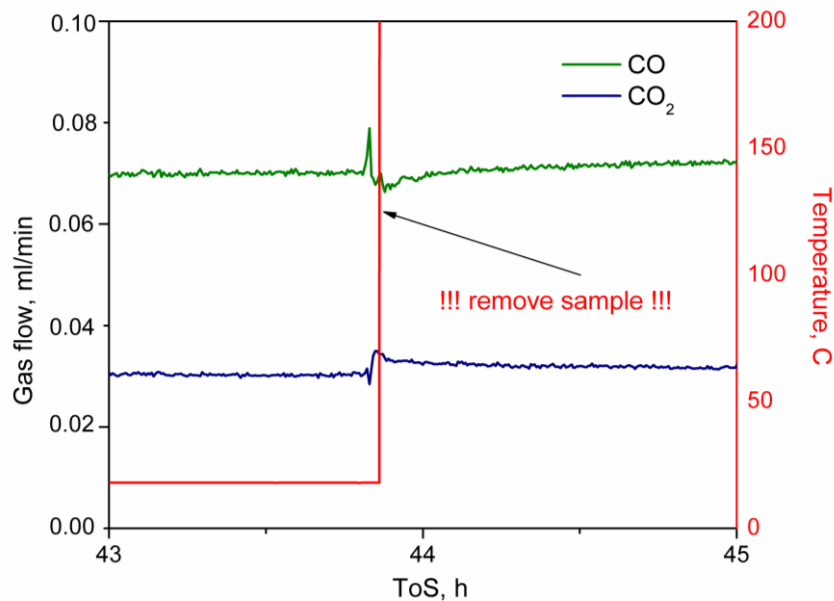


Figure 3.20. Gas mixture changes while removing Au powder out of the chamber.

The role of Au powder in CO oxidation is still unclear; therefore the simple test was done. The sample containing Au powder was removed from the chamber without stopping the reaction (Figure 3.20). No difference in the gas yield, so we conclude that background reaction dominates and the role of Au powder is negligible.

3.1.5. Conclusions.

The obtained spectroscopy and microscopy results can be interpreted by the restructuring of the Au surface as reported by others, suggesting the presence of low-coordinated atoms on the surface of the Au foil after ozone treatment. However, it should be stressed that the presence of such proposed active sites for molecular oxygen dissociation does not prevent the disappearance of the Au-oxide when O₃ is removed at 100°C. Although, the low-coordinated atoms may have an enhanced interaction strength with surrounding molecules, and still might play a role in O₂ adsorption at room temperature, our results do not show that they enhance O₂ dissociation. This observation suggests that low-coordinated Au sites alone might not dissociate molecular oxygen as efficiently at room temperature [32,95] or the number of active sites was not sufficient to compensate for the thermal decomposition of the oxide, unlike the case of O₃ dissociation.

From the results presented we suggest the following picture of the system gold-ozone under a constant chemical potential of O₃. The surface consists of an overlayer of oxygen being chemisorbed on a surface oxide by a thickness of 0.29 nm. This layer may be presented as a tri-layer oxygen–gold–oxygen with a region of oxygen atoms diffusing in deeper layers with decreasing probability. The formation of the surface oxide mobilized gold atoms leading to a significant restructuring of the surface and the frequent formation of coordinatively undersaturated species, which leads to shape changes in the Au 4f spectra. These species may be responsible for holding the atomic oxygen at the surface. Whereas the restructuring remains upon lowering the chemical potential of oxygen to vacuum levels, the absorbed oxygen species and also the surface oxide vanish even at 100°C indicating that the heat of adsorption and heat of formation respectively are small even in the presence of the

massive restructuring. This sheds light on the energetic consequences of the formation of coordinatively undersaturated gold species.

We prefer such a picture of a laterally homogeneous multi-layer architecture over the alternative of laterally inhomogeneous patches of different surface oxide species as the SEM image does not reveal indications for extensive lateral inhomogeneity.

3.2. Au nanoparticles on oxygen-free support.

3.2.1 Au/HOPG.

It was shown in the previous chapters, that extended Au surfaces are inactive in CO oxidation reaction, even after oxidation. But physical and catalytic properties of Au change with size reduction to nanometer. In the last decade, Au NPs, particularly below 5 nm in size, attracted attention for unique catalytic properties [97-99]. Since real catalysts are very complex system a lot of factors, such as size, support, method of synthesis, etc., may influence their performance. Therefore, systematic studies of these parameters are necessary. In the present thesis Au on oxygen-free support were chosen as model catalyst with no Au-support interaction to study the catalytic properties of nanosized Au.

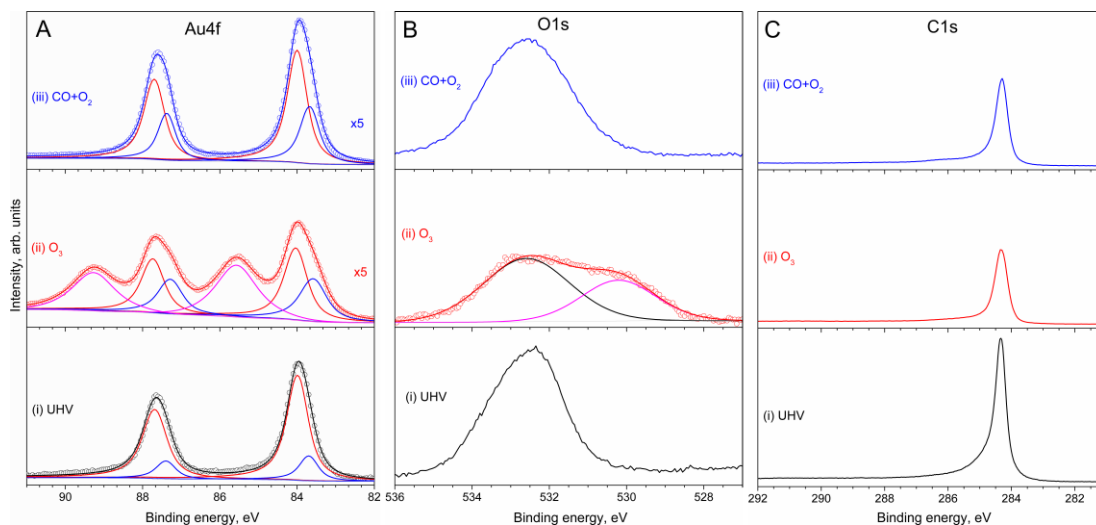


Figure 3.21. NAP (a) Au 4f, (b) O 1s and (c) C 1s XP spectra of Au/HOPG (i) in UHV at RT, (ii) under O₃ at 0.3 mbar, 100 °C and (iii) under CO and O₂ (CO:O₂=1:75) atmosphere at 0.3 mbar, RT.

Model Au/HOPG (highly oriented pyrolytic graphite) catalysts were prepared inside a preparation chamber attached to a photoelectron spectrometer (Novosibirsk, Russia) which was built by SPECS (Germany). The analyzer chamber was equipped with a hemispherical analyzer PHOIBOS-150-MCD-9, an ellipsoidal monochromator FOCUS 500 and an X-ray source XR 50 M with double Al/Ag

anode. The three-step preparation procedure, previously used to prepare Ag/HOPG model catalysts, as described in detail elsewhere [100], was used to prepare Au/HOPG model catalysts. This procedure consists of an initial stage of defect formation on the HOPG surface by soft Ar⁺ sputtering followed by Au deposition and surface annealing at T = 300 °C in UHV (for Au NPs stabilization). The Au nanoparticle size was varied by changing the amount of deposited gold, which was controlled by monitoring the ratio of Au 4f to C 1s XPS peak areas.

The first step to study the Au catalyst is to characterize the freshly prepared samples. Photoelectrons with 150 eV kinetic energy were used to collect surface sensitive Au 4f, O 1s and C 1s spectra in UHV and CO+O₂, and photons with 720 eV energy were used to collect Au 4f, O 1s and C 1s spectra during O₃ treatment (Figure 3.21). Au 4f spectrum of the fresh Au/HOPG in UHV at RT (Figure 3.21A(i)) shows one sharp peak at a binding energy (BE) of 83.95 eV, assigned to bulk Au in the metallic state, according to the literature [71-73]. The component shifted to low BE by the 0.3 eV is assigned to low-coordinated Au atoms [74,75,77]. The corresponding O 1s spectrum shows the presence of oxygen on the surface (Figure 3.21B(i)). The asymmetry of O 1s peak indicates that there are more than just one oxygen specie and the position of its maximum (BE 532.6 eV) suggests the presence of C-O, C=O and/or C-OH bonds [101,102]. C 1s spectrum (Figure 3.21C(i)) shows well-known graphite peak at BE of 284.3 eV [103].

When the O₂/O₃ mixture was introduced into the chamber and the sample was heated to 100 °C, the Au 4f spectrum changed (Figure 3.21A(ii)). A well-defined peak appears at 85.6 eV, which is assigned to an ionic Au species [73,76]; however, with lower BE than that of Au₂O₃ (BE 85.9 eV) [89,104]. Under O₃ the numbers of low coordinated Au atom increasing, this is evidenced by an increase and broadening in low BE peak at 83.5 eV. According to Weststrate et al. [77] the less neighbors the lower BE, in other words an oxidation restructures Au surface and forms low-coordinated Au atoms (for example edges, kinks, etc.) on the surface. The surface sensitive O 1s spectrum (Figure 3.21B(ii)) is broader in comparison with one measured in UHV. The O 1s spectrum in O₃ atmosphere consists of at least two components: the high BE species are associated with carbon-oxygen species or OH groups (BE 532.6 eV) while the low BE component corresponds to oxygen on Au

(BE 530.1 eV) [73,85]. A decrease in the intensity of C 1s spectrum (Figure 3.21C(ii)) is due to decrease of inelastic mean free path of photoelectron in oxygen compared to UHV.

Table 3.2. Surface composition of Au/HOPG at different conditions.

	Au⁰, %	Au³⁺, %	O, %	C, %
UHV	16.5	-	5.0	78.5
O ₃	7.4	4.6	9.5	75.5
CO+O ₂	8.0	-	10.3	81.7

As was shown in Chapter 3.1, all signs of gold oxide vanish when O₃ is evacuated from the chamber. Even an O₂-rich gas mixture (CO/O₂=1:75) does not prevent the decomposition of the oxide (Figure 3.21(iii)). In contrast to the changes found for extended Au surfaces exposed to ozone [105], the Au 4f spectral shape of Au NPs remains unchanged after O₃ treatment (Figure 3.21A(iii)). The low BE components of the Au 4f spectra does not change much, only small intensity decrease, which can be due to sintering or/and carbon accumulation (Figure 3.21C(iii)). Consistently, the peak shape of the O 1s spectrum returns to nearly the same shape as when measured in UHV, but with a slightly broader width due to the formation of new carbon-oxygen species. Note that only oxygen bonding to the carbon remains on the surface.

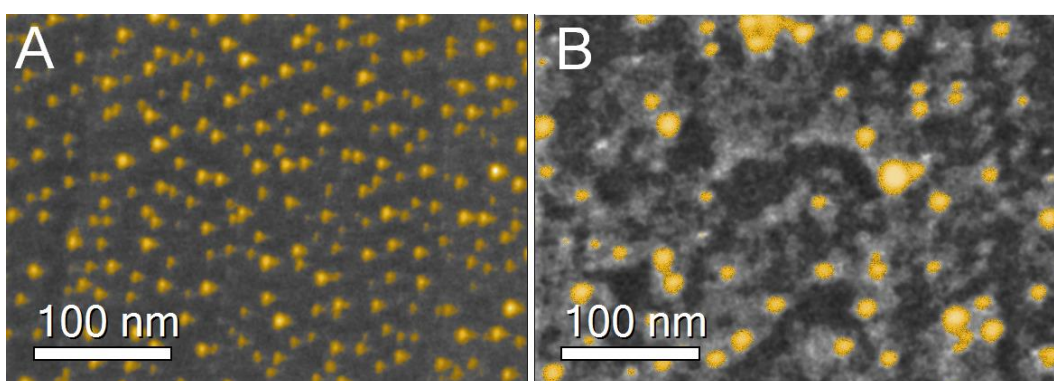


Figure 3.22. SEM image of Au/HOPG a) before and b) after O₃ treatment at 250 °C and CO oxidation at 0.3 mbar. Images were colorized in order to highlight the differences between the two samples.

The quantitative analysis of surface composition is presented in Table 3.2. The dominant element on the surface obviously is carbon at all conditions. The amount of Au on the untreated sample is 16.5%. O₃ treatment leads to oxidation of ca. 30% of Au and significant increasing of oxygen concentration. Decreasing of Au concentration during and after O₃ treatment points out, that the sintering takes place.

The structural evolution of Au NPs during CO oxidation may help to shed light on the origin of Au activation. An SEM image of the untreated Au/HOPG is presented in Figure 3.22A. The image shows Au NPs with a narrow size distribution of 6-8 nm. After O₃ treatment and CO oxidation, the Au NPs are not homogeneously distributed anymore, as shown in Figure 3.22B. The mean particle size is higher (~10 nm) than the fresh sample and some agglomerated particles are visible, which is in good agreement with quantification of the surface composition made by XPS. Burning of graphite at the interface with the Au NPs is accompanied by the migration of metallic particles on the HOPG surface (the tracks are darker in Figure 3.22B). This may occur because the aggressive oxidation by O₃ leads to high mobility of Au NPs due to destruction (burning and oxidation) of carbon surface [106].

To estimate catalytic performance Au/HOPG sample was placed in the NAP-XPS chamber without any pretreatment. Then the reaction mixture (CO:O₂=1:75) was introduced to the chamber (Figure 3.23A). Small fluctuations of CO flow are due to fluctuations of the MFC at very low flow. Initially, the CO₂ yield exhibits a small increase for a short time: we attribute this activity to a reaction between CO and residual O on the HOPG surface. For long time on stream, Au/HOPG does not show any significant activity under the described conditions, therefore we reason that size reduction is not sufficient to activate Au.

We tried to slightly oxidize Au before the reaction, using an O₃ treatment. QMS data is presented in Figure 3.23B, in which Au NPs that were pre-treated with O₃ are exposed to a constant flow of a 1:75 mixture of CO and O₂. The activity of the oxidized sample is much higher than that of the sample not pre-treated with O₃, but a strong deactivation takes place, and after approximately 2 hours the CO₂ yield is negligible. Thus the agglomeration does not influence the activity of Au/HOPG, suggesting that other reasons apart of the structural changes are responsible of the

activation of Au for CO oxidation. We assume that the increase of the CO₂ yield after the O₃ treatment is caused by the stoichiometric reaction between the remaining surface oxygen and CO.

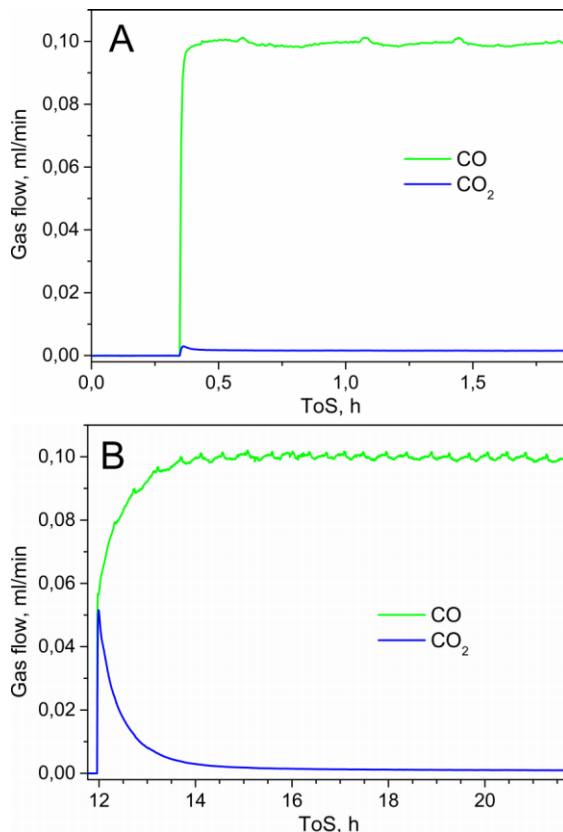


Figure 3.23. QMS data (CO:O₂=1:75) of Au/HOPG a) before and b) after O₃ treatment at 0.3 mbar and RT.

3.2.2 Au/N-CNTs and Au/O-CNTs.

Multi-walled carbon nanotubes were supplied by Applied Science Ltd. 20 g CNTs were treated with 1 L of concentrated HNO₃ under reflux for 4 h. Then the nanotubes were filtrated and washed with distilled water until the filtrate showed a neutral pH. Subsequently, the sample was dried at 110 °C for 3 d in air. N-functionalized carbon nanotubes (N-CNTs) were obtained via a treatment of the previously oxidized nanotubes with NH₃ at 700 °C for 6h. For this purpose 3g of the material were placed in a quartz tube under a flow of 120 ml/min composed of 10% NH₃ in Ar.

5 mg of NaN_3 were dissolved in 10 ml of MilliQ water. Then 6 mg of trihydrate chloroauric acid ($\text{HAuCl}_4 \cdot 3\text{H}_2\text{O}$) were added to the solution, which subsequently turned orange. The ratio $\text{NaN}_3/\text{HAuCl}_4 \cdot 3\text{H}_2\text{O}$ was 5:1. 300 mg of N-CNTs were added to the solution in order to allow the adsorption of the Au precursor on the N-CNTs with a final Au load of 1wt%. The addition of the N-CNTs induced gas release and caused the solution to turn colorless, indicating the decomposition and complete adsorption of the precursor. Afterwards, the N-CNT suspension was filtered and the total precursor decomposition was ensured by photo-treatment with an UV/Vis lamp for 30 min.

10 g Baytubes C150HP were treated with 500 mL of 3 molar HNO_3 (diluted with water from nitric acid 65% (Merck)) at room temperature (RT) for 24 h. Then the O-functionalized CNTs (O-CNTs) were thoroughly washed and filtrated with Millipore water until a neutral pH was obtained. For the synthesis of Au/O-CNTs, 1 g of O-CNTs was impregnated with 6 mL aqueous solution containing 20.2 mg of HAuCl_4 . The slurry was then sonicated in an ultrasonic bath for 10 sec and afterwards the solvent was evaporated slowly at RT in air for 48h. Thereafter, the samples containing the metal precursor were reduced in 20% H_2/Ar gas mixture at 250 °C for 2h, a final Au load was 1 wt%.

The results obtained for Au NPs on nitrogen- and oxygen-functionalized carbon nanotubes (Au/N-CNTs and Au/O-CNTs) are similar to Au/HOPG. The Au particle size was <5nm. The Au NPs on functionalized CNTs consisted of a few large (ca. 40 nm diameter) particles, sparsely distributed along the tubes (Figure 3.24), along with a majority of densely dispersed nanoclusters visible only by scanning transmission electron microscopy (STEM) (Figure 3.25 and 3.26). In these images Au NPs are colorized in order to highlight the difference between CNTs and Au; in case of N-CNTs the Au NPs are atomic distributed, meanwhile Au NPs supported on O-CNTs are 2-3 nm in diameter. Under the same conditions, the fresh samples were inactive for CO oxidation as Au/HOPG, in spite of the significant increase of the catalyst surface area that resulted from the higher support area and Au size reduction. After O_3 treatment, Au/N-CNTs and Au/O-CNTs show the same initial activity profile as discussed for Au/HOPG and, the same rate of deactivation (~2.5 hours) (Figure 3.27).

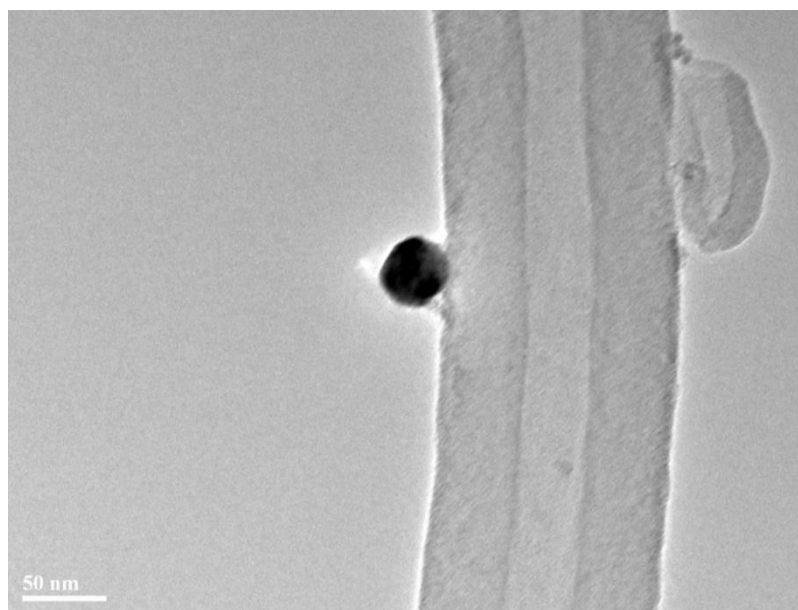


Figure 3.24. TEM image of large Au particle supported on N-CNT.

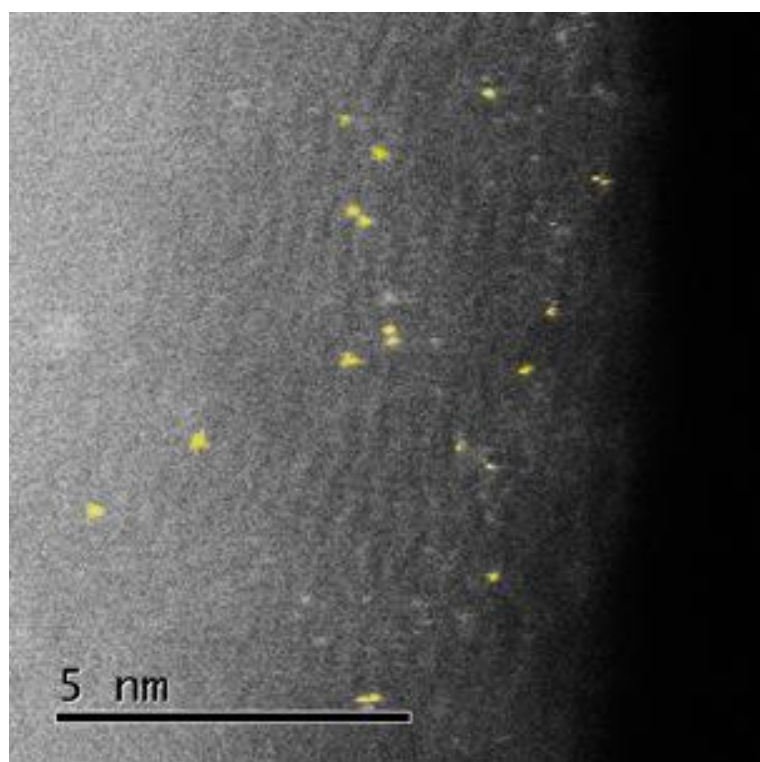


Figure 3.25. STEM image of fresh Au/N-CNTs.

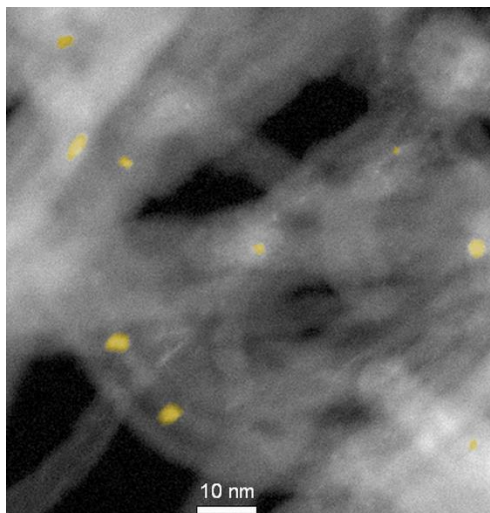


Figure 3.26. STEM images of fresh Au/O-CNTs.

In order to exclude any pressure gap effects, Au-based samples were tested at 1 bar in mixture of CO and O₂ (CO:O₂=2:1) (Figure 3.28). At RT no activity was detected, even increasing the temperature to 473 K does not lead to any CO₂ production. Thus, untreated (fresh) Au NPs supported on functionalized carbon nanotubes are totally catalytic inactive at low temperature in CO oxidation reaction.

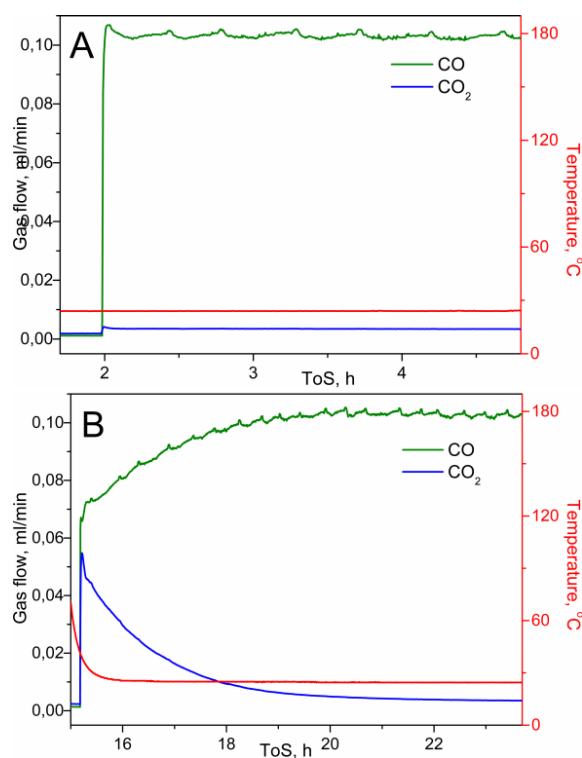


Figure 3.27. QMS data (CO:O₂=1:75) of Au/O-CNTs A) before and B) after O₃ treatment at 0.3 mbar and RT.

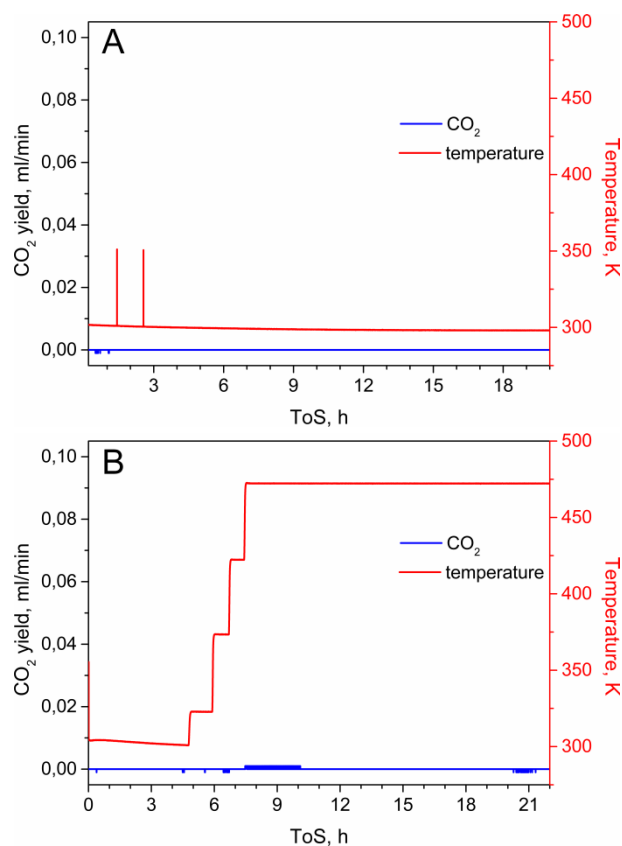


Figure 3.28. QMS data ($\text{CO}:\text{O}_2=2:1$) of a) Au/N-CNTs and b) Au/O-CNTs at 1 bar without any pretreatment.

3.2.3 HOPG

In order to prove that stoichiometric reaction takes place, ‘blank’ measurements were done. A pristine HOPG crystal was placed in the sample holder and all treatment procedures were repeated. Untreated HOPG does not catalyze the oxidation of CO as clearly shown in the Figure 3.29A. However after interaction with O_3 , HOPG demonstrates an initial high CO conversion that strongly decreases with time. After O_3 treatment Au/HOPG produces 1.68 ml of CO_2 in 2.4 h (Figure 3.23), while pure HOPG produces 1.63 ml of CO_2 in 2.4 h (Figure 3.29) after the same pretreatment. The difference is within error bar of the measurements. Since HOPG contains only carbon atoms, the origin of sample’s activity can be attributed only to the stoichiometric reaction between chemisorbed oxygen on the HOPG surface and CO in the gas phase.

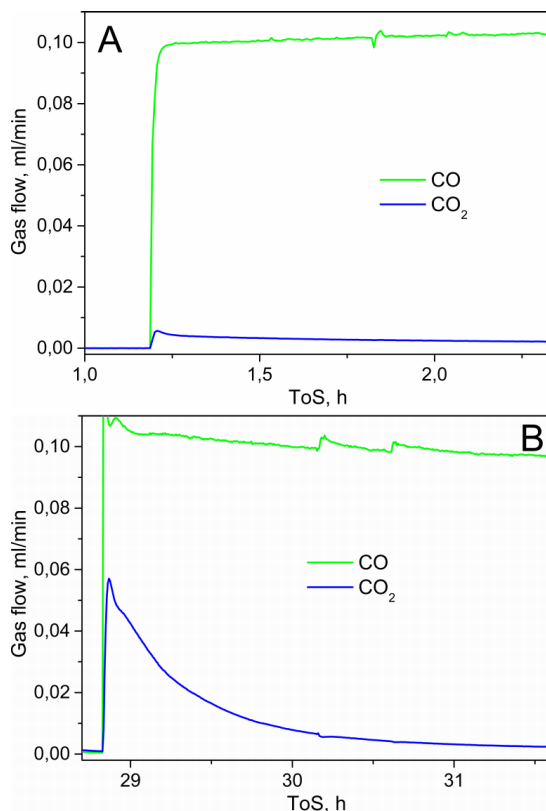


Figure 3.29. QMS data (CO:O₂=1:75) of HOPG A) before and B) after O₃ treatment at 0.3 mbar and RT.

3.2.4 Au/Au foil

To further corroborate the idea that the reactivity is due to a stoichiometric reaction between CO and O functional groups on the carbon surface, we investigated Au nanoparticles supported on oxygen-free Au foil. The Au foil was chosen as a support because it is expected to be inactive in CO oxidation.

After preparation, the surface composition of the Au/Au foil is very important. All fitting parameters are given in Tables 3.3 and 3.4. The corresponding Au 4f spectrum (Figure 3.30A(i)) of Au/Au foil shows the metallic peak at a BE of 83.95 eV with second component shifted to the low BE by 0.3 eV. This peak is assigned to the surface core-level shift [74,75], which is ascribed mainly to the lower coordination of surface atoms compared to bulk atoms. The O 1s spectrum (Figure 3.30B(i)) displays one broad peak at BE of 532.5 eV, which is in the range observed for carbonates and oxygen-containing (hydro)carbons on gold [107]. The presence of

carbonates and/or oxygen-containing (hydro)carbons on the surface is confirmed by the C 1s spectrum (Figure 3.30C(i)).

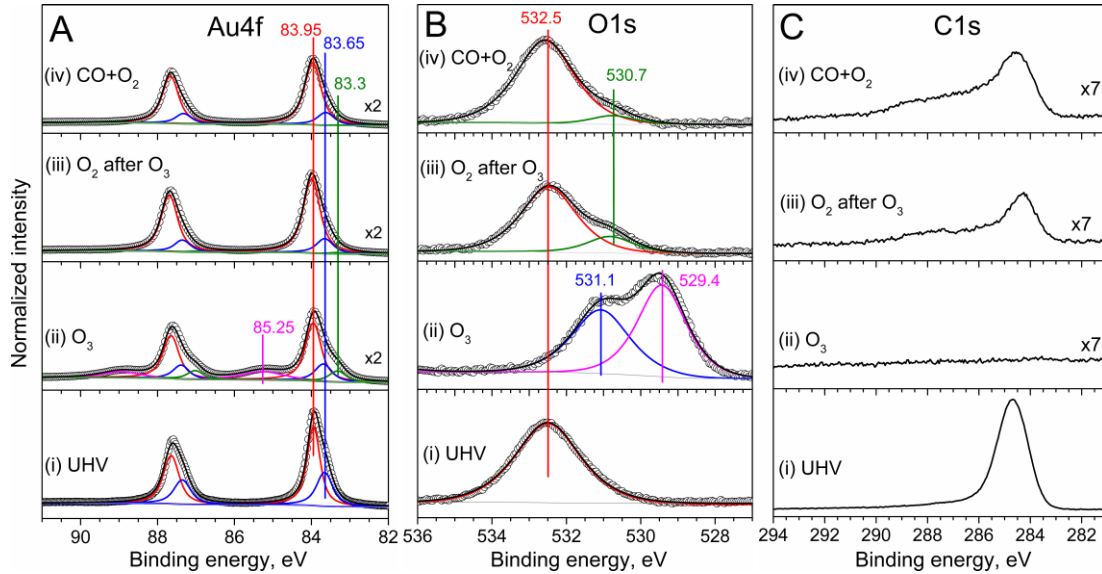


Figure 3.30. NAP (a) Au 4f, (b) O 1s and (c) C 1s XP spectra of Au/Au foil (i) in UHV at RT, (ii) under O₃ at 0.3 mbar, 150 °C, (iii) under O₂ after O₃ treatment at 0.3 mbar, RT and (iv) under CO and O₂ atmosphere (CO:O₂=1:75) at 0.3 mbar, RT.

Table 3.3. Fitting parameters of Au 4f_{7/2} spectra of Au/Au foil.

Au 4f _{7/2}								
	bulk		surface		restructuring		oxide	
	BE	FWHM	BE	FWHM	BE	FWHM	BE	FWHM
	(eV)	(eV)	(eV)	(eV)	(eV)	(eV)	(eV)	(eV)
UHV	83.95	0.49	83.66	0.50	-	-	-	-
O ₃	83.95	0.49	83.69	0.52	83.32	0.52	85.25	1.30
O ₂ after O ₃	83.98	0.51	83.65	0.52	83.34	0.52	-	-
CO+O ₂	83.96	0.51	83.65	0.52	83.32	0.52	-	-

To clean the Au surface from the surface carbon impurities, an O₃ treatment at 150 °C was performed. When we apply the combination of high temperature (150 °C) and very reactive treatment (O₃) the carbon is burned of very rapidly, as is clearly visible in the Figure 3.309C(ii). The influence of the O₃ to the sample is not limited only to the burning of the carbon, but also the oxidation of the Au surface takes place. The corresponding Au 4f spectrum (Figure 3.30A(ii)) reveals the

formation of Au oxide, the broad peak at BE of 85.25 eV appears under O₃ conditions, which is assigned to an ionic Au species [73,76]. Simultaneously, a new feature in comparison with the untreated sample appears in low BE region (BE=83.3 eV), which is assigned to the surface restructuring during oxidation [77,105]. The O 1s spectrum (Figure 3.30B(ii)) has also undergone changes: the broad peak at 532.5 eV vanishes due to carbon removal and a double peak in the lower BE region is formed. The component with BE of 529.4 eV can be assigned to a surface oxide or chemisorbed oxygen on Au [85,88,108]; the other component (BE=531.1 eV) has to be attributed to O in water and/or hydroxyl groups [73,85], but also the oxidation of contaminants in concentrations below the detection limits of XPS cannot be excluded [85].

Table 3.4. Fitting parameters of O 1s spectra of Au/Au foil.

O 1s						
	(hydro)carbon		surface oxide		Hydroxyl group/comntaminants	
	BE (eV)	FWHM (eV)	BE (eV)	FWHM (eV)	BE (eV)	FWHM (eV)
UHV	532.50	2.06	-	-	-	-
O ₃	-	-	529.42	1.55	531.07	1.82
O ₂ after O ₃	532.37	1.75	-	-	530.72	1.49
CO+O ₂	532.38	1.73	-	-	530.66	1.53

After O₃ cleaning the sample was cooled down to RT and O₃ was substituted by O₂. The cooling leads to immediate carbon accumulation as shown in the C 1s spectrum (Figure 3.30C(iii)), because usual backpressure in the reaction chamber is in 10⁻⁸ mbar range instead of 10⁻¹⁰-10⁻¹² mbar in UHV chambers. The high BE tail of the C 1s spectrum indicates the formation of C-O and C=O bonds on the surface during cooling in O₃ and further treatment in O₂. The O 1s spectrum in O₂ (Figure 3.30B(iii)) confirms the formation of oxygen-containing (hydro)carbons on the Au surface, corresponding peak at 532.5 eV is well pronounced. But additionally, a small peak at 530.7 eV is arises, and can be assigned to residual oxidized contaminants or to (hydro)carbons adsorbed on the low-coordinated atoms (defects) on the surface. There is no peak (BE <530 eV) related to the Au oxide(s). Also no

signs of Au oxide(s) (BE 85.25 eV) are in the Au 4f spectrum (Figure 3.30A(iii)), but deconvolution of the spectrum shows that the peak assigned to the surface reconstruction (BE 83.3 eV) remains. Therefore, O₃ evacuation leads to decomposition of oxide(s) and carbon accumulation.

Following O₃ treatment, we introduced a reaction mixture (CO/O₂=1:75) into the chamber. The spectra do not change substantially. Further carbon accumulation occurs, as is seen by the increase in intensity of the C 1s peak (Figure 3.30C(iv)). The shapes of the O 1s (Figure 3.30B(iv)) and Au 4f (Figure 3.30A(iv)) spectra are similar in general to the ones measured in O₂ atmosphere; only the intensity of the peak (BE=530.7 eV) corresponding to residual oxidized contaminants or to (hydro)carbons adsorbed on the low-coordinated atoms (defects) decreases.

Table 3.5. Surface composition of Au/Au foil at different conditions.

	Au ⁰ , %	Au ³⁺ , %	O, %	C, %
UHV	24.8	-	6.2	69.0
O ₃	47.7	8.9	41.8	<1.5
O ₂	37.3	-	23.4	39.3
CO+O ₂	8	-	10.3	81.7

Quantification of the surface composition of Au/Au foil is presented in Table 3.5. The untreated sample is mostly covered by carbon (69.0 %). Nevertheless initial considerable carbon coverage O₃ treatment cleans surface from carbon totally. Contemporaneously to carbon burning Au oxidation takes place during O₃ treatment, oxygen concentration on the surface in O₃ atmosphere exceeds stoichiometric ratio of Au₂O₃, which indicates the presence of an additional adsorbed oxygen overlayer. Changing chemical potential from O₃ to O₂ leads the decomposition of the surface oxide and immediate carbon accumulation (39.3 %). Following CO oxidation only facilitates further increasing carbon concentration on the surface of Au/Au foil.

Microscopy does not reveal big differences between fresh and oxidized samples. SEM images of untreated Au/Au foils show a particle size of ca. 10 nm (Figure 3.31A). In turn, the Au particle size distribution on O₃-treated samples shows some sintering effects and a slightly rougher surface (Figure 3.31B).

A fresh electrochemically prepared sample Au/Au foil was tested under reaction conditions (Figure 3.32A) at 0.3 mbar. The presence of the sample in the set-up does not influence the CO conversion. The CO₂ yield is negligible for the overall measurements. The adsorption of (hydro)carbons (see above XPS part), which cover the surface, prevent access of the gas mixture to the catalyst surface.

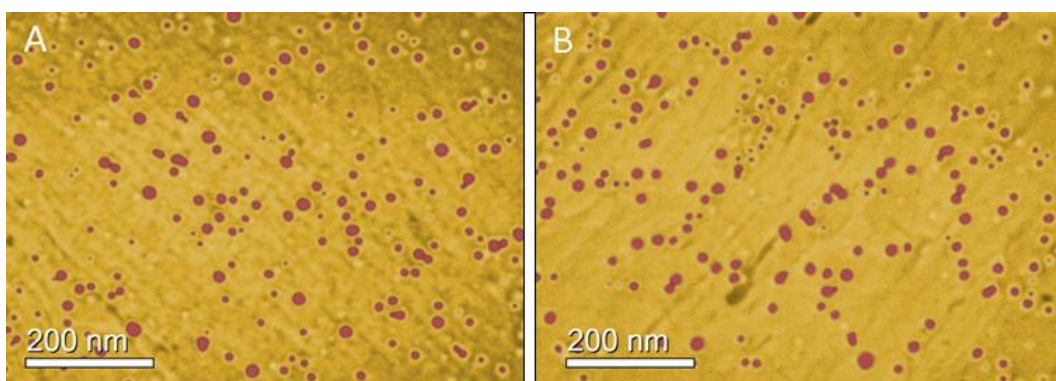


Figure 3.31. SEM images of Au/Au foil a) before and b) after O₃ treatment at 0.3 mbar. Images were colorized in order to highlight the differences between the two samples.

However, the oxidized Au sample looks more promising, but is not stable for long times (Figure 3.32B). CO consumption and deactivation time (2 hours) are similar to those observed on Au/HOPG. The corresponding Au 4f, O 1s and C 1s spectra are shown in Figure 3.33. In the Au 4f spectrum the peak assigned to surface reconstruction (BE 83.3 eV) is almost vanished (green line in Figure 3.33A). The two components of the O 1s spectra (Figure 3.33B) show opposite behavior: the oxygen-containing (hydro)carbons (BE=532.5 eV) peak increases, while the intensity of the peak (BE=530.7 eV) corresponding to residual oxidized contaminants or to (hydro)carbons adsorbed on the low-coordinated atoms (defects) decreases during the reaction. The explanation of such behavior can be that the reaction occurs between oxidized (hydro)carbons (O₃ functionalized carbon) and CO molecules. When the oxygen supply is depleted the reaction stops, and poisoning due to carbon accumulation takes place, which is evident from increasing of C 1s peak (Figure 3.33C). Thus, oxidized Au/Au foil itself does not catalyze CO oxidation at low temperature.

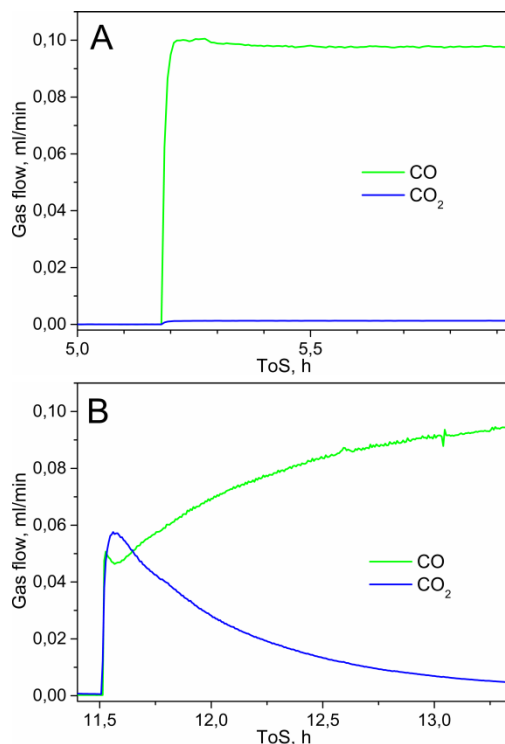


Figure 3.32. QMS data (CO:O₂=1:2) of Au/Au foil a) before and b) after O₃ treatment at 0.3 mbar and RT.

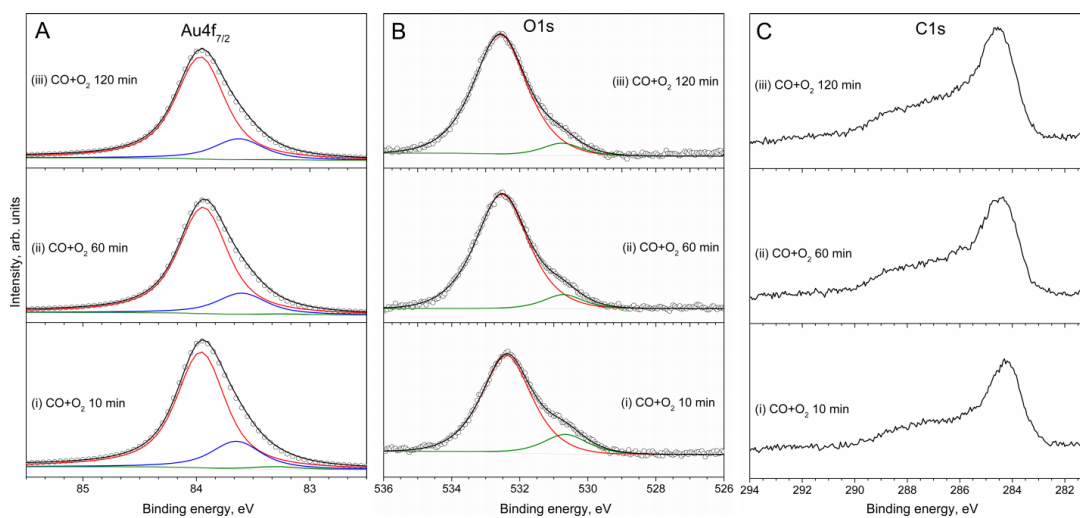


Figure 3.33. NAP (a) Au 4f_{7/2}, (b) O 1s and (c) C 1s XP spectra of Au/Au foil under CO reaction (CO:O₂=1:2) after O₃ treatment at 0.3 mbar, RT (i) after 10 min, (ii) 60 min and (iii) 120 min.

3.2.5 Conclusions.

The results presented here indicate that Au NPs supported on oxygen-free substrates are not active catalysts in CO oxidation, unless an external source of oxygen is provided. This behavior is found to be independent of the method of preparation and the nature of the support. Freshly prepared samples are covered by a carbon overlayer, which probably prevents access of the gas mixture to the active sites of the catalyst. O₃ treatment allows cleaning of the surface, but at the same time to functionalize the (hydro)carbon overlayer. Oxygen-functionalized (hydro)carbons may still be present if their removal by O₃ treatment was not completed, and can react with CO. The stoichiometric reaction ends rather soon after reaction initiation, and O₂ alone cannot re-functionalize the (hydro)carbons.

Under a constant chemical potential of O₃, an Au oxide is formed, but evacuation or substitution of O₃ by O₂ results in the disappearance of the surface oxide. Therefore, participation of Au oxide in CO oxidation can be excluded. Remaining low-coordinated atoms do not have sufficient catalytic properties, and CO oxidation does not occur on the Au NPs even after oxidation. Our results clearly show that the size reduction and/or the oxidation of Au is not an effective strategy to activate Au.

3.3. Au nanoparticles on oxide support.

3.3.1 Au/Fe₂O₃-PC (photo-induced decomposition of an Au-azido-complex to generate zero-valence Au-species)

In a large 3-necked flask, equipped with a magnetic stirrer and a centered junction of the appropriate size to house the radiation source, 1 g of solid Fe₂O₃ (Hematite, SIGMA-ALDRICH, p.a.) was suspended in a solution of 66 mg NaN₃ (SIGMA-ALDRICH) in 2 L of deionized water (MILLIPORE). The radiation source, a HERAEUS UV-TQ-150 mercury lamp, a water-cooled quartz device, was submerged into the liquid phase. From a stock, 10 mL of a solution of HAuCl₄ were added to the suspension in order to have a total of 10 mg of gold and a 20-fold molar excess of azide relative to the gold.

The decomposition of the intermediate auro-azido species and deposition of the zero-valence Au onto the dispersed support particles was stimulated by UV irradiation over 2 h. The suspension was continuously stirred and kept at room temperature.

The solid was separated from the liquid phase by suction-filtration and washed with deionized water. Finally, the sample was dried in a vacuum desiccator over KOH. The absence of color in the filtrate was indicative for near-quantitative capture of the gold by the support. The final Au load was 1wt%.

In order to have a benchmark for comparison, the first step in this study was to characterize the morphology of freshly prepared catalysts. A TEM image of an untreated Au/Fe₂O₃-PC is presented in the Figure 3.34A. The image shows a round Au NP of about 25 nm in diameter. The contact angle between the Au NP and the support (Fe₂O₃) is high, and no spreading of the support material over the Au NP surface. After annealing in O₂ and CO oxidation, Au NPs do not change significantly, retaining the same mean particle size as before oxidation (Figure 3.34B). The low degree of wetting between gold and the oxide support is also retained, with a contact angle of ca. 130°, which allows one to conclude that the interaction between Au NPs and Fe₂O₃ is not significantly altered during annealing and CO oxidation.

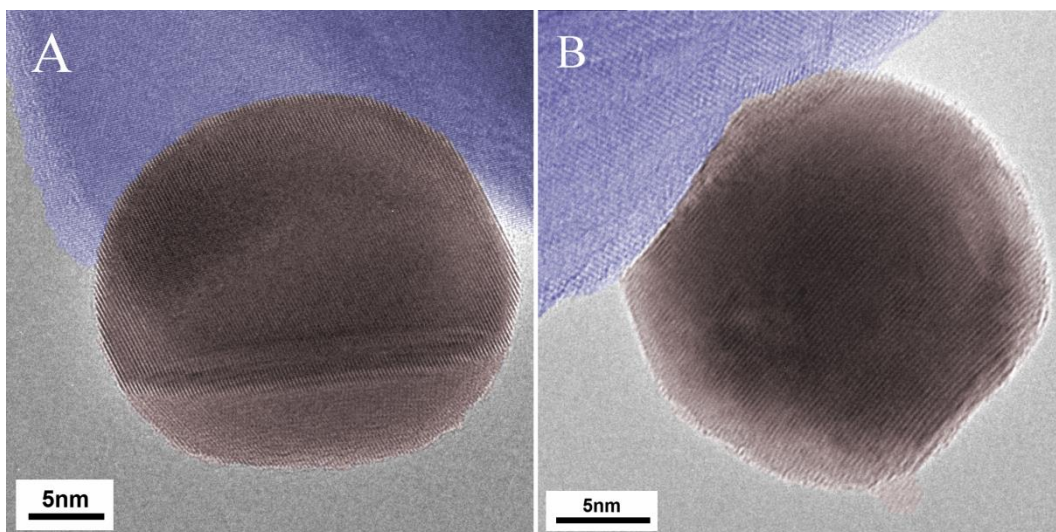


Figure 3.34. TEM images of Au/Fe₂O₃-PC (A) before and (B) after annealing in O₂ at 300 °C and CO oxidation (CO:O₂=1:2) at 0.3 mbar and 300 °C. Images were colorized in order to highlight the differences between the two samples.

NAP-XPS provides information about the electronic structure of Au under reaction conditions. Due to carbon contamination on the fresh sample, Au/Fe₂O₃-PC was annealed in O₂ to 300°C to remove the majority of the carbon. No significant changes in particle size distribution were found after annealing. Photoelectrons with 160 eV kinetic energy were used to collect the O 1s and C 1s spectra (Figure 3.35B and 3.34C). The spectra collected during annealing in O₂ are presented in Figure 3.35(i). At the beginning of the annealing process, the C 1s spectrum (Figure 3.35C(i)) shows one intense broad peak at a binding energy (BE) of 284.5 eV, which decreases with temperature. The corresponding O 1s spectrum (Figure 3.35B(i)) consists of three components (Table 3.6). The lowest binding energy species (BE 529.9eV) is associated with lattice oxygen of ferric oxide (Fe₂O₃) [109], higher binding energy species are assigned to the copper oxides/hydroxides (BE 531.6 eV) from the copper mesh [110,111] and oxygen-containing (hydro)carbons (BE 533.7 eV) [107].

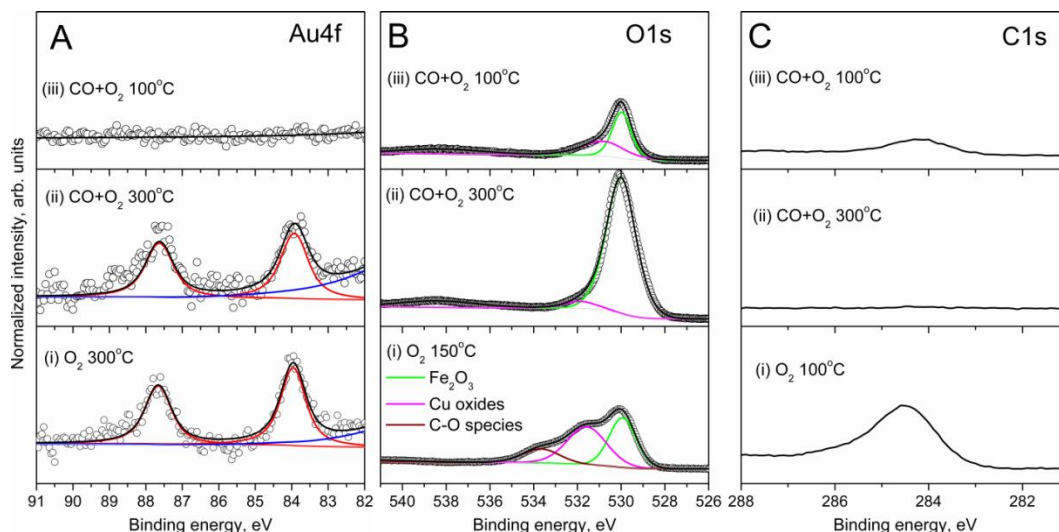


Figure 3.35. (A) Au 4f, (B) O 1s and (C) C 1s XPS spectra of Au/Fe₂O₃-PC at 0.3 mbar (i) in O₂ during annealing, (ii) in CO+O₂ (CO:O₂=1:2) at 300 °C and (iii) in CO+O₂ (CO:O₂=1:2) at 100 °C. Photoelectrons with 160 eV kinetic energy were used to collect the O 1s and C 1s spectra, and photoelectrons with 900 eV kinetic energy were used to collect the Au 4f spectra.

Table 3.6. Fitting parameters of Au 4f_{7/2} and O 1s spectra of Au/Fe₂O₃-PC.

	Au 4f _{7/2}		O 1s					
	Au ⁰		(hydro)carbon		Copper oxides/hydroxides		Fe ₂ O ₃	
	BE (eV)	FWHM (eV)	BE (eV)	FWHM (eV)	BE (eV)	FWHM (eV)	BE (eV)	FWHM (eV)
O ₂	83.97	0.83	533.7	2.0	531.6	2.1	529.9	1.5
CO+O ₂ 300 °C	83.97	0.89	-	-	531.8	1.7	530.0	1.6
CO+O ₂ 100 °C	-	-	-	-	531.6	1.6	530	1.2

In order to penetrate through the carbonaceous layer, photoelectrons with higher kinetic energy (900 eV) were used for measuring the Au 4f spectra (Figure 3.35A). The Au 4f spectrum of Au/Fe₂O₃-PC in O₂ at 300 °C (Figure 3.35A(i)) shows only one sharp peak at a BE of 83.97 eV, assigned to bulk Au in its metal

state, in accordance with the accepted Au 4f_{7/2} binding energy value [71-73]. Note that the contribution from the neighboring Cu 3p_{1/2} peak (blue line in Figure 3.35A) (BE 77.6 eV) [112] has to be taken into account for correct fitting.

After annealing, O₂ was substituted by a reaction gas mixture of CO and O₂ in a 1-to-2 ratio, keeping the temperature of Au/Fe₂O₃-PC at 300 °C. After annealing in O₂ at high temperature, the Au 4f spectrum measured in the reaction gas mixture (Figure 3.35A(ii)) does not exhibit any changes in comparison with its state during annealing in O₂. The C 1s peak totally vanishes (Figure 3.35C(ii)). The absence of the 533.7 eV peak in the O 1s spectrum (Figure 3.35B(ii)) confirms the carbon removal. The two remaining O 1s peaks are assigned to lattice oxygen in Fe₂O₃ (BE 530.0 eV) and copper oxides/hydroxides (BE 531.8 eV). Note, the increase of the intensity of Fe₂O₃ component in the O 1s spectrum (Figure 3.35B(ii)) is a consequence of removing the carbon surface layer; however, the decrease of copper oxide contribution is a result of the presence of CO, which is capable of reducing copper oxides/hydroxides to copper metal. Fe₂O₃ is more stable at low temperature than copper oxides/hydroxides, and cannot be reduced to metal at these temperatures.

Then the sample was cooled down to 100 °C in the reaction gas mixture. Cooling leads to immediate carbon accumulation on the sample surface, as shown in the C 1s spectrum (Figure 3.35C(iii)). The shape of the corresponding O 1s spectrum (Figure 3.35B(iii)) does not change. There is only an intensity decrease, as a consequence of the formation of the overlying carbon layer. As the Au loading is low, the Au 4f signal is quite weak, and consequently, after the accumulation of the carbonaceous layer at low temperature, the Au 4f signal attenuates so much that it can no longer be detected (Figure 3.35A(iii)).

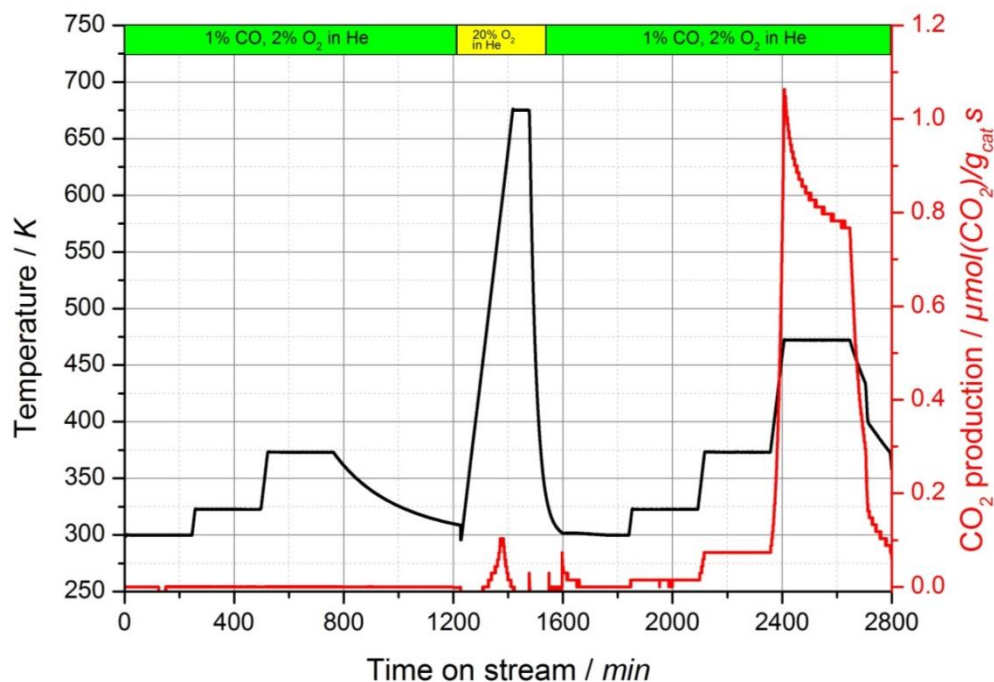


Figure 3.36. CO₂ production of Au/Fe₂O₃-PC in CO-reactor at 1 bar and CO:O₂=1:2.

Catalytic activity of Au/Fe₂O₃-PC at 0.3 mbar was below the detection limit of the mass-spectrometer, so as-prepared Au/Fe₂O₃-PC was tested in CO oxidation at atmospheric pressure in an oxygen-rich feed (CO:O₂ = 1:2) (Figure 3.36). Catalytic activity was monitored at RT, 323 and 373 K but the sample did not produce any CO₂. Subsequent oxidation of the catalyst in synthetic air was performed at 673 K for 1 hour, showing the formation of some CO₂ below 600 K, probably originating from burning of (hydro)carbons from the surface, which may block active sites. However, after the oxidative treatment, the sample became active towards CO oxidation, with CO₂ production already detectible at 323 K. The activity increased with temperature, showing no sign of deactivation when held at 323 and 373 K. However, when held at 473 K the production of CO₂ decreased by ca. 28 % over a period of 4 h. The highest amount of CO₂ observed at 473 K corresponds to a conversion of CO of about 7%.

3.3.2 Au/Fe₂O₃-C (co-precipitation) and Au/TiO₂-DP (deposition-precipitation).

200 mL of 0.1 M Fe(NO₃)₃ aqueous solution and 10 mL 0.05 M HAuCl₄ aqueous solution were mixed and stirred constantly, then the mixture was precipitated at 80 °C using 0.25 M Na₂CO₃ solution until a pH of 8.2 was reached. The gel-like precipitate was cooled, filtered and washed with hot deionized water (1 L, 80 °C) three times and dried at 120 °C for 16 hours in a muffle furnace under static air and a ramp rate of 15 °C. The final Au load was 5 wt%.

100 mL of HAuCl₄ (8.4×10^{-3} M) aqueous solution was heated to 80 °C. Then the pH value of the solution was adjusted to 8 by dropwise addition of NaOH (1 M). 4 g of TiO₂ (P25) was dispersed in the solution and the pH value was re-adjusted to 8. The suspension was then vigorously stirred at 80 °C for 2 h. Solids were collected by centrifugation (10 000 rpm, 10 min) and washed in 100 mL deionized water under stirring for 10 min at 50 °C. The above procedure was repeated three times. The solids were dried in air at 80 °C for 24 h and then calcined under a flow of synthetic air (O₂:N₂=20:80, 100 mL min⁻¹) with a heating ramp of 2 °C min⁻¹ and held at 300 °C for 4 hours. The final Au load was 1 wt%.

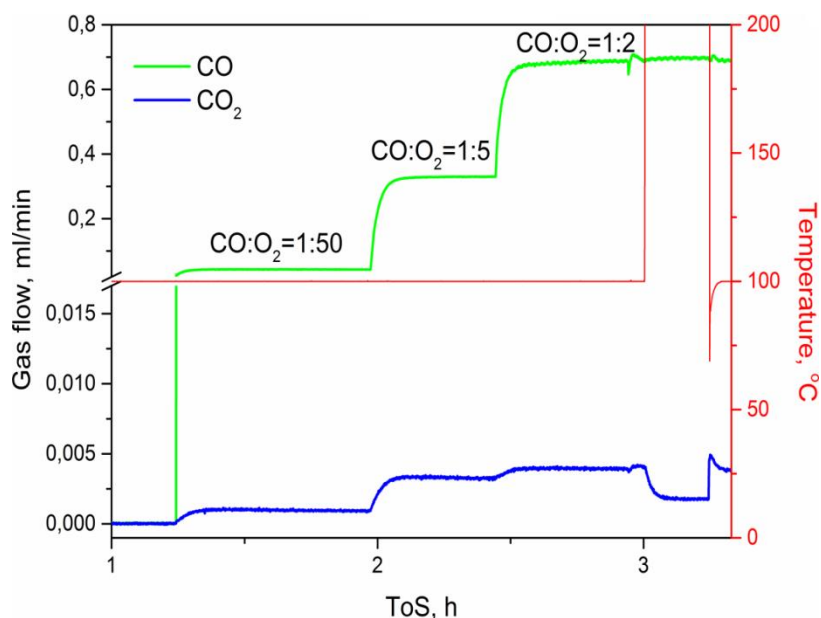


Figure 3.37. CO₂ production of Au/Fe₂O₃-C in NAP-XPS chamber at 0.3 mbar.

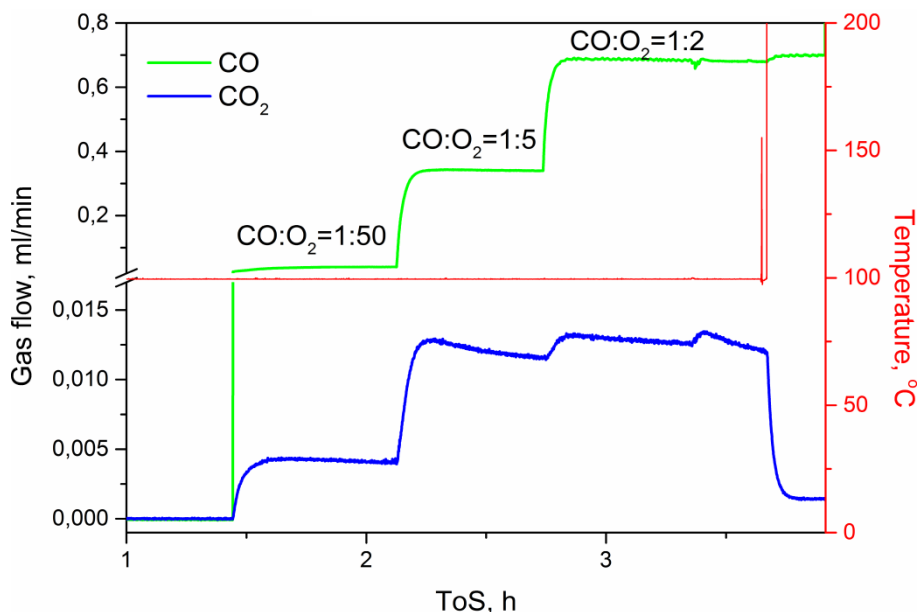


Figure 3.38. CO₂ production of Au/TiO₂-DP in NAP-XPS chamber at 0.3 mbar.

In contrast to the sample prepared by photo-induced decomposition of the Au-azido-complex, both of the samples synthesized by precipitation methods (Au/Fe₂O₃-C and Au/TiO₂-DP) exhibited high CO₂ yields at 100 °C, without any pretreatment necessary (Figure 3.37 and 3.38, respectively). As shown in Figures 3.36 and 3.37, CO₂ production increases with increasing CO:O₂ ratio. To exclude the possibility that some background reaction in the chamber was causing this reactivity, the samples were removed from the chamber without interrupting the gas flows. In Figures 3.36 and 3.37 these moments are apparent by the sharp jumps to infinity in the temperature signal (red line)—i.e. the apparent temperature becomes infinite due to breaking the contact between thermocouple and temperature control stage—occurring at a ToS of 3 hours in Figure 3.37 and at 3.7 hour in Figure 3.38. It is clear from the corresponding drop in CO₂ signal that the reaction stops immediately once the sample is removed, and restarts once the sample is returned, as seen in Figure 3.37.

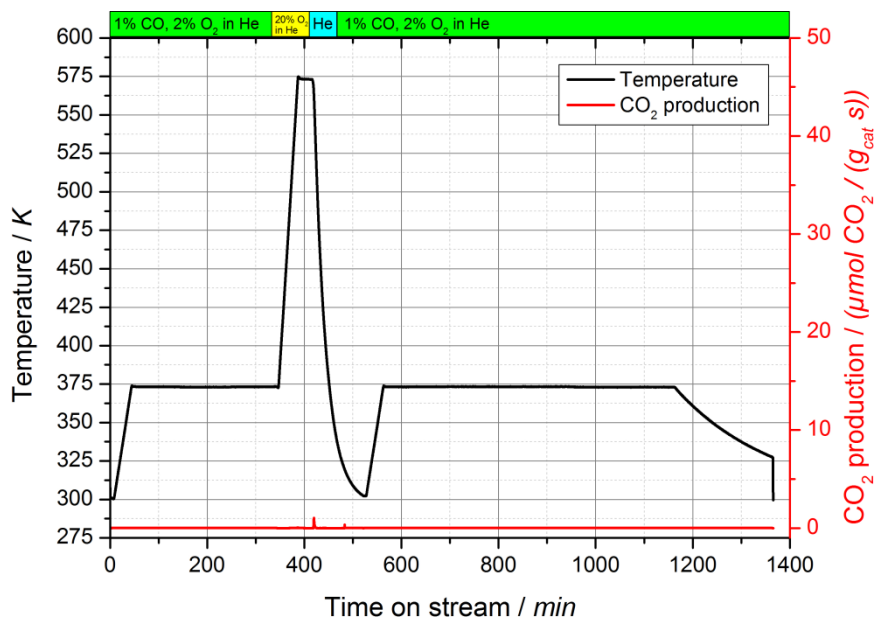


Figure 3.39. CO₂ production of pure Fe₂O₃ in CO-reactor at 1 bar (CO:O₂=1:2) and 373 K.

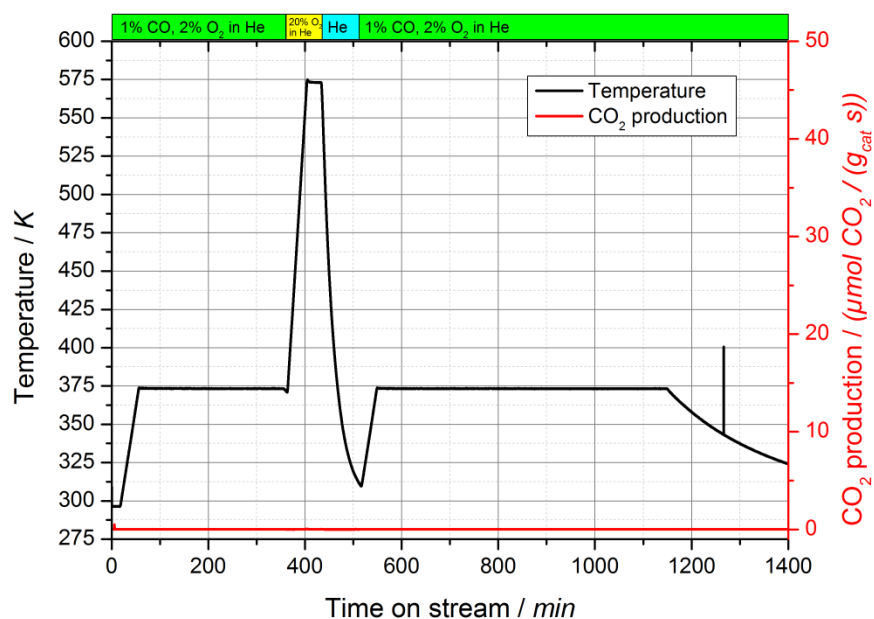


Figure 3.40. CO₂ production of pure TiO₂ in CO-reactor at 1 bar (CO:O₂=1:2) and 373 K.

Pure oxides (i.e. Fe₂O₃ and TiO₂ without Au NPs) were also tested and did not show any significant activity at low temperature (Figures 3.39 and 3.40, respectively). Thus, catalytic CO oxidation was found to occur when Au NPs are supported on transition metal oxides. The catalytic performance of Au/Fe₂O₃-C and

Au/TiO₂-DP also were tested in a CO-reactor at 1 bar (Figure 3.41 and 3.42) and confirmed the results obtained at 0.3 mbar.

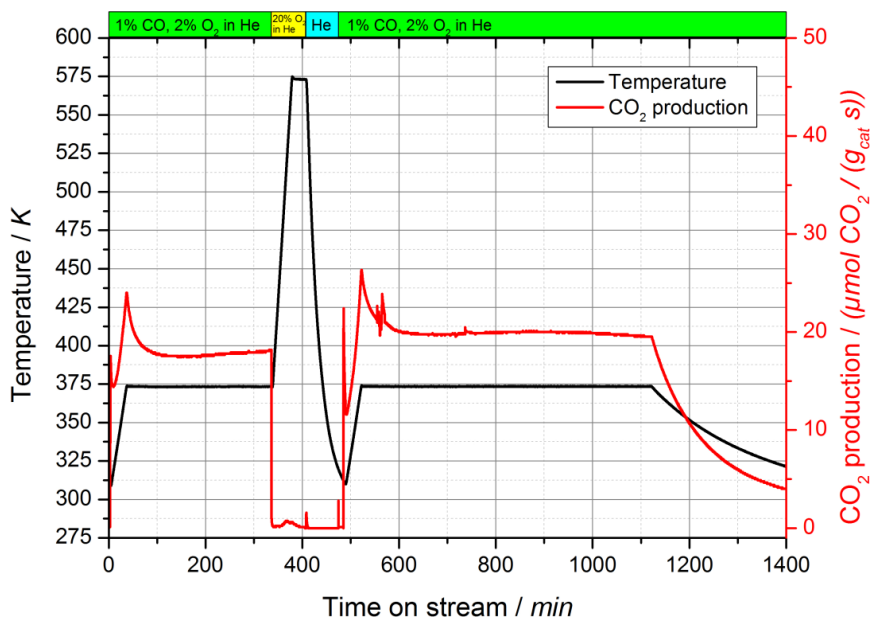


Figure 3.41. CO₂ production of Au/Fe₂O₃-C in CO-reactor at 1 bar (CO:O₂=1:2) and 373 K.

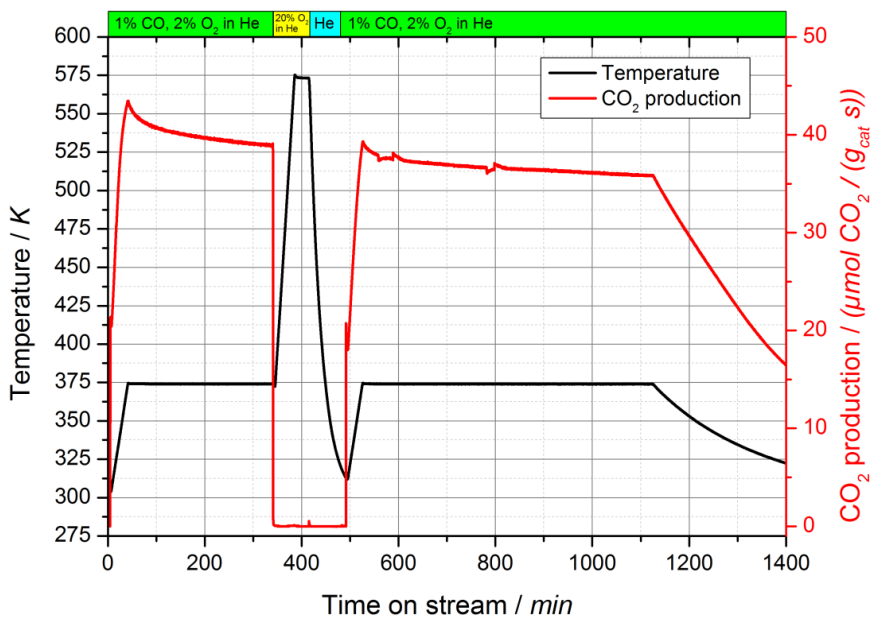


Figure 3.42. CO₂ production of Au/TiO₂-DP in CO-reactor at 1 bar (CO:O₂=1:2) and 373 K.

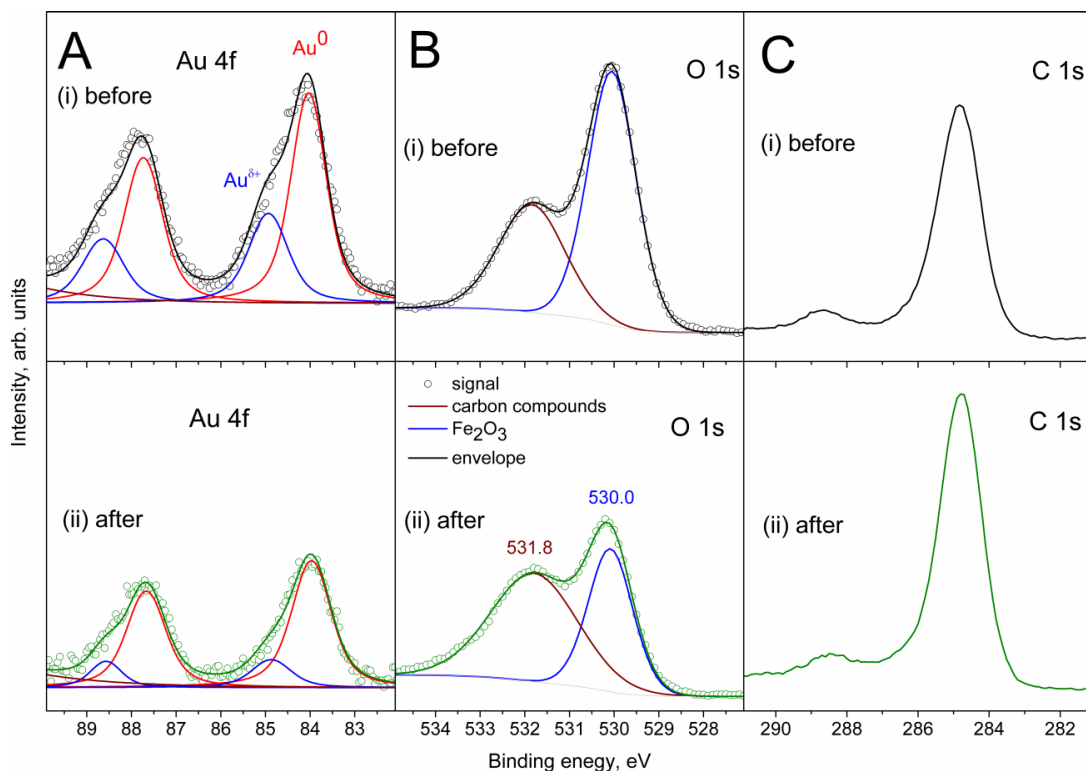


Figure 3.43. (A) Au 4f, (B) O 1s and (C) C 1s XP spectra of Au/Fe₂O₃-C before (top panel) and after (bottom panel) CO oxidation (CO:O₂=1:2) at 0.3 mbar and 100 °C. Photoelectrons with 160 eV kinetic energy were used to collect O 1s and C 1s spectra and photoelectrons with 900 eV kinetic energy were used to collect Au 4f spectra.

To further examine the nature of the Au active sites, NAP-XPS was measured of the Au/Fe₂O₃-C and Au/TiO₂-DP samples. The Au 4f core level spectrum of the fresh Au/Fe₂O₃-C, measured in UHV at 100°C before the reaction (Figure 3.43A(i)), exhibits a main metallic peak at a BE of 84.0 eV, with a second component shifted to higher BE by 0.9 eV (Table 3.7). For proper fitting of Au 4f spectra the contribution from Fe 3s peak (BE 93.7 eV) [113] has to be taken into account (wine line in Figure 3.43A). The high-binding-energy Au 4f peak is assigned to Au^{δ+}, which can be interpreted as perimeter Au atoms that interact with the metal oxide support via charge transport [26,114-117].

The corresponding O 1s spectrum (Figure 3.43B(i)) displays two peaks at BE of 530.0 eV and 531.8 eV, respectively. The first peak is assigned to lattice oxygen of Fe₂O₃ [109] and the second one to oxygen from carbonates and other oxygen-containing (hydro)carbons [107]. The presence of carbonates and/or oxygen-containing (hydro)carbons on the surface is confirmed by the very intense C 1s

spectrum, which consists of a main peak (BE=284.8 eV) and a small peak (C=O bonds) or satellite at 288.5 eV (Figure 3.43C(i)).

Table 3.7. Fitting parameters of Au 4f_{7/2} and O 1s spectra of Au/Fe₂O₃-C.

	Au 4f _{7/2}				O 1s			
	Au ⁰		Au ^{δ+}		(hydro)carbon		Fe ₂ O ₃	
	BE (eV)	FWHM (eV)	BE (eV)	FWHM (eV)	BE (eV)	FWHM (eV)	BE (eV)	FWHM (eV)
before CO	84.03	0.95	84.93	1.05	531.8	1.8	530.0	1.3
After CO	83.97	1.05	84.87	1.05	531.8	2.3	530.1	1.2

Unfortunately, during the reaction, the sample was partially charging due to the low electrical conductivity of Fe₂O₃ in the presence of an O₂-rich gas mixture at low temperature. Therefore, Au 4f, C 1s and O 1s spectra had to be measured in UHV at 100 °C after the reaction (Figure 3.43(bottom panel)) in order to obtain a reliable binding energy scale.

Table 3.8. Surface composition of Au/Fe₂O₃-C before and after CO oxidation (CO:O₂=1:2) at 100 °C.

	Au ⁰ , %	Au ^{δ+} , %	O, %	C, %	Fe, %
before	0.6	0.3	35.5	50.0	13.6
after	0.4	0.1	29.1	64.6	5.8

The C 1s peak after the reaction is more intense than before, which indicates carbon accumulation during CO oxidation. Corresponding Au 4f and O 1s spectra did not change their shapes, and only their intensities decreased due to carbon accumulation. Both, Au⁰ and Au^{δ+}, species remained even after reaction, only the ratio Au^{δ+}/Au⁰ decreases and was 0.5 and 0.25 before and after CO oxidation, respectively (Table 3.8).

The Au 4f, O 1s and C 1s XP spectra were also measured for Au/TiO₂-DP (Figure 3.44). A substantial amount of carbon is present on the surface of untreated

Au/TiO₂-DP (Figure 3.44C(ii)). In comparison with the C 1s XP spectra of Au/Fe₂O₃-C, the high-BE peak (BE 288.5 eV) is less pronounced; however, the intensities of the main peak (BE 284.9 eV) are comparable. The obtained O 1s spectrum consists of two main components (Table 3.9): the high-BE component has exactly the same position (BE 531.8 eV) as in case of Au/Fe₂O₃-C, and corresponds to oxygen-containing (hydro)carbons; the second O 1s peak differs from the Au/Fe₂O₃-C sample, having a BE at 530.5 eV. This binding energy matches well the position of lattice oxygen of TiO₂ [118]. The asymmetric Au 4f spectrum is composed of a metallic peak at a BE of 83.95 eV, and a second component shifted to the higher BE by 0.6 eV. The high-BE peak is assigned to an ionic Au species (Au^{δ+}) [119], which also suggests a strong interaction between the Au NPs and the support material.

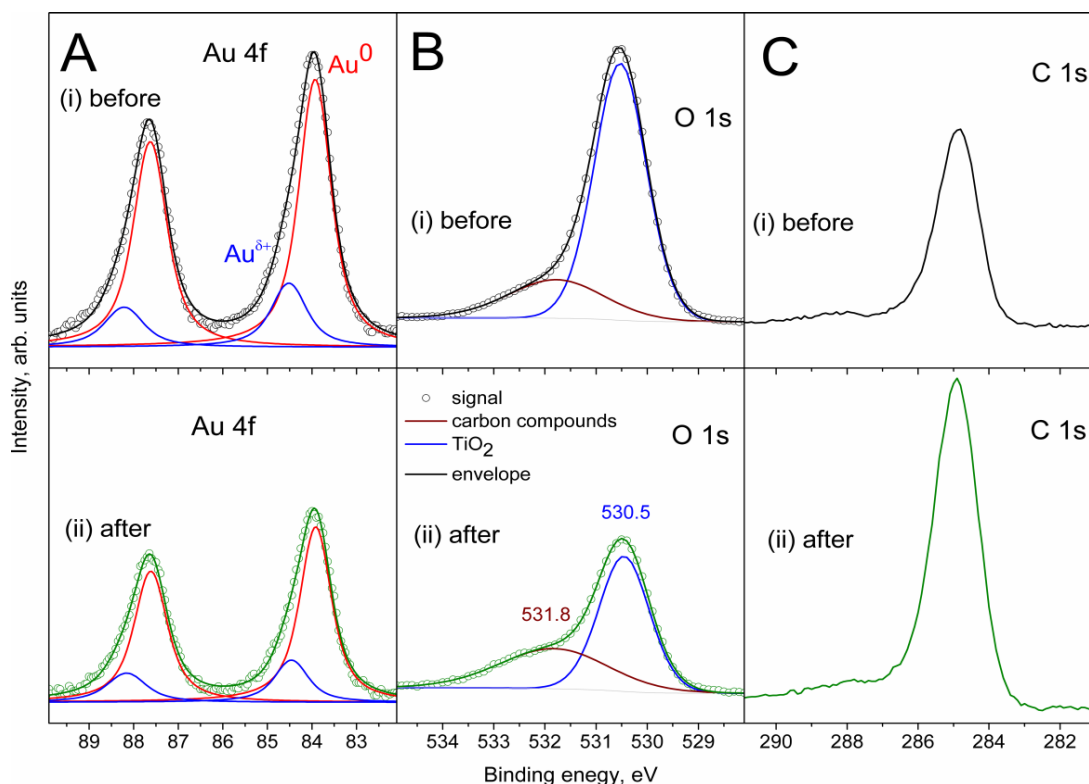


Figure 3.44. (A) Au 4f, (B) O 1s and (C) C 1s XP spectra of Au/TiO₂-DP before (top panel) and after (low panel) CO oxidation (CO:O₂=1:2) at 0.3 mbar and 100 °C. Photoelectrons with 160 eV kinetic energy were used to collect O 1s, C 1s spectra and photoelectrons with 720 eV kinetic energy were used to collect Au 4f spectra.

Table 3.9. Fitting parameters of Au 4f_{7/2} and O 1s spectra of Au/TiO₂-DP.

	Au 4f _{7/2}				O 1s			
	Au ⁰		Au ^{δ+}		(hydro)carbon		TiO ₂	
	BE (eV)	FWHM (eV)	BE (eV)	FWHM (eV)	BE (eV)	FWHM (eV)	BE (eV)	FWHM (eV)
Before CO	83.93	0.86	84.52	0.95	531.8	2.2	530.5	1.2
After CO	83.92	0.85	84.47	0.9	531.8	2.5	530.5	1.2

Table 3.10. Surface composition of Au/TiO₂-DP before and after CO oxidation (CO:O₂=1:2) at 100 °C.

	Au ⁰ , %	Au ^{δ+} , %	O, %	C, %	Ti, %
before	1.1	0.16	48.0	34.7	16.0
after	0.8	0.2	31.7	59.7	7.6

After CO oxidation on Au/TiO₂-DP, both, Au⁰ and Au^{δ+}, species remained as in case of Au/Fe₂O₃-C (Table 3.8), but their ratio Au^{δ+}/Au⁰ has changed from 0.15 before to 0.25 after reaction (Table 3.10). It cannot be explained by continuing carbon accumulation during the reaction, which leads to an increase of the C 1s peak intensity and a decrease of O 1s and Au 4f peak intensities (Figure 3.44(ii)).

The combination of XPS and TEM is a powerful approach, since it allows correlation of electronic structure and morphology. TEM images of a Au/TiO₂-DP sample are shown in Figure 3.45. In comparison with the photochemical decomposition preparation method, Au NPs synthesized by deposition precipitation, exhibit a higher degree of wetting, which indicates stronger interaction between the Au NPs and the support. More defects (for instance twins or symmetrical intergrowth of crystals, and low-coordinated atoms) are evident for the Au particles supported on titania. The NPs have a mean diameter of 15 nm.

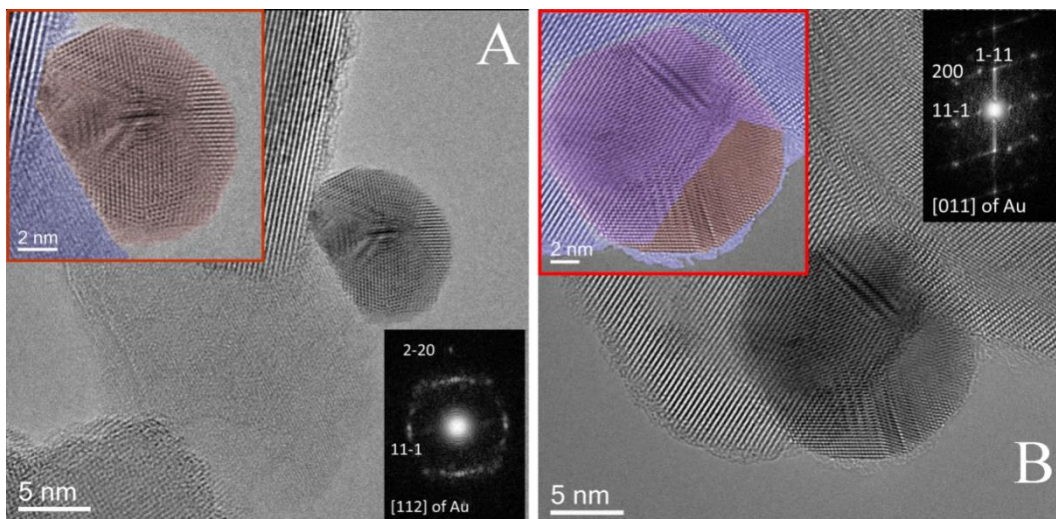


Figure 3.45. TEM images of Au/TiO₂-DP (A) before and (B) after CO oxidation (CO:O₂=1:2) at 0.3 mbar and 100°C. The insets in (A) and (B) represent power spectra of the Au nanoparticles. Images were colorized in order to highlight the differences between the two samples.

For fresh samples (i.e. prior to use in the CO oxidation reaction), no overgrowth of the support onto the NPs is visible. In contrast, after CO oxidation the Au NPs were covered by a thin layer of support material (Figure 3.45B). Similar results were obtained for Au/Fe₂O₃-C sample, with overgrowth of the support forming a thin layer over the Au NPs after the CO oxidation reaction; however, the overgrowth layer is not as extensive as in case of Au/TiO₂-DP (Figure 3.46). Therefore increasing of the Au^{δ+}/Au⁰ ratio of the Au/TiO₂-DP sample after CO oxidation detected by XPS is associated with an overlayer formation observed in TEM due to charge transfer between Au NPs and transition metal oxide. This observation confirms the assumption that a strong metal support interaction (SMSI) is occurring, which may play a key role in the activation mechanism of Au for CO oxidation.

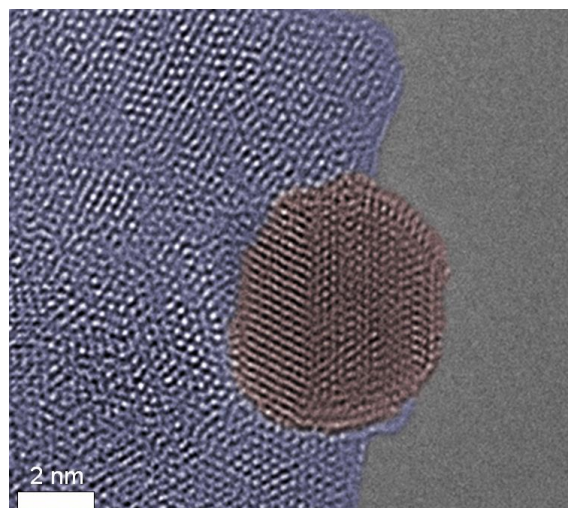


Figure 3.46. TEM image of Au/Fe₂O₃-C after CO oxidation at 0.3 mbar (CO:O₂=1:2) and 100°C. Image was colorized in order to highlight the differences between Au and Fe₂O₃.

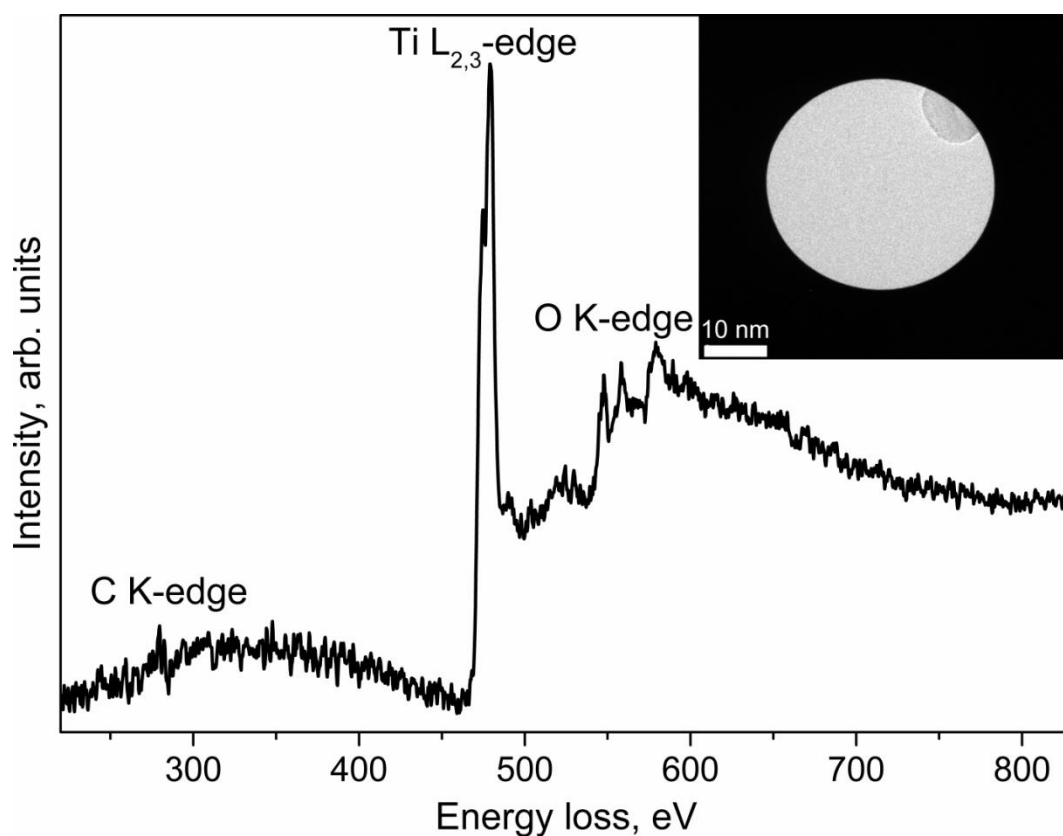


Figure 3.47. EELS spectra of Au/TiO₂-DP after CO oxidation at 0.3 mbar (CO:O₂=1:2) and 100°C. The inset represents a TEM image of a single Au NP in front of the aperture.

The spot size in our XPS measurements is $150 \times 200 \mu\text{m}$, which provides information about electronic structure averaged over this area; however, it does not allow one to judge unequivocally the origin of the overgrowth. Therefore, we use EELS to clarify the nature of overgrowth layer after reaction, and confirm whether it indeed originates from the support material. A single Au NP was placed in front of the aperture, as shown in the inset of Figure 3.47, to reduce the signal contribution from support. The obtained EELS spectrum is presented in Figure 3.47. Here one clearly sees Ti $L_{2,3}$ - and O K-edges. Therefore, the EELS measurements confirms that the overlayer arises from overgrowth of the oxide support onto the Au NPs, and that there is indeed an SMSI between Au NPs and these transition metal oxides.

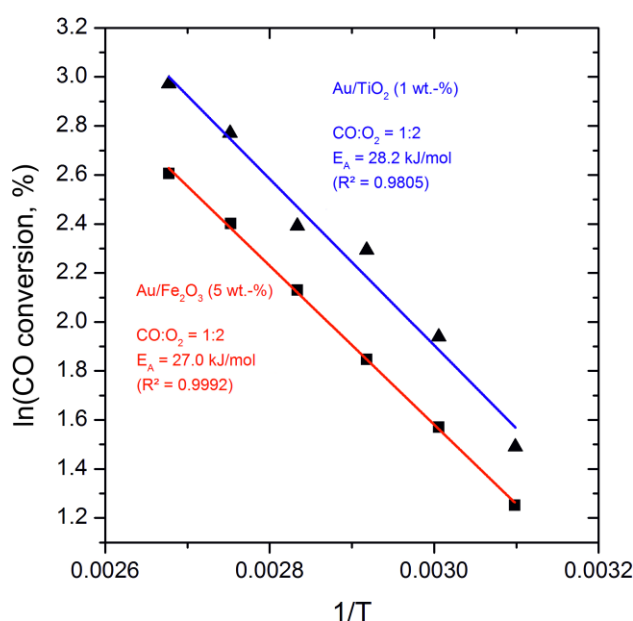


Figure 3.48. Arrhenius plot of Au/TiO₂-DP (blue line) and Au/Fe₂O₃-C (red line).

In order to estimate activation energies for CO oxidation on Au/Fe₂O₃-C and Au/TiO₂-DP, samples were placed in a CO oxidation reactor. CO conversion was measured at six different temperatures without any pre-treatment, yielding the Arrhenius plot shown in Figure 3.48. While the Au/TiO₂-DP sample shows higher conversion rates than Au/Fe₂O₃-C at all temperatures, the activation energies of both samples are similar (27.0 kJ/mol and 28.3 kJ/mol for Au/Fe₂O₃-C and Au/TiO₂-DP, respectively). Thus one may conclude that Au/TiO₂-DP had more active sites than Au/Fe₂O₃-C, but that CO oxidation on both systems may occur via similar mechanisms.

Comparison of the activities at 373 K yields about 7 $\mu\text{mol CO}_2 \text{ g}_{[\text{Au}]}^{-1} \text{ s}^{-1}$ for photo-chemically prepared Au/Fe₂O₃-PC after oxidative pre-treatment (673 K) and 20 $\mu\text{mol CO}_2 \text{ g}_{[\text{Au}]}^{-1} \text{ s}^{-1}$ Au/Fe₂O₃-C by co-precipitation without any pre-treatment. The most active sample was Au/TiO₂-DP, with a yield of 35 $\mu\text{mol CO}_2 \text{ g}_{[\text{Au}]}^{-1} \text{ s}^{-1}$. The most important results about Au-based samples on transition metal oxides are summarized in Table 3.11.

Table 3.11. Main finding of Au NPs supported on transition metal oxides.

	Au/Fe ₂ O ₃ -PC	Au/Fe ₂ O ₃ -C	Au/TiO ₂ -DP
BE difference between Au ^{δ+} and Au ⁰ , eV	-	+0.9	+0.6
degree of wetting	low	high	high
overlayer formation	no	low	high
activation energy for CO oxidation, kJ/mol	-	27.0	28.3
CO ₂ yield, $\mu\text{mol CO}_2 \text{ g}_{[\text{Au}]}^{-1} \text{ s}^{-1}$	<7	20	35

Our experiments reveal that activity of Au on transition metal oxides, such as Fe₂O₃ and TiO₂, depends on the method of synthesis. Only samples prepared by the precipitation method showed high CO₂ production at low temperature, independent of the metal oxide. It is known that the method of synthesis is crucial for controlling the activity of a catalyst [120]. Au NPs synthesized by photo-induced decomposition do not possess any significant catalytic activity because of minimal interaction with the metal oxide support, and therefore such samples retain the inertness of bulk gold. Most preparation methods produce large NPs that are inactive for CO oxidation, but deposition precipitation provides good control over particle size. The preparation of Au/TiO₂ by deposition precipitation has been studied in detail by Moreau et al. [121] and they outline that the method allows one to control many experimental parameters (concentration, temperature, pH, time, etc.).

As is apparent from the XPS results, two Au species are formed on the active catalysts. TEM images of these samples reveal the formation of an extended interface

between the Au NPs and the oxide support. Therefore, it is possible that the Au^{δ+} component seen in the XP spectra is from a species formed by a strong interaction between the surface Au atoms and overgrowth layer from the oxide supports. In the literature there is much debate concerning the nature of the active site for Au-based catalysts. Various factors—such as quantum size effects [122], low coordinated atoms, surface ions and the support interactions [25]—have been proposed as factors that influence Au activity. Some authors consider metallic gold [123,124] to be the active site, while others suggest positive (δ+) [125,126] or negative (δ-) [127,128] low-charged gold or oxidized (1+,3+) states [129]. Some years ago Bond and Thomson [26] proposed a model where Au atoms at the interface between Au and the oxide are the active oxidation centers; however, they focus on a mechanistic debate, while the electronic structure of active Au remained unclear.

Our present findings suggest that, on the active catalyst's surface, gold is present in both cationic and metallic forms, where the atoms at the triple-phase boundary are cationic in nature. These results are in a good agreement with previous works of Costello et al. [130] and Kung et al. [116], where a chemical model that involves an ensemble of metallic Au atoms and Au cations with hydroxyl ligands has been suggested.

It must also be noted that XP spectra of Au NPs are markedly affected by final-state effects, and furthermore, the binding energy of the Au⁰ is highly size-dependent for small nanoparticles [131]. When the electron leaves the system, a core hole is made and is stabilized to a varying degree depending on the chemical environment. If this core hole decay occurs before the emitted photoelectron is completely decoupled from the system, then the electron binding energy is affected. The ionization of a single atom will result in a localized hole with little ability for the atom to electronically relax, while in a cluster of many atoms, the hole produced after ionization may be delocalized over the cluster lowering the final state energy. It was shown that Au NPs containing less than 70 atoms (0.5 nm) have a BE shift of the Au 4f peak by 0.25 eV to higher region independently on the substrates [132]. However, BE value decreases with increasing number of atoms and approaches value of bulk Au, when NPs reach size about 5 nm (1800 atoms). In our case, because of rather large Au NPs (15 nm) and simultaneously observed shifted and none shifted

Au species, the contribution from final-state effects to BE shift can be excluded, so the positive binding energy shifts are the result of the interaction between Au and the oxide support. The similarity in the high-BE shift values of Au/TiO₂-DP and Au/Fe₂O₃-C suggests the same origin for both samples, i.e. SMSI. The small difference in chemical shift arises due to different interaction strengths (charge transfer) between Au and the oxides. The high-BE shift value (0.9 eV) for Au/TiO₂-DP correlates well with Chusuei's work [133]. Yang and Wu [134] showed that the high-BE shift is caused by the interaction of gold with oxygen vacancies and not by final-state effects. DFT calculations also identify the importance of Au-transition metal oxide interaction in CO oxidation [135].

The obtained TEM images reliably show that the formation of an overgrowth layer can be observed only after the reaction. Au^{δ+} peak observed in XPS before reaction shows initial interaction between Au NPs and underlying oxide. The overgrowth layer from the support is evidence of a SMSI. Furthermore, the higher CO₂ production rate of Au/TiO₂-DP than Au/Fe₂O₃-C may be explained by different interaction strengths between Au and the support. Indeed, Grunwald et al. [136] showed higher activity of Au/TiO₂ in comparison with Au/ZrO₂ even though the particle sizes were identical. They believe that the support affects the ability of Au to dissociate oxygen. Also Au-based catalysts supported on 'non-reducible' metal oxide supports (Au/Al₂O₃) have considerably less activity than those supported on 'reducible' metal oxide supports (Au/Fe₂O₃, Au/TiO₂) [137]. Au-assisted Mars-van Krevelen mechanism of reducible support [138] was discussed to be the origin of the overgrowth layer. Based on quantitative temporal analysis of products reactor measurements, which allow the detection and quantification of active species even at the extremely low concentrations at RT and above, Behm's group [139] has shown that the active oxygen species for CO oxidation on Au/TiO₂ at temperature above 80 °C is formed only at the perimeter of the Au-oxide interface. In-situ infrared spectroscopy confirms the interaction of CO molecules with the partly reduced titania support surface under reduction atmosphere [140]. Indeed, locally reduced TiO₂ near Au NPs may have higher mobility, which could lead to the formation of an overlayer.

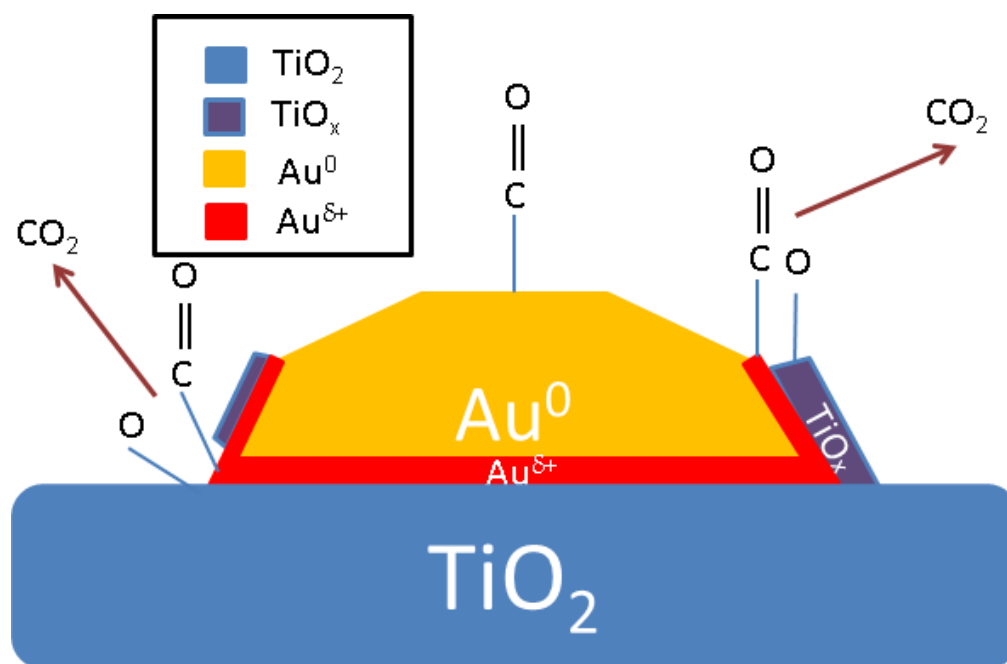
The activation energy values calculated from Arrhenius plots for CO oxidation and specific surface area measurements (S_{BET}) of our samples, Au/Fe₂O₃-C and Au/TiO₂-DP, prepared by precipitation methods are shown in Table 3.13 together with a comparison with other works. Despite the similarity of activation energy values and sizable difference in specific surface area, 27.0 kJ/mol and 28.2 kJ/mol, 206.8 m²/g and 54.8 m²/g for Au/Fe₂O₃-C and Au/TiO₂-DP, respectively, the intrinsic activity of Au/TiO₂-DP is much higher (Table 3.12), which suggests higher numbers of active sites on the surface. Because of the existence of numerous defects on the surface of active samples, SMSI also enables stabilization of low-coordinated Au atoms.

Table 3.12. Activation energies for CO oxidation and specific surface area of Au/Fe₂O₃ and Au/TiO₂ prepared by different methods.

Catalysts	Preparation method	S_{BET} [m ² /g]	E_a [kJ/mol]	Ref.
Au/Fe ₂ O ₃	DP		29	[137]
	DP		35	[141]
	DP with phosphine		21	[142,143]
	co-precipitation	206.8	27.0	This work
	co-precipitation	73		[41]
	co-precipitation	45		[144]
	DP	196.1		[145]
Au/TiO ₂	DP		27	[146,147]
	DP with phosphine		12	[142,143]
	impregnation		21	[137]
	impregnation		29	[148]
	DP	54.8	28.2	This work
	DP	44		[144]
	DP	81.8		[149]
	colloidal deposition	47		[150]

Our results agree well with the proposed reaction pathway (Scheme 3.1) for the CO oxidation reaction over supported Au catalysts, as described by Schubert et al. [137] Oxygen adsorbs in large quantities on reducible metal oxides and then migrates

to the Au NPs. Dissociation of the mobile oxygen is suggested to take place at the metal–support interface, after which atomic oxygen reacts with CO adsorbed on the gold and/or at the interface. Therefore, the formation of an overlayer increases triple phase boundary, which leads to increases in CO₂ yield. An increase in interface area can be achieved by decreasing the particle size, which also leads to a significant increase of CO₂ production [122,142,151].



Scheme 3.1. Suggested CO oxidation pathway on Au/TiO₂.

3.3.3 Conclusions.

The results presented here indicate that the Au NPs on transition metal oxides show high catalytic activity, which depends on the method of preparation, and can be associated with the formation of positively charged Au species. Indeed, only the samples prepared by precipitation methods showed significant CO conversion at low temperature. XPS revealed the presence of two Au species (Au⁰ and Au^{δ+}) on the surface of active Au/TiO₂-DP and Au/Fe₂O₃-C samples. The energy shift of the Au^{δ+} peak, relative to bulk gold (Au⁰), depends on the support, and is 0.6 eV and 0.9 eV to higher binding energy for Au/TiO₂-DP and Au/Fe₂O₃-C, respectively. TEM images indicate the formation of overlayers on Au particles. EELS spectra confirm that the

overlayers consist of support material—i.e. transition metal oxide overlayers on top of the Au NPs.

Tiny activity of Au/Fe₂O₃-PC at higher temperature shows that there are some active sites, but their amount is very little. Sample synthesized by photo-induced decomposition of an Au-Azido complex is characterized by small contact angle between Au and Fe₂O₃ and spherical shape of NPs. These features do not allow forming strong interaction between Au NPs and metal oxide. Therefore the correct strategy to activate Au is to form Au-support interaction via charge transfer, which can be realized by the method of synthesis.

4. Summary.

The discovery that gold nanoparticles (Au NPs) supported on metal oxides are active in low-temperature CO oxidation has inspired a considerable amount of research focused on understanding the basis of activity of Au catalysts. Various factors—such as quantum size effects, low coordinated atoms, surface ions and the support interaction have been proposed as factors that influence Au activity. In this thesis a systematic study of the catalytic properties of oxidized Au and Au NPs on various supports in CO oxidation reaction were conducted.

All measurements were performed in the near ambient pressure X-ray photoelectron spectroscopy (NAP-XPS) endstation at the ISIS beamline at HZB/BESSY II (Berlin, Germany). Gold containing samples (Au foil, Au NPs supported on carbon and transition metal oxides) were characterized using *in-situ* XPS and *ex-situ* techniques, such as electron energy loss spectroscopy (EELS), scanning and transmission electron microscopy (SEM and TEM). CO and O₂/O₃ were introduced to the chamber at different ratios, keeping the pressure and temperature constant, at 0.3 mbar and 100°C, respectively.

The procedure, used to prepare the Au/HOPG (highly oriented pyrolytic graphite) model catalysts, involves forming defects on the HOPG surface via soft Ar⁺ sputtering, followed by Au deposition and surface annealing at 300°C in UHV (for Au NPs stabilization). Au NPs supported on functionalized carbon nanotubes (CNTs) were prepared using immobilization and incipient impregnation methods. Nanoscopic Au was electrochemically deposited on Au foil. Au NPs on transition metal oxides were synthesized by precipitation (Au/Fe₂O₃, Au/TiO₂) and photochemical decomposition of intermediate gold-azido complexes (Au/Fe₂O₃, Au/Cr₂O₃) methods.

Our *in-situ* measurements show that the oxidation of extended Au surfaces by O₃ treatment is accompanied by the formation of meta-stable surface oxide(s). It was found that Au oxide does not directly participate in CO oxidation on Au-based catalysts. Our experiments on Au foil allow us to conclude that low-coordinated Au atoms, present on the surface after oxidation, do not possess catalytic activity for CO oxidation at room temperature. Similar to oxidized Au foil, Au NPs on oxygen-free

supports (HOPG, functionalized CNTs, Au foil) do not show any catalytic activity, regardless of the NPs' size, the type of the support and the method of synthesis. Therefore, NP size only reduction and/or oxidation are not sufficient to activate Au (Table 4.1).

Table 4.1 CO oxidation on Au-based catalysts.

	Stoichiometric reaction	Catalytic reaction
Clean Au foil	✗	✗
Oxidized Au foil	✗	✗
Clean Au powder	✗	✗
Oxidized Au powder	✗	✗
Au@HOPG	✗	✗
Oxidized Au@HOPG	✓	✗
Au@N-CNTs	✗	✗
Oxidized Au@N-CNTs	✓	✗
Au@O-CNTs	✗	✗
Oxidized Au@O-CNTs	✓	✗
Au@Au foil	✗	✗
Oxidized Au@Au foil	✓	✗
Au@Fe ₂ O ₃ (photo-induced)	-	✗ / ✓
Au@Cr ₂ O ₃ (photo-induced)	-	✗ / ✓
Au/Fe ₂ O ₃ (coprecipitation)	-	✓
Au/TiO ₂ (deposition-precipitation)	-	✓

In contrast, Au NPs on oxygen containing supports show high catalytic activity, which depends on the method of preparation, and can be associated with the formation of positively charged Au species (Figure 4.1). Indeed, only samples prepared by precipitation methods showed significant CO conversion at low temperature. XPS revealed the presence of only two Au species (Au⁰ and Au^{δ+}) on the surface of active samples, Au NPs of inactive sample have 'bulk'-like (Au⁰) nature. The energy shift of the Au^{δ+} peak, relatively to bulk gold (Au⁰), depends on

the support, and is 0.6 eV and 0.9 eV to higher binding energy for Au/TiO₂ and Au/Fe₂O₃, respectively. TEM and EELS spectra show the formation of transition metal oxide overlayers on top of the Au NPs.

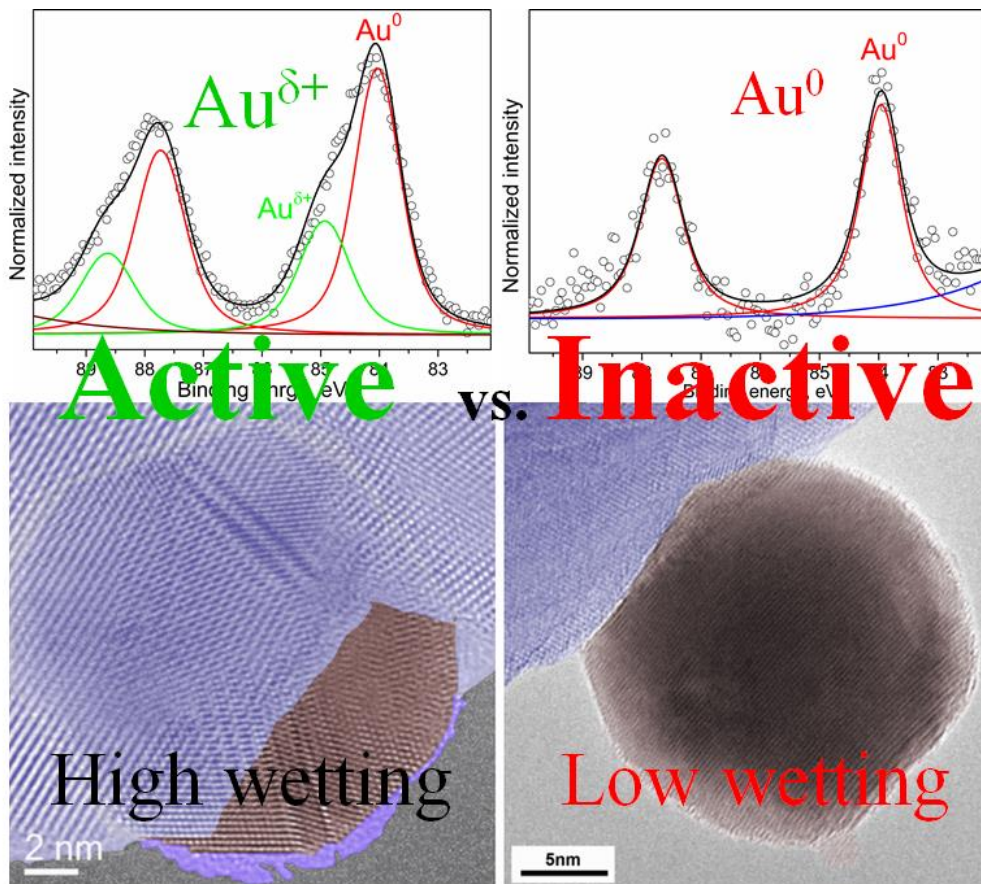


Figure 4.1. Au 4f XP spectrum and TEM image of sample synthesized by deposition-precipitation (left) and photochemical decomposition of intermediate gold-azido complex (right) method.

Our results suggest a mechanism of Au activation in CO oxidation via Strong Metal Support Interaction, assuming a strong influence of the support on the electronic structure of the gold through charge transfer and stabilization of low-coordinated Au atoms. Therefore SMSI plays key role in Au activation for CO oxidation and is more important than size reduction.

Bibliography.

1. G. C. Bond, *Heterogeneous Catalysis: Principles and Applications*, Oxford U.P, Oxford, 1987.
2. G. C. Bond, C. Louis, D. T. Thompson, *Catalysis by Gold*, Imperial College Pr., London, 2007.
3. B. Hinnemann, J. K. Nørskov, *Top. Catal.* **2006**, *37*, 55-70.
4. R. Schlögl, in *Handbook of Heterogeneous Catalysis*, ed. G. Ertl, H. Knozinger, F. Schuth, J. Weitkamp, Wiley-VCH Verlag, GmbH & Co. KGaA, Weinheim, 2008, Chapter 12.1, pp. 2501-2575.
5. F. Haber, G. van Oordt, *Z. Anorg. Allg. Chem.* **1905**, *44*, 341–378.
6. A. M. Trzeciak, J. J. Ziolkowski, *Coord. Chem. Rev.* **1999**, *190-192*, 883-900.
7. K. Klier, *Adv. Catal.* **1982**, *30*, 243-313.
8. G. P. Van der Laan, A. A. C. M. Beenackers, *Catal. Rev. –Sci. Eng.* **1999**, *41*, 255-318.
9. L. Glasser, *J. Chem. Educ.* **1979**, *56*, 22.
10. A. Couper, D. D. Eley, *Discuss. Faraday Soc.* **1950**, *8*, 172-184.
11. B. L. M. Hendriksen, J. W. M. Frenken, *Phys. Rev. Lett.* **2002**, *89*, 046101.
12. A. Hoffman, T. Maniv, M. Folman, *Surf. Sci.* **1987**, *183*, 484–502.
13. A. Atli, M. Abon, P. Beccat, J.C. Bertolini, B. Tardy, *Surf. Sci.* **1994**, *302*, 121–125.
14. H. Hirano, T. Yamada, K. I. Tanaka, J. Siera, P. Cobden, B. E. Nieuwenhuys, *Surf. Sci.* **1992**, *262*, 97–112.
15. K.S. Kim, M. A. Barteau, *Surf. Sci.* **1989**, *223*, 13–32.
16. J. H. McCreery, G. Wolken Jr., *J. Chem. Phys.* **1976**, *64*, 2845-2853.
17. R. A. Barker, P. J. Estrup, F. Jona, P. M. Marcus, *Solid State Commun.* **1978**, *25*, 375–379.
18. M. Bäumer, H.-J. Freund, *Prog. Surf. Sci.* **1999**, *61*, 127-198.
19. L. Aballe, A. Barinov, A. Locatelli, S. Heun, M. Kiskinova, *Phys. Rev. Lett.* **2004**, *93*, 196103.
20. D. W. Goodman. *Chem. Rev.* **1995**, *95*, 523-536.

21. A. Böttcher, H. Nirhus, S. Schwegmann, H. Over, G. Ertl, *J. Phys. Chem. B* **1997**, 101, 11185-11191.
22. T. C. R. Rocha, M. Hävecker, A. Knop-Gericke, R. Schlögl, *J. Catal.* **2014**, 312, 12-16.
23. P. A. Sermon, *Gold Bull.* **1976**, 9, 129-131.
24. M. Haruta, N. Yamada, T. Kobayashi, S. Iijima, *J. Catal.* **1989**, 115, 301-309.
25. B. K. Min, C. M. Friend, *Chem. Rev.* **2007**, 107, 2709-2724.
26. G.C. Bond, D. T. Thompson, *Gold Bull.* **2000**, 33, 41-51.
27. T. Hayashi, K. Tanaka, M. Haruta, *J. Catal.* **1998**, 178, 566-575.
28. A. K. Sinha, S. Seelan, S. Tsubota, M. Haruta, *Top. Catal.* **2004**, 29, 95-102.
29. I. Andreeva, T. Tabakova, A. Andreev, *J. Catal.* **1996**, 158, 354-355.
30. A. S. K. Hashmi, G. J. Hutchings, *Angew. Chem. Int. Ed.* **2006**, 45, 7896-7936.
31. C. González-Arellano, A. Corma, M. Iglesias, F. Sánchez, *Chem. Commun.* **2005**, 27, 3451-3453.
32. N. Dimitratos, J. A. Lopez-Sanchez, G. J. Hutchings, *Chem. Sci.* **2012**, 3, 20-44.
33. M. C. Kung, J.-H. Lee, A. Chu-Kung, H. H. Kung, *Stud. Surf. Sci. Catal.* **1996**, 101, 701-710.
34. A. Ueda, T. Oshima, M. Haruta, *Appl. Catal. B* **1997**, 12, 81-93.
35. R. M. T. Sanchez, A. Ueda, K. Tanaka, M. Haruta, *J. Catal.* **1997**, 168, 125-127.
36. G. K. Bethke, H. H. Kung, *Appl. Catal. A* **2000**, 194, 43-53.
37. Y. A. Kalvachev, T. Hayashi, S. Tsubota, M. Haruta, *J. Catal.* **1999**, 186, 228-233.
38. T. Hayashi, K. Tanaka, M. Haruta, *J. Catal.* **1998**, 178, 566-575.
39. J. F. Jia, K. Haraki, J. N. Kondo, K. Domen, K. Tamaru, *J. Phys. Chem. B* **2000**, 104, 11153-11156.
40. M. Okumura, T. Akita, M. Haruta, *Catal. Today* **2002**, 74, 265-269.
41. M. Haruta, M. Daté, *Appl. Catal. A* **2001**, 222, 427-437.
42. J.-L. Lu, H.-J. Gao, S. Shaikhdinov, H.-J. Freund, *Catal. Lett.* **2007**, 114, 8-16.
43. F. Boccuzzi, A. Chiorino, M. Manzoli, *Surf. Sci.* **2000**, 454-456, 942-946.

44. Y. Iizuka, T. Tode, T. Takao, K. Yatsu, T. Takeuchi, S. Tsubota, M. Haruta, *J. Catal.* **1999**, *187*, 50-58.
45. K. Mallick, M. S. Scurrall, *Appl. Catal. A Gen.* **2003**, *253*, 527-536.
46. J.-D. Grunwaldt, M. Maciejewski, O. S. Becker, P. Fabrizioli, A. Baiker, *J. Catal.* **1999**, *186*, 458-469.
47. J. T. Calla, R. J. Davis, *J. Phys. Chem. B* **2004**, *109*, 2307-2314.
48. A. K. Tripathi, V. S. Kamble, N. M. Gupta, *J. Catal.* **1999**, *187*, 332-342.
49. D. E. Starr, Sh. K. Shaikhutdinov, H.-J. Freund, *Top. Catal.* **2005**, *36*, 33-41.
50. M. Valden, S. Pak, X. Lai, D. W. Goodman, *Catal. Lett.* **1998**, *56*, 7-10.
51. G. Glaspell, L. Fuoco, M. S. El-Shall, *J. Phys. Chem. B* **2005**, *109*, 17350-17355.
52. W.-C. Li, M. Comotti, F. Schüth, *J. Catal.* **2006**, *237*, 190-196.
53. V. Schwartz, D. R. Mullins, W. Yan, B. Chen, S. Dai, S. H. Overbury, *J. Phys. Chem. B* **2004**, *108*, 15782-15790.
54. A. Bongiorno, U. Landman, *Phys. Rev. Lett.* **2005**, *95*, 106102.
55. B. K. Min, A. R. Alemozafar, D. Pinnaduwege, X. Deng, C. M. Friend, *J. Phys. Chem. B* **2006**, *110*, 19833-19838.
56. J.-D. Grunwaldt, A. Baiker, *J. Phys. Chem. B* **1999**, *103*, 1002-1012.
57. N. Lopez, J. Norskov, *J. Am. Chem. Soc.* **2002**, *124*, 11262-11263.
58. H. Robinson, W. F. Rawlison, *Phil. Mag.* **1914**, *28*, 277-281.
59. M. de Broglie, *Compt. Rend. Acad. Sci.* **1921**, *172*, 274-275.
60. C. S. Fadley, in *Electron Spectroscopy: Theory, Techniques and Applications*, ed. C.R. Brundle and A.D. Baker, Academic Press, New York, 1978, Vol.2, Chapter 1, pp. 2-157.
61. K. Siegbahn, C. Nordling, G. Johansson, J. Hedman, P.-F. Heden, K. Hamrin, U. Gelius, T. Bergmark, L. O. Werme, R. Manne, Y. Baer, *ESCA applied to free molecules*, Amsterdam, North-Holland, 1969.
62. D.A. Shirley, *Phys. Rev. B* **1972**, *5*, 4709-4714.
63. S. Tougaard, *Surf. Interface Anal.* **1997**, *25*, 137-154.
64. J. Stöhr, *NEXAFS Spectroscopy*, Springer, Berlin, 1992.
65. M. H. Carpenter, *Helium Atmosphere Chamber for Soft X-ray Spectroscopy of Biomolecules*, MS Thesis, University of California, Davis, 2010.

66. L. Reimer, *Scanning Electron Microscopy Physics of Image Formation and Microanalysis*, Springer, Berlin, 1984.
67. B. Fultz, J.M. Howe, *Transmission Electron Microscopy and Diffractometry of Materials*, Springer, Berlin, 2001
68. W. Paul, M. Raether, *Z. Physik* **1955**, *140*, 262-273.
69. J. B. Farmer, in *Mass Spectroscopy*, ed. C.A. McDowell, McGraw-Hill Book Company, New York, 1963, Chapter 2, pp. 7-45.
70. S. Tanuma, C.J. Powell, and D.R. Penn., *Surf. Interface Anal.*, 1991, **17**, 911-926.
71. N. D. S Canning, D. Outka, R. J. Madix, *Surf. Sci.* **1984**, *141*, 240–254.
72. D. E. King, *J. Vac. Sci. Technol. A* **1995**, *13*, 1247-1253.
73. B. Koslowski, H.-G. Boyen, C. Wilderotter, G. Kästle, P. Ziemann, R. Wahrenberg, P. Oelhafen, *Surf. Sci.* **2001**, *475*, 1-10.
74. P. H Citrin, G. K. Wertheim, Y. Baer, *Phys. Rev. Lett.* **1978**, *41*, 1425-1428.
75. P. Heimann, J. F. van der Veen, D. E. Eastman, *Solid State Commun.* **1981**, *38*, 595-598.
76. H. Tsai, E. Hu, K. Perng, M. Chen, J.-C. Wu, Y.-S.Chang, *Surf. Sci.* **2003**, *537*, L447–L450.
77. C. J. Weststrate, E. Lundgren, J. N. Andersen, E. D. L. Rienks, A. C. Gluhoi, J. W. Bakker, I. M. N. Groot, B. E. Nieuwenhuys, *Surf. Sci.* **2009**, *603*, 2152–2157.
78. K. A. Mills, R. F. Davis, S. D. Kevan, G. Thornton, D.A. Shirley, *Phys. Rev. B* **1980**, *22*, 581.
79. H.-G. Zimmer, A. Goldmann, R. Courths, *Surf. Sci.* **1986**, *176*, 115-124.
80. R. Courths, H.-G. Zimmer, A. Goldmann, H. Saalfeld, *Phys. Rev. B* **1986**, *34*, 3577-3585.
81. A. Cimino, D. Gazzoli, M. Valigi, *J. Electron. Spectrosc. Relat. Phenom.* **1999**, *104*, 1-29.
82. H. Shi, R. Asahi, C. Stampfl, *Phys. Rev. B* **2007**, *75*, 205125.
83. A. Knop-Gericke, M. Hävecker, T. Schedel-Niedrig, R. Schlögl. *Topics Catal.* **2001**, *15*, 27-34.

84. X. Deng, B. K. Min, A. Guloy, C. M. Friend, *J. Am. Chem. Soc.* **2005**, *127*, 9267-9270.
85. A. Krozer, M. Rodalh, *J. Vac. Sci. Technol. A* **1997**, *15*, 1704-1709.
86. J. T. Miller, A. J. Kropf, Y. Zha, J. R. Regalbuto, L. Delannoy, C. Louis, E. Bus, J. A. van Bokhoven, *J. Catal.* **2006**, *240*, 222–234.
87. M. C. Kung, R. J. Davis, H. H. Kung, *J. Phys. Chem. C* **2007**, *111*, 11767-11775.
88. B. K. Min, A. R. Alemozafar, M. M. Biener, J. Biener, C. M. Friend, *Top. Catal.* **2005**, *36*, 77-90.
89. K. Juodkazis, J. Juodkazyte, V. Jasulaitiene, A. Lukinskas, B. Sebeka, *Electrochem. Commun.* **2000**, *2*, 503-507.
90. H. Ron, I. Rubinstein, *Langmuir* **1994**, *10*, 4566-4573.
91. P. Jiang, S. Porsgaard, F. Borondics, M. Köber, A. Caballero, H. Bluhm, F. Besenbacher, M. Salmeron, *J. Am. Chem. Soc.* **2010**, *132*, 2858–2859.
92. W. X. Li, C. Stampfl, M. Scheffler, *Phys. Rev. B* **2003**, *67*, 045408.
93. J. Schnadt, J. Knudsen, X. L. Hu, A. Michaelides, R. T. Vang, K. Reuter, Z. Li, E. Lægsgaard, M. Scheffler, F. Besenbacher, *Phys. Rev. B: Condens. Matter Mater. Phys.*, **2009**, *80*, 075424.
94. T. C. R. Rocha, A. Oestereich, D. V. Demidov, M. Hävecker, S. Zafeiratos, G. Weinberg, V. I. Bukhtiyarov, A. Knop-Gericke, R. Schlögl, *Phys. Chem. Chem. Phys.* **2012**, *14*, 4554-4564.
95. B. K. Min, X. Deng, D. Pinnaduwege, R. Schalek, C.M. Friend, *Phys. Rev. B* **2005**, *72*, 121410.
96. E. I. Intezarova, V. N. Kondrat'ev. *B. Acad. Sci. USSR Ch+* **1967**, *16*, 2326-2331.
97. M. Haruta, *Chemical Records* **2003**, *3*, 75-87.
98. Hutchings, G.J.; Edwards, J.K. In *Frontiers of Nanoscience*, eds. L.J. Roy, J.P. Wilcoxon, Elsevier, Amsterdam, 2012, Vol. 3, Chapter 6, pp. 249–293.
99. R. Meyer, C. Lemire, Sh. K. Shaikhutdinov, H.-J. Freund, *Gold Bull.* **2004**, *37*, 72-124.
100. D. V. Demidov, I. P. Prosvirin, A. M. Sorokin, T. Rocha, A. Knop-Gericke, V. I. Bukhtiyarov, *Catal. Sci. Technol.* **2011**, *1*, 1432-1439.

101. E. Desimoni, G. I. Casella, A. Morone, A. M. Salvi, *Surf. Interface Anal.* **1990**, *15*, 627-634.
102. S. Kundu, Y. Wang, W. Xia, M. Muhler, *J. Phys. Chem. C* **2008**, *112*, 16869–16878.
103. G. Witek, M. Noeske, G. Mestl, S. Shaikhutdinov, R. J. Behm, *Catal. Lett.* **1996**, *37*, 35-39.
104. T. Dickinson, A. F. Povey, P. M. A. Sherwood, *J. Chem. Soc. Faraday Trans.* **1975**, *71*, 298-311.
105. A. Yu. Klyushin, T.C.R Rocha, M. Hävecker, A. Knop-Gericke, R. Schlögl, *Phys. Chem. Chem. Phys.* **2014**, *16*, 7881-7886.
106. D. Tandon, E. J. Hippo, H. Marsh, E. Sebok, *Carbon* **1997**, *35*, 35-44.
107. A. Schaefer, D. Ragazzon, A. Wittstock, L. E. Walle, A. Borg, M. Bäumer, A. Sandell, *J. Phys. Chem C* **2012**, *116*, 4564-4571.
108. N. Saliba, D. H. Parker, B. E. Koel, *Surf. Sci.* **1998**, *410*, 270–282.
109. A.P. Grosvenor, B.A. Kobe, N.S. McIntyre, *Surf. Sci.* **2004**, *572*, 217–227.
110. G. Ertl, R. Hierl, H. Knozinger, N. Thiele, H. P. Urbach, *Appl. Surf. Sci.* **1980**, *5*, 49-64.
111. E. Cano, C. L. Torres, J. M. Bastidas, *Mater. Corros.* **2001**, *52*, 667-676.
112. A. N. Mansour, *Surf. Sci. Spectra* **1994**, *3*, 202-210.
113. G. C. Allen, S. J. Harris, J. A. Jutson, J. M. Dyke, *Appl. Surf. Sci.* **1989**, *37*, 111-134.
114. I. X. Green, W. Tang, M. McEntee, M. Neurock, J.T. Yates, *J. Am. Chem. Soc.* **2012**, *134*, 12717-12723.
115. A. K. Sinha, S. Seelan, S.Tsubota, M. Haruta, *Angew. Chem. Int. Ed.* **2004**, *43*, 1546-1548.
116. H. H. Kung, M. C. Kung, C. K. Costello, *J. Catal.* **2003**, *216*, 425-432.
117. D. W. Goodman, *J. Phys. Chem.* **1996**, *100*, 13090-13102.
118. P. Stefanov, M. Shipochka, P. Stefchev, Z. Raicheva, V. Lazarova, L. Spassov, *J. Phys. Conf. Ser.* **2008**, *100*, 012039.
119. C. Chusuei, X. Lai, K. Luo, D. W. Goodman, *Top. Catal.* **2001**, *14*, 71-83.
120. R. Zanella, L. Delannoy, C. Louis, *Appl. Catal. A Gen.* **2005**, *291*, 62-72.
121. F. Moreau, G. C. Bond, A. O. Taylor, *J. Catal.* **2005**, *231*, 105-114.

122. M. Valden, X. Lai, D. W. Goodman, *Science* **1998**, *281*, 1647-1650.
123. A. K. Tripathi, V. S. Kamble, N. M. Gupta, *J. Catal.* **1999**, *187*, 332-342.
124. T. Bär, T. Visart de Bocarmé, B. E. Nieuwenhuys, N. Kruse, *Catal. Lett.* **2001**, *74*, 127-131.
125. D. Guillemot, V. Yu. Borovkov, V. B. Kazansky, M. Polisset-Thfoin, J. Fraissard, *J. Chem. Soc. Faraday Trans.* **1997**, *93*, 3587-3591.
126. F. Boccuzzi, A. Chiorino, M. Manzoli, P. Lu, T. Akita, S. Ichikawa, M. Haruta, *J. Catal.* **2001**, *202*, 256-267.
127. M. S. Chen, D. W. Goodman, *Science* **2004**, *306*, 252-255.
128. B. Yoon, H. Häkkinen, U. Landman, A. S. Wörz, J.-M. Antonietti, S. Abbet, K. Judai, U. Heiz, *Science* **2005**, *307*, 403-407.
129. S. Minicò, S. Scirè, C. Crisafulli, A. M. Visco, S. Galvagno, *Catal. Lett.* **1997**, *47*, 273-276.
130. C. K. Costello, J.H. Yang, H. Y. Law, Y. Wang, J.-N. Lin, L. D. Marks, M. C. Kung, H. H. Kung, *Appl. Catal. A Gen.* **2003**, *243*, 15-24.
131. M. G. Mason, *Phys. Rev. B* **1983**, *27*, 748-762.
132. Y. Kitsudo, A. Iwamoto, H. Matsumoto, K. Mitsuhara, T. Nishimura, M. Takizawa, T. Akita, Y. Maeda, Y. Kido, *Surf. Sci* **2009**, *603*, 2108-2114.
133. C. Chusuei, X. Lai, K. Luo, D. W. Goodman, *Top. Catal.* **2001**, *14*, 71-83.
134. Z. Yang, R. Wu, *Phys. Rev. B* **2003**, *67*, 081403.
135. Z.-P. Liu, X.-Q. Gong, J. Kohanoff, C. Sanchez, P. Hu, *Phys. Rev. Lett.* **2003**, *91*, 266102.
136. J.-D. Grunwaldt, C. Kiener, C. Wögerbauer, A. Baiker, *J. Catal.* **1999**, *181*, 223-232.
137. M. M. Schubert, S. Hackenberg, A. C. van Veen, M. Muhler, V. Plzak, R. J. Behm, *J. Catal.* **2001**, *197*, 113-122.
138. D. Widmann, R. J. Behm, *Angew. Chem. Int. Ed.* **2011**, *50*, 10241-10245.
139. D. Widmann, R. J. Behm, *Acc. Chem. Res.* **2014**, *47*, 740-749.
140. T. Diemant, Z. Zhao, H. Rauscher, J. Bansmann, R. J. Behm, *Top. Catal.* **2007**, *44*, 83-93.
141. M. Haruta, S. Tsubota, T. Kobayashi, H. Kageyama, M. J. Genet, B. Delmon, *J. Catal.* **1993**, *144*, 175-192.

142. A. I. Kozlov, A. P. Kozlova, H. Liu, Y. Iwasawa, *Appl. Catal. A* **1999**, *182*, 9-28.
143. Y. Yuan, K. Asakura, H. Wan, K. Tsai, Y. Iwasawa, *Catal. Lett.* **1996**, *42*, 15-20.
144. B. E. Solsona, T. Garcia, C. Jones, S. H. Taylor, A. F. Carley, G. J. Hutchings, *Appl. Catal. A* **2006**, *312*, 67–76.
145. R. Liu, N. Gao, F. Zhen, Y. Zhang, L. Mei, X. Zeng, *Chem. Eng. J.* **2013**, *225*, 245-253.
146. M. Haruta, *Catal. Today* **1997**, *36*, 153-166.
147. G.R. Bamwenda, S. Tsubota, T. Nakamura, M. Haruta, *Catal. Lett.* **1997**, *44*, 83-87.
148. M. A. Bollinger, M. A. Vannice, *Appl. Catal. B* **1996**, *8*, 417-443.
149. J. Liu, R. Si, H. Zheng, Q. Geng, W. Dai, X. Chen, X. Fu, *Catal. Commun.* **2012**, *26*, 136–139
150. D. Widmann, Y. Liu, F. Schüth, R. J. Behm, *J. Catal.* **2010**, *276*, 292–305.
151. N. Lopez, T. V. W. Janssens, B. S. Clausen, Y. Xu, M. Mavrikakis, T. Bligaard, J. K. Nørskov, , *J. Catal.* **2004**, *223*, 232–235.